eXPRESS Polymer Letters Vol.10, No.3 (2016) 187
Available online at www.expresspolymlett.com
DOI: 10.3144/expresspolymlett.2016.17

Editorial corner – a personal view
A second life for polymers … needs more research

*M. Gahleitner**

Borealis Polyolefine GmbH, Innovation Headquarters, St. Peterstr. 25, 4021 Linz, Austria

While scientists and engineers tend to focus on the role of polymers as problem solvers, parts of society appear to consider polymers more as a problem. Polymer scientists therefore need to consider the discussed issues in their daily research, like the various end-of-life options for polymer articles. But before going into details let's look what happens to the about 300 mio tons of polymers produced every year right now.

In Europe (EU27+CH+NO), out of 25 mio tons of polymer waste 25% are recycled mechanically and 36.5% used as an energy source (in combustion, steel and cement production mostly). 38.4% or 9.6 mio t still goes to landfills, varying between 1% (CH), 50% (IT) and 70% (UK), while peaking at 87% for Malta (acc. PlasticsEurope). In North America, the recycled fraction is 9% (USA) resp. 16% (Canada), with about 60% going to landfills. China, a hotspot of plastic waste treatment, manages 22%, out of more than 600 mio tons, half of this being imported. Only India manages to re-process more than half at a rate of 60%.

A consequence of this bad resource management together with poorly maintained landfills is the increasing ocean pollution by plastic waste, as the recorded quantities can hardly be caused just by beachside littering (250 kt globally, see DOI: 10.1371/journal.pone.0111913). One may dispute the claimed consequences, but trying to combat this kind of marine pollution by fishing particles from the sea is doomed to failure if the influx is not reduced. That means better waste management and higher cost – and good recycling may partly pay for it.

The role models are there: Global paper production is based 50% on recycling, glass production 75% in Europe and 70% in the US. In all cases, these figures were not just reached by politics or public pressure, but also by ingenuity and research. The fact that polymer recycling is not growing rapidly is at least partly due to a lack of research efforts in the field which is obviously not considered 'sexy' enough by the scientific community. Progress happens, nevertheless, largely driven by industrial research. The highly relevant issue of purification, for example, is largely handled in such developments (e.g. http://www.erema.at/en/general_corema/), and the involvement of small companies demonstrates economic opportunities.

Academic research on recycling, however, is often rather repetitive and unrealistic in scope, even if ~950 papers on the subject were published in 2014 (acc. SciFinder). An example is the use of tyre regrind for toughening thermoplastics – this works well if done correctly, but the simple issue of the necessarily horrid sulphur smell of such compounds which will prevent application of such compounds in more than 90% of the cases is never addressed.

Polymer scientists need to take a fresh look at recycling, dealing with issues like compatibilisation, purification, emission reduction and long-term stability from a 'fundamental perspective'.

Dr. Markus Gahleitner
Member of International Advisory Board

*Corresponding author, e-mail: markus.gahleitner@borealisgroup.com

eXPRESS Polymer Letters Vol.10, No.3 (2016) 188–203
Available online at www.expresspolymlett.com
DOI: 10.3144/expresspolymlett.2016.18

PLA-b-PEG/magnetite hyperthermic agent prepared by Ugi four component condensation

L. P. Icart[1], E. R. F. dos Santos[2], E. D. Pereira[3], S. R. Ferreira[4], V. Saez[1], J. A. Ramon[1], M. Nele[2], J. C. S. Pinto[5], R. D. Toledo[4], D. Z. Silva[1], F. G. Souza Jr[4]*

[1]Departamento de Macromoléculas, Centro de Biomateriales, Universidad de la Habana, av. Ronda 4400, Vedado, La Habana, Cuba
[2]Escola de Química, Centro de Tecnologia-Cidade Universitária, av. Horacio Macedo, bloco E. Universidade Federal de Rio de Janeiro, 2030 Rio de Janeiro, Brasil
[3]Instituto de Macromoléculas: Professora Eloisa Mano, Centro de Tecnologia-Cidade Universitária, av. Horacio Macedo, 2030, bloco J. Universidade Federal de Rio de Janeiro, 2030 Rio de Janeiro, Brasil
[4]Programa de Engenharia Civil, COPPE, Centro de Tecnologia-Cidade Universitária, av. Horacio Macedo, bloco I. Universidade Federal de Rio de Janeiro, 2030 Rio de Janeiro, Brasil
[5]Programa de Engenharia Química, COPPE, Centro de Tecnologia-Cidade Universitária, av. Horacio Macedo, bloco G. Universidade Federal de Rio de Janeiro, 2030 Rio de Janeiro, Brasil

Received 6 July 2015; accepted in revised form 1 October 2015

Abstract. Ugi four component condensation (UFCC), is an important tool for the synthesis of different types of bioconjugate species. In this study, a PLA-PEG/magnetite magnetic composite was prepared by a synthetic-route approach based on UFCC. In particular, poly(lactic acid) (PLA) was synthesized by autocatalytic polycondensation. Also, poly(ethyleneglycol) bis-amine (bis-amine PEG) was synthesized by two different methods: via carbonyldiimidazol (CDI)/ethylenediamine (ED) (75% yield) and via chlorate monochlorated acetyl (CCA)/ED (95% yield). All products were characterized by gel permeation chromatography (GPC), hydrogen-1 nuclear magnetic resonance (NMR ^{1}H), Fourier transform infrared (FTIR), differential scanning calorimetry (DSC) and thermogravimetric analysis (TGA). In addition, magnetite was prepared and modified to generate aldehyde groups which are also necessary for UFCC. This product was characterized by DSC, TGA, X-ray diffraction (XRD) and magnetic force (MF) techniques. Also, the magnetic composite PLA-PEG/magnetite was synthesized by UFCC. The calculated yield was equal to 80%. Furthermore, magnetic microspheres were prepared by the procedure of emulsion solvent-evaporation and characterized by scanning electron microscopy (SEM) and magnetic induction hyperthermia (MIH). The main contribution of these results is to propose a new application for UFCC in the preparation of biomasked magnetic drug delivery systems able to improve the cancer treatment and even the welfare of the patients.

Keywords: *biodegradable polymers, Ugi reaction, magnetic composites, hyperthermic agent*

1. Introduction

Drug delivery systems (DDS) is one of the most exciting research fields of pharmacy, chemistry and other related sciences [1–8]. The clinical benefits have been demonstrated by dozens of products that have already been approved for use in humans and several types of DDS have been approved by regulatory agencies [9].

Many of these systems are based on polymers. Among them, the most widely used are polyethylene glycol (PEG) and the poly(lactic acid) family, including its copolymers with glycolic acid [9, 10]. The

*Corresponding author, e-mail: fgsj@ufrj.br

most important feature of PEG is its potential for biomasking [11–13]. The conjugation of PEG to DDS or drugs (e.g. peptides and proteins) prevents recognition by the various defense systems of organisms [14–16].

In turn, PLA or poly(lactic/glycolic acid) (PLGA) copolymers have been widely studied with regard to the controlled release of drugs occluded in this matrix by diffusion or erosion of biodegradable polymers [17–21]. Since 1987, there have been 1042 reports of DDS, based on PEG-PLA or the PLGA polymeric system. However, in the last five years, 600 papers were published, which suggests a remarkable level of interest in this scientific field. The properties and applications of DDS can be improved by the use of magnetic particles. These composites have the potential to be targeted to a specific site by using magnetic fields. In addition, they could be very useful in magnetic hyperthermia therapy [22–25].

Magnetic particles modified with biodegradable PLGA or PLA were firstly prepared in the beginning of the 1990s by chemical adsorption or molecular interactions between a reactive polymer end group and the surface of the particle [26–30]. On the other hand, the surface modification of magnetic particles by chemical linkage of polymers is less documented, even less by the use of Ugi four component condensation (UFCC).

The main objective of this study was to prepare a new system of controlled drug release, based on the union of the three elements mentioned above (i.e. PLA, PEG and magnetic particles) and using Ugi four component condensation (UFCC) [31]. This reaction is useful to the functionalization and PEGylation of biomacromolecules based on glycoprotein [32], lipoprotein [33] and polymeric conjugates [34–36]. UFCC is a condensation reaction in which an aldehyde or a ketone, an amine, an isocyanide, and a carboxylic acid can form a bis-amide. It is considered a prime example of a multi-component reaction (MCRs) which proceeds by the formation of an imine as a result of condensation of the aldehyde and primary amine. Afterwards, the isocyanide and carboxylic acid are added to the imine intermediate which, via an acyl transfer, rearranges to the bis-amide product [37].

This new DDS could be used in very interesting applications, such as (i) the occlusion of hydrophobic drugs in the PLA phase, which can be released by diffusion and erosion of the polymer matrix; (ii) the conjugation of targeting elements to the amino end groups of the PEG chain; (iii) the production of biomasking by PEG chains, increasing the lifetime of the system; (iv) additional targeting capability due to the presence of the magnetic iron oxide core; and (v) use of the phenomenon of magnetic hyperthermia. Therefore, the presented material is very interesting due to the advantages of Ugi reaction, which make the synthetic route less expensive and enables easier manipulation of the reagents used. In addition, it can increase the efficiency of treatments, improving the welfare of patients.

2. Experimental

2.1. Materials

Lactic acid (85%), $FeCl_3 \cdot 6H_2O$, $FeSO_4 \cdot 7H_2O$, KOH, glutaraldehyde (50%), reduced Fe, $CoSO_4 \cdot 7H_2O$ and $CuSO_4 \cdot 5H_2O$, polyvinyl alcohol (PVA) and ethylenediamine were purchased from VETEC. PEG (M_n 6000), carbinyldiimidazole (CDI), chlorate monochlorated acetyl (CCA) and tert-butyl isocyanide were purchased from SIGMA-ALDRICH.

2.2. Synthesis of PLA polymeric system by autocatalytic polycondensation

The PLA polymer was synthesized from 85% lactic acid (700 mL), in a closed system with slight vacuum (–550 mL/mm Hg). The reaction medium was kept at 180 °C for 12 h. The product of the reaction was purified by solubilization in chloroform (250 mL) and precipitation in cold ethanol (4 L).

2.3. Synthesis of end amine functionalized PEG

2.3.1. Via CDI/ED

PEG (0.5 g) dissolved in dichloromethane (70 mL) was reacted with an appropriate amount of CDI (10 equivalent) overnight, at room temperature under stirring. Soon afterwards, the reaction mixture was concentrated by rotoevaporation and the activated PEG was purified by three precipitations in cold diethyl ether (140 mL) and filtered under a slight vacuum. The purified activated PEG (0.1 g) dissolved in dichloromethane (14 mL) was reacted with appropriate amounts of ethylenediamine (10 equivalent) overnight, at room temperature under stirring. Then, the reaction mixture was concentrated by rotoevaporation and diafiltered against distilled water, (cellulose acetate membrane, 1 kDa cutoff). Finally, the bis-amine PEG was dried by lyophilization.

2.3.2. Via CCA/ED

PEG (5 g) dissolved in 100 mL hexane/dichloromethane (1.1 vv) was reacted with an appropriate amount off CCA (6 equivalent) for 8 hours, at room temperature and under stirring. Then, the reaction mixture was kept under nitrogen atmosphere for 30 minutes. Immediately following this, 14 mL of ethanol was added and the system was kept under reflux for 30 minutes. Finally, the reaction mixture was concentrated by rotoevaporation until 50 mL. Suddenly the activated PEG was reacted with appropriate amounts of ethylenediamine (10 equivalents) for 48 hours at room temperature and stirring. The final product was purified by precipitation in diethyl ether (250 mL) followed by slight vacuum filtration.

2.4. Synthesis of magnetite and aldehyde-modified magnetite

Magnetite was prepared as described in the literature [38]. Briefly, in separate vessels, 3.375 g (2.5 mmol) of $FeCl_3 \cdot 6H_2O$ and 3.475 g (2.5 mmol) of $FeSO_4 \cdot 7H_2O$ were dissolved in 100 mL of deionized water. Subsequently, these two solutions were mixed and then 50 mL of aqueous solutions of KOH 2 M were added rapidly under stirring; the final product was a black precipitate that is attracted by a neodymium magnet. The magnetite was washed three times with deionized water and once with ethanol using magnetic decantation. The final product was dried at room temperature. The purified magnetite mixed in distilled water (75 mL) was reacted, first with glutaraldehyde 50% (10 mL) for 9 min under sonication (450 Watts) and then was kept overnight under mechanical agitation at room temperature. The modified magnetite was washed once with ethanol using magnetic decantation and dried at room temperature.

2.5. Synthesis of Ugi-magnetic-composite (UMC)

Aldehyde-modified magnetite (0.08 g) dispersed in 2 mL chloroform/methanol (1:2 v/v mixture) was reacted with appropriate amount of bis-amine PEG (0.15 μMol) overnight at room temperature under nitrogen atmosphere and stirring (Modify-aldehyde magnetite/ bis-amine PEG molar ratio = 1:5). The protonated imine formed was reacted with PLA (0.029 μMol) and tert-butyl isocyanide (0.029 μMol) at room temperature for 72 hours under nitrogen atmosphere and stirring (aldehyde-modified magnetite/bis-amine PEG/PLA/tert-butyl isocyanide molar ratio equal to 1/5/5/1, respectively). After this time, the product obtained was washed once with ethanol using magnetic decantation and dried at room temperature.

2.6. Preparation of magnetic microsphere

Magnetic microspheres were prepared using the single emulsion-solvent evaporation methodology [39], with some modifications. Briefly, the UMC (100 mg) was dispersed in 1 mL of dichloromethane. Soon afterwards, the prepared UMC dispersion was added to a beaker containing 5 mL of cold PVA (w/w 0.5%). This system was kept under stirring at 20 000 rpm during 5 minutes. Then, the o/w emulsion was poured into a beaker containing 50 mL of PVA (w/w 0.1%) and kept under mechanical stirring for 2 hours at room temperature (25 °C) to harden the microspheres by solvent evaporation. Magnetic microspheres were then collected by centrifugation at 2500 rpm and washed 3 times with distilled water. Finally, the collected magnetic microspheres were freeze-dried by lyophilization and stored at 12 °C.

2.7. Materials characterizations

2.7.1. Hydrogen-1 nuclear magnetic resonance

Mmeasurements of PLA and bis-amine PEG were carried out in a Varian Mercury VX-300 NMR spectrometer operating at 300 MHz (^{1}H) and 75 MHz (^{13}C). Samples (15 or 50 mg) were dissolved in chloroform-D1 (0.8 mL) in 5 mm NMR tubes at room temperature.

2.7.2. Gel permeation chromatography

Measurements of PLA and bis-amine PEG were determined using an Agilent 1200 series HPLC with a MIXED-C column. Chloroform was used as the solvent with a flow rate of 1.0 mL/min and polystyrene was used as a standard.

2.7.3. Fourier transform infrared

Spectra of PLA, bis-amine PEG and aldehyde-modified magnetite was performed using a Varian model 3100 FTIR Excalibur Series spectrophotometer (Japan). Samples were macerated with potassium bromide (1 mg/100 mg samples/KBr). Then, the FTIR spectra of the samples were recorded at room temperature and a resolution of 4 cm^{-1}.

2.7.4. Differential scanning calorimetry

Measurement of PLA, bis-amine PEG, magnetite, aldehyde-modified magnetite and UMC was carried out with help of the TA Q1000 V9.9 build 303 Calorimeter. Briefly, 5 mg of the samples were heated and cooled at a rate of 10 °C/min from –80 to 200 °C under nitrogen flow. Values of glass transition (T_g), melting temperature (T_m) and the crystallization temperature on cooling (T_{cc}) were taken in a cooling run after the second heating run.

2.7.5. Thermogravimetric analyses

Were performed using a TA TGA Q500 Thermoanalyser. Measurements were carried out in nitrogen at a heating rate of 20 °C/min up to 700 °C with a gas flow rate of 20 mL/min.

2.7.6. X-ray diffraction

Measurement of bis-amine PEG, magnetite, aldehyde-modified magnetite and UMC was determined in Rigaku Miniflex X-ray diffractometer in a 2θ range from 20 to 70° by the FT (fixed time) method. The steps used were equal to 0.05° and a time of 1s, using a tube voltage and current equal to 40 kV and 20 mA, respectively. The radiation used was CuKα = 1.5418 Å.

2.7.7. Magnetic force

Measurement of magnetite, aldehyde-modified magnetite and UMC were performed as reported by our group elsewhere [40]. Briefly the samples were kept under a variable magnetic field (0–790 Gauss), calibration of the test was performed by using reduced Fe, $CoSO_4 \cdot 7H_2O$ and $CuSO_4 \cdot 5H_2O$ as standard for high level, medium level and a lack of magnetic force, respectively [41–43]. Then, the apparent variation in the mass of the sample in the presence of a magnetic field was calculated subtracting the mass of the sample in the presence of a magnetic field from the mass of sample.

2.7.8. Scanning electron microscopy

Measurement of magnetite, UMC and magnetic microspheres was carried out with a JEOL JSM-5610 LV microscope, using acceleration voltage of 15 kV. Samples were coated with gold in order to study the morphology of the magnetic particles synthesized by UFCC. The materials were sampled by taking several images of various magnifications to ensure that analysis was based on a representative region of the sample.

2.7.9. Magnetic induction hyperthermia

MIH measurements of magnetic microspheres were performed using the Ambrell Easy Heat machine model L1. Samples, dispersed in distilled water (10 and 20 mg/mL at 25 °C), were thermally isolated using glass fiber textile. Soon afterwards, each sample was inserted inside the coil of the machine. Electrical current equal to 200, 400 and 600 A were applied for 600 s. Sample temperature was recorded at 120, 240, 360, 480 and 600 s. The bulk temperature of the samples was measured before and after the induction heating tests.

3. Results and discussion

The Ugi reaction allows the binding, in a single experimental step, of four functional groups: amine, aldehyde, carboxylic acid and isocyanide [37]. In this work, we placed these functional groups as follows:

I. PEG provided the amine group. Instead of using a commercial diamine reagent, PEG was modified so that the amine group is attached to the polymer backbone by labile bond (i.e., amide). This labile link could permit the release of PEG and/or any molecule bound to the free end.
II. Iron particles were coated with aldehyde groups. This choice was based on the ease of modification of the NP with glutaraldehyde.
III. Obviously, the carboxylic group was supplied by the PLA.
IV. A commercial reagent was used as tert-butyl isocyanide. However, this could be replaced by some interesting molecules in future applications.

3.1. Synthesis of diamine PEG

Firstly, PEG was modified by a known method [44, 45], which is based on the reaction of the hydroxyl groups of the polymer with ethylenediamine in the presence of CDI [46]. However, yields were small (Table 1). Possibly due to the various purification steps necessary to remove excess CDI. To improve yields, another linker was used to attach the ED: chlorate monochlorated acetyl. In this reaction, further purification steps were not necessary after the synthesis of Product 1 (see Figure 1), due to the easy elimination of the hydrochloric acid during the

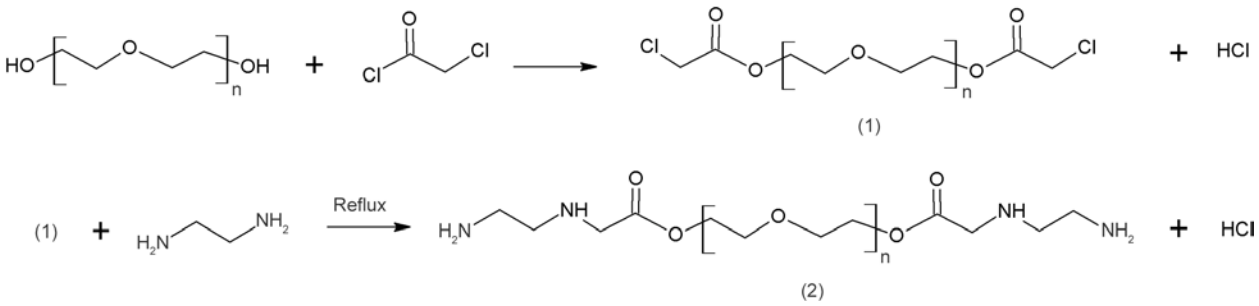

Figure 1. Synthesis of PEG bis-amine by chlorate monochlorated acetyl/carbinyldiimidazole reaction

Table 1. Yields of poly (ethyleneglycol) bis amine functionalized ($p < 0.01$)

Samples	Method	Yield [%]	SD*	CV**
PEG bis amine 1	Via CDI/ED	71.7	1.5	2.1
PEG bis amine 2	Via CCA/ED	94.3	1.2	1.2

*Standard Deviation
**Variation coefficient

acetylation. On the other hand, the residual CCA remaining after refluxing was eliminated by ethanol esterification. The formed ester was easily eliminated because it was miscible with the solvent used for the synthesis and purification of bis-amine PEG [47]. Moreover, the cross-link reactions, on both sides of PEG, were avoided using a small excess of ethylenediamine.

The yields of this reaction were significantly increased, as shown in Table 1, as expected due to there being fewer purification steps required.

As shown in Table 1, the mechanism of CDI/ED presented moderate yields, probably due to several purifications steps being required to eliminate the residual CDI before the amine reaction. However, these results are in agreement with those reported for the functionalization of PEG with CDI [48]. On the other hand, high yields (94.3%) were achieved for 8 h reaction at room temperature with CCA/ED; it was not necessary to perform purification of activated PEG with CCA before the amine reaction.

The products (1) and (2) of the Figure 1 were characterized by NMR ^{1}H and FTIR and the spectra obtained are shown in Figures 2 and 3, respectively. It can be seen in Figure 2a that only two peaks at 4.11 and 3.65 ppm appear, which are assigned as (CH_2Cl) and ethylene (CH_2–CH_2) groups of CCA and PEG, respectively [49]. Consequently, the ^{1}H-NMR spectra of aminated PEG (Figure 2b) retained the peak at 3.65 ppm assigned to (CH_2–CH_2) of PEG and to (CH_2 α C=O); however, Figure 2b allows us to infer the absence of the peak assigned to CH_2Cl groups of CCA. These protons might appear overlapped by the signal of (CH_2–CH_2) groups of PEG due to the release of chloride group after the amination process, which suggests the success of the amination process. Unfortunately, we cannot observe the peaks assigned to the ethylene (CH_2–CH_2) groups of ethylenediamine, probably due to their overlap with the ethylene (CH_2–CH_2) groups of PEG.

FTIR spectra of activated and aminated PEG showed the characteristic absorption bands of this product, i.e. the stretching band at 1751 and 1730 cm^{-1} related to C=O of ester groups of activated and aminated PEG, respectively (see Figure 3). Axial bending at 3420 cm^{-1} is related to the N–H of amine groups of aminated PEG (see Figure 3 curve b). Unfortunately, the absorption band characteristic of amine groups like C–N bounds could not be observed, probably due to the small molar range of amine groups in relation to PEG.

3.2. Synthesis of PLA

Low molecular weight PLA was synthesized by one-step autocatalytic polycondensation of the lactic acid. This procedure does not need further purification steps to eliminate the catalytic agent; in this case, the purification process was performed to ensure the elimination of low molecular weight oligomers [50]. The synthesized PLA was characterized by FTIR; the results are shown in Figure 4.

The FTIR spectra of PLA homopolymers, shown in Figure 4, present the characteristic absorption bands of this polymer [51], i.e., an axial bending at 3518 cm^{-1} corresponding to O–H groups, axial bending at 2997 and 2946 cm^{-1} related to CH and CH_3, a stretching band at 1757 cm^{-1} corresponding to C=O groups, asymmetric and symmetric deformation vibrations at 1486 and 1464 cm^{-1} of the CH_3 groups, a stretching band at 1271 cm^{-1} of C-C=O groups, stretching bands at 1196, 1134, 1093 cm^{-1} related to C–O groups, a stretching band at 1046 cm^{-1} of O–H

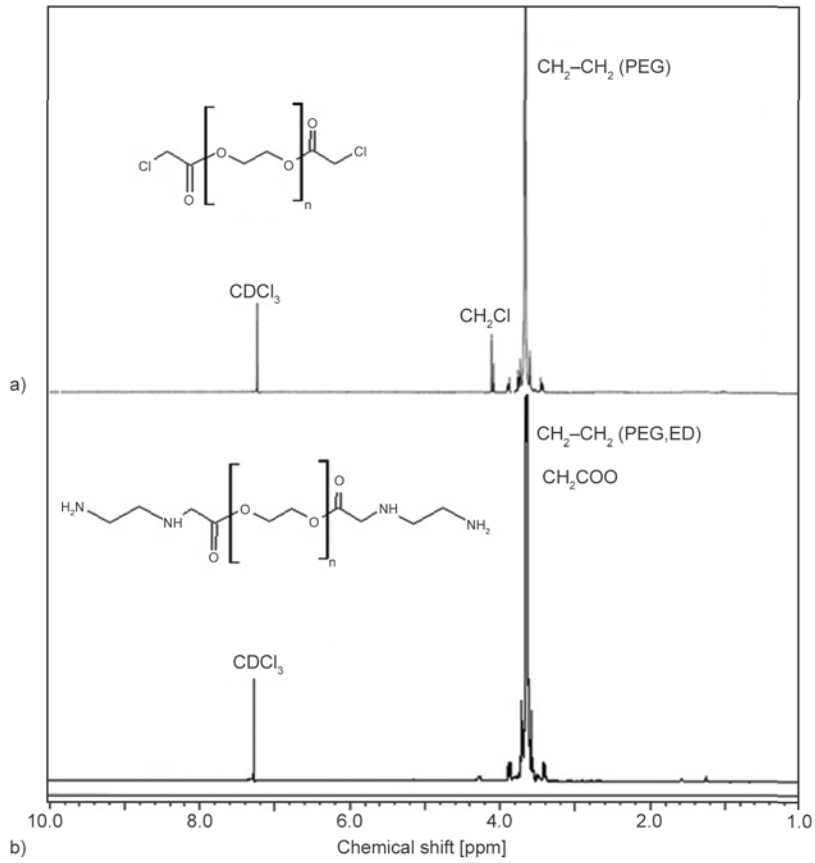

Figure 2. [1]H-NMR spectra of activated PEG (a) and aminated PEG (b)

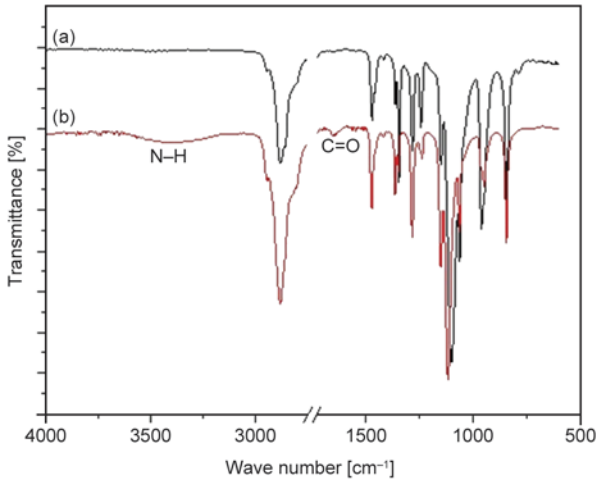

Figure 3. FTIR spectra of activated PEG (a) and FTIR of aminated PEG (b)

groups, stretching bands at 875 and 789 cm^{-1} related to C–C groups and a stretching band at 704 cm^{-1} of the O–H group; these are all in agreement with those reported in the literature [10, 52].

In turn, the synthesized PLA were characterized by [1]H-NMR and [13]C-NMR, shown in Figures 5 and 6, respectively.

Figure 4 shows the [1]H-NMR spectra of the PLA homopolymers. It can be clearly seen from Figure 5

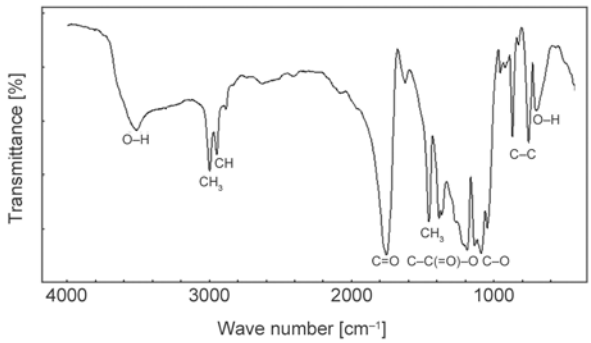

Figure 4. FTIR spectra of synthesized PLA

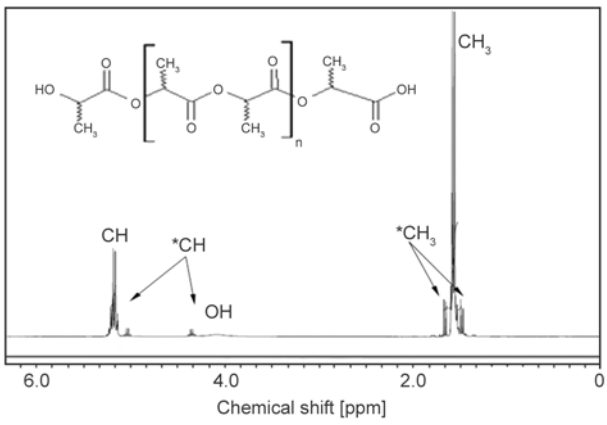

Figure 5. [1]H-NMR spectra obtained for sample of the PLA homopolymer

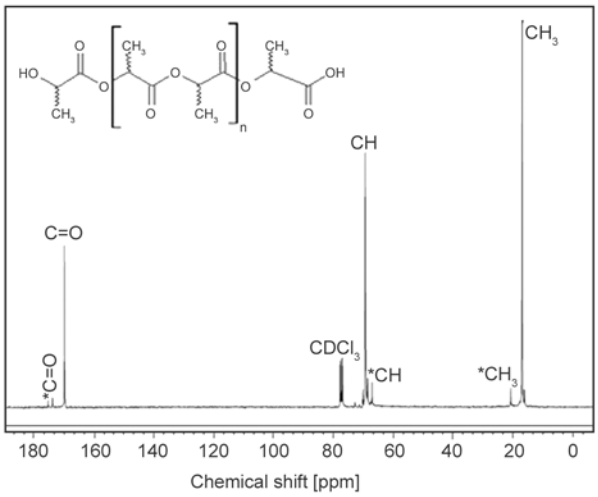

Figure 6. ^{13}C-NMR spectra obtained for samples of the PLA homopolymers

Table 2. Molecular weights of synthesized poly(lactic acid)

Samples	M_w [g·mol^{-1}]	M_n [g·mol^{-1}]	M_w/M_n
PLA1	6543	4641	1.41
PLA2	6475	4466	1.45
PLA3	6287	4428	1.42

that only two peaks at 1.49 and 5.16 ppm appear, which are assigned to the methyl (CH_3) and methine (CH) signals from the PLA homopolymer, respectively [53]. These results are consistent with those obtained from PLA homopolymers prepared by the polycondensation of lactic acid [54]. Furthermore, Figure 6 shows three peaks at 16.92, 69.35 and 169.83 ppm which are assigned to the methyl (CH_3), methine (CH) and carbonyl (C=O) groups, respectively. The peaks that appear at 1.47, 1.65, 4.34, and 5.14 ppm (see Figure 5) and 20.71, 67.77, and 17383 ppm (see Figure 6) were assigned to the D-lactic acid product present in the samples [55, 56].

The number-average molecular weights (M_n) and polydispersities (M_w/M_n) obtained from GPC are listed in Table 2.

Three batches of PLA were prepared by the method described in this work. Analysis by GPC (Table 2) showed good batch-to-batch reproducibility (Variant coefficient ≈2%). The polymers obtained presented molecular weight values suitable for use in controlled release systems [57]. Furthermore, a narrow M_w/M_n allows greater control of the release profiles [58].

3.3. Synthesis of aldehyde-modified magnetite

Glutaraldehyde modification of the magnetite obtained by co-precipitation [38] was studied by

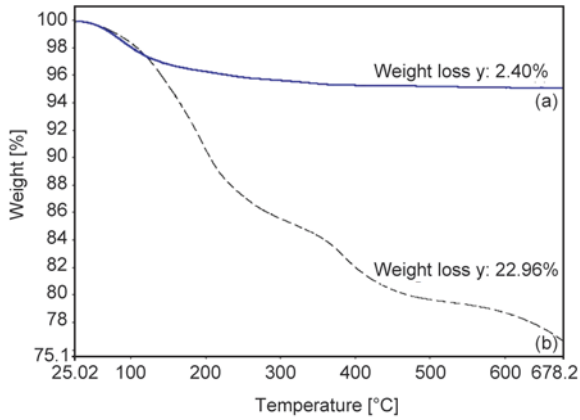

Figure 7. Thermogravimetric analysis of magnetite (a) and aldehyde-modified magnetite (b)

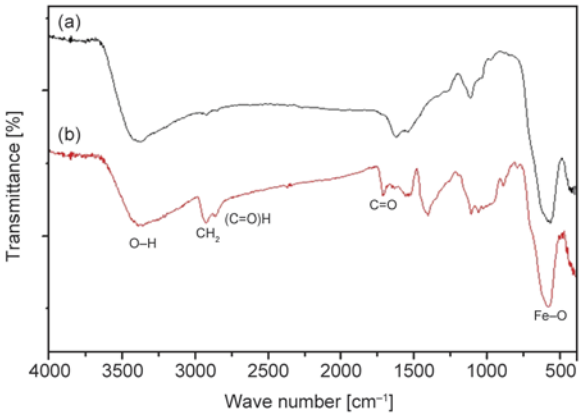

Figure 8. FTIR spectra of magnetite 7 (a) and aldehyde-modified magnetite 7 (b)

thermogravimetric analysis; the results obtained are shown in Figure 7.

The comparison between weight losses up to 600 °C of magnetite and modified product, equal to 2.0% (due to water loss) and 22.9%, respectively, demonstrated the presence of the aldehyde.

Aldehyde modification of magnetite was also confirmed by FTIR analyses, as can be seen in Figure 8. The FTIR spectrum of magnetite provides information about the excitation of vibration or rotation of molecules in their ground electronic state. In the magnetite structure presented in Figure 8 curve a, these vibrations are associated with the stretching deformation of the interatomic bond of iron with other molecules like oxygen and appears at 588 and 585 cm^{-1} [59, 60]. The FTIR analysis of aldehyde-modified magnetite (Figure 8 curve b) also showed the presence of aldehyde groups by the appearance of stretching bands at 1717 cm^{-1} related to C=O of ester groups, axial bending at 2860 cm^{-1} related to (C=O)H of the aldehyde group and axial bending at 2927 cm^{-1} corresponding to the CH_2 of aldehyde groups.

3.4. Synthesis of Ugi magnetic composite

Ugi as well as Passerini reactions are classified as isocyanide-based multicomponent reactions. The Ugi reaction is usually performed in a polar protic solvent such as methanol, and some success in water was recently showed [61]. In turn, non-polar halogenated solvents favoring the occurrence of the Passerini reaction, since most of the amines are insoluble in cited media [62]. Thus, the synthesis of the magnetic composite was performed in dichloromethane/MeOH. This medium as chosen due to the heterogeneous nature of the Ugi components. In addition, the bis-amine PEG is soluble in dichloromethane, allowing its use in the Ugi reaction. This way, the Ugi reaction is favored in comparison with Passerini reaction as shown in Figure 9. The yield of the magnetic composite synthesis was equal to 80%, determined by the weight of the final product. Obtained material was characterized by TGA and the main results are shown in Table 3.

Table 3 shows the decrease of the T_g, T_c and T_m of UMC in comparison to PLA. The replacement of the rigid homogeneous PLA-PLA interaction by heterogeneous PLA-PEG interaction in the UMC makes the macromolecular motion easier, producing the observed decrease of the temperature in the cited transitions (see Figure 10a). As a consequence, the UMC exhibited values of T_g (52.8 °C) that were lower than those for PLA, equal to 52.8 and 59.8 °C, respectively (see Table 3). These results are in agreement with those previously reported for the decreased values of T_g in some PLA-PEG copolymers [63]. The influence of PEG on the crystallization behavior of UMC is also shown in Table 3. From this table, it was observed that the T_c of PLA decreased significantly with the incorporation of PEG (reduction around 15 °C). Similar results were reported for the T_c behavior of PLA-PEG copolymers [64]. The melting behavior is also influenced by the incorporation of PEG into PLA. It was clearly evident from Table 3 that there was a decrease in the T_m of between 14 and 21 °C in the case of UMC. This decrease in the melting point is also an indication of the formation of a composite (Figure 8 curve b) [65]. The degree of crystallinity increased from 21.2 to 29.2% in the case of UMC, suggesting that X_c increased in the case of UMC with an increase of the ΔH_m. In turn, the increased crystallinity in the PLA-PEG copolymer was previously reported [66]. It could be con-

Table 3. TGA analyses of carboxylic PLA, aminated PEG and Ugi magnetic composite

Sample	T_g [°C]	T_{cc} [°C]	T_m [°C]	X_c [%]	T_d^* [°C]
PLA	59.8	98.6	144.0 154.4	21.2	272.8
PEG-NH_2	–	–	56.7	–	394.1
UMC	52.8	84.2	140.3 123.2 54.4	29.2	264.4 392.4

Determined considering $\Delta H_m^0 = 106$ J/g [85].
*Degradation temperature determined by TGA

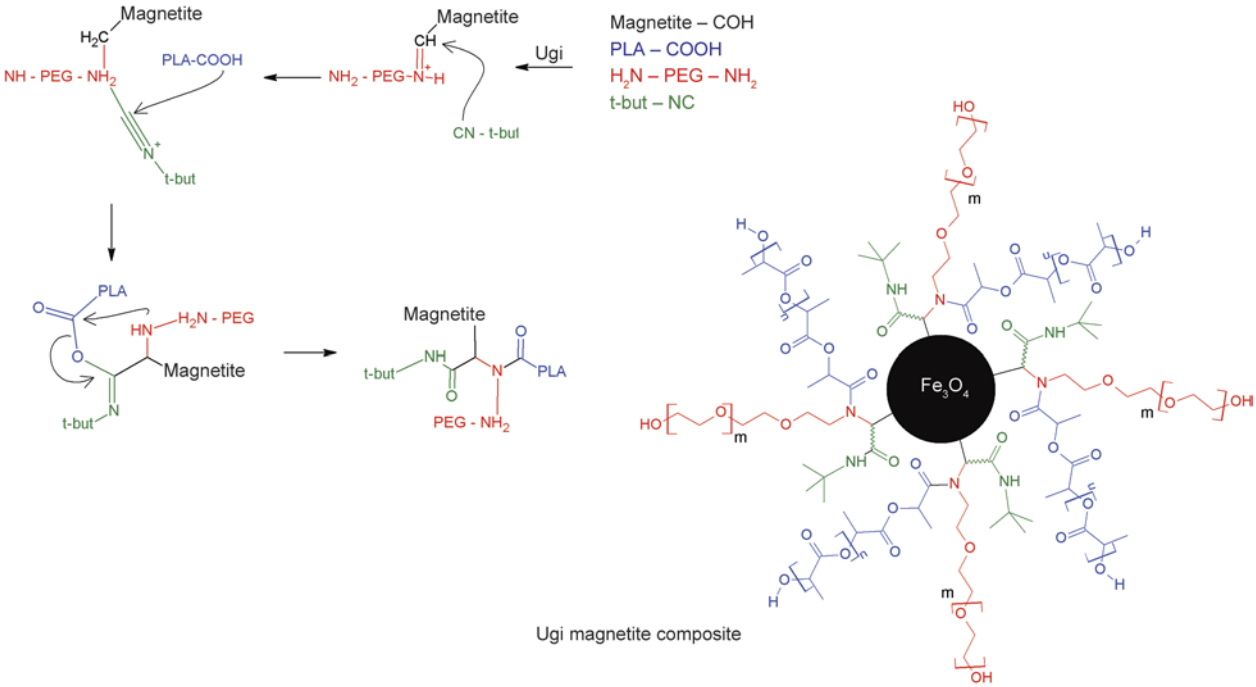

Figure 9. Syntheses of magnetic composite by Ugi four component condensation sheme of Ugi magnetic particle

cluded that PEG has the ability to increase flexibility of the UMC material by increasing the mobility of the PLA molecule [16]. On the other hand, only two temperatures for weight loss appeared, at 264.4 and 392.4 °C (see Table 3 and Figure 10c), for the Ugi magnetic composite, which probably belong to the PLA and PEG molecule, respectively. The increase of the polymer chains mobility in the UMC material can decrease the thermal stability of the material. In addition, this phenomenon could be enhanced by the presence of basic amines from the residual bis-amine PEG. Moreover, the residue in the case of UMC was negligible. Therefore, these results are in agreement with those that have been previously reported [67].

In addition, the chemical linkage between PEG, PLA and magnetite could be confirmed by the FTIR spectra of Ugi magnetite composite (Figure 11).

In Figure 11, the absorption bands of PEG and PLA linked to magnetite are clearly seen; i.e., axial bending at 2945 cm^{-1} related to CH_2 of the ether groups and axial bending at 1093 cm^{-1} corresponding to C–O of ether groups, which are assigned to PEG. The stretching band at 1762 cm^{-1} related to C=O of ester groups, axial bending at 2996 cm^{-1} corresponding to CH_3 and the stretching band at 1048 cm^{-1} were related to (C=O)–O–C of the ester groups, which were assigned to PLA. Finally, the FTIR spectra also presented the stretching absorption bands of magnetite at 588 and 585 cm^{-1} described above.

Magnetic composites were also characterized by XRD, the results of which are shown in Figure 12.

XRD results from magnetite, magnetite modified with aldehyde and magnetic composite are shown in Figures 12 curves a)–c) respectively. All the tested materials present peaks at 2θ equal to 30.3°, 35.7°, 43.3°, 53.9°, 57.3° and 63.0°, which confirm the spinel structure of the crystal, characteristic of this iron oxide [68], proving that Ugi four component condensation does not change the particles' nature [40, 27, 69]. Moreover, the crystal size of magnetic particles was calculated by the Scherrer equation [70]. Crystal size values of 13.6, 13.4 and 12.5 nm were obtained for magnetite, aldehyde-modified magnetite and Ugi magnetic composite particles, respectively. This nanometric size could provide superparamagnetic properties for the Ugi-modified magnetic particles [71] making them very interesting for studies of nano-carriage, targeting and magnetic hyperthermia [22, 72, 73].

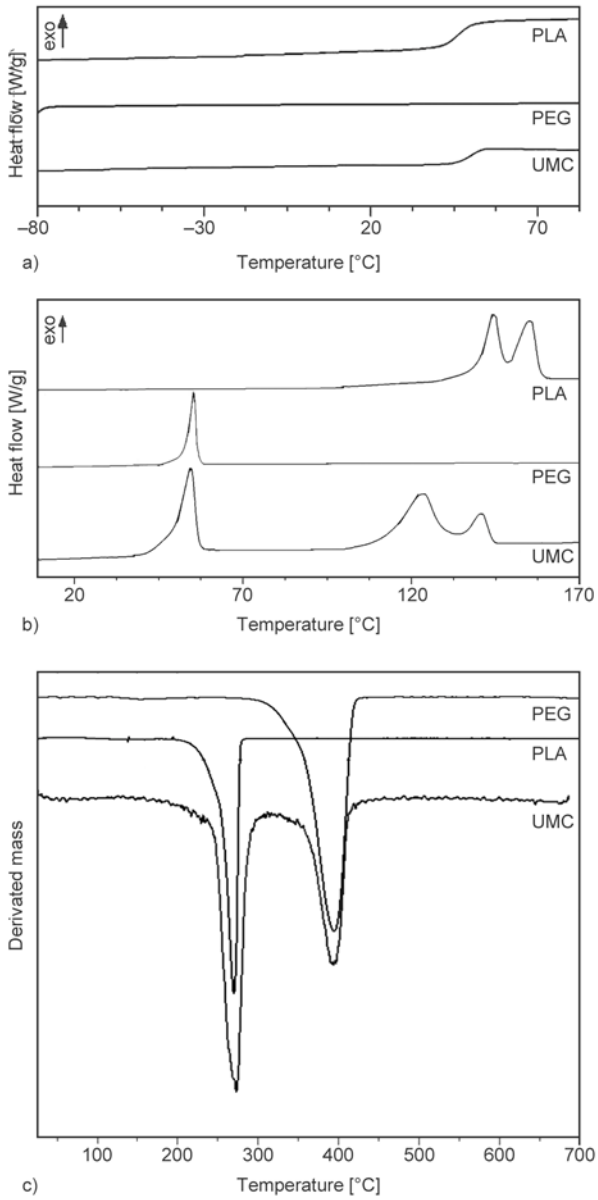

Figure 10. DSC thermograms of PLA, PEG and it magnetic Ugi composite, T_g (8a) and T_m (8b). TGA curves for PLA, PEG and UMC (8c).

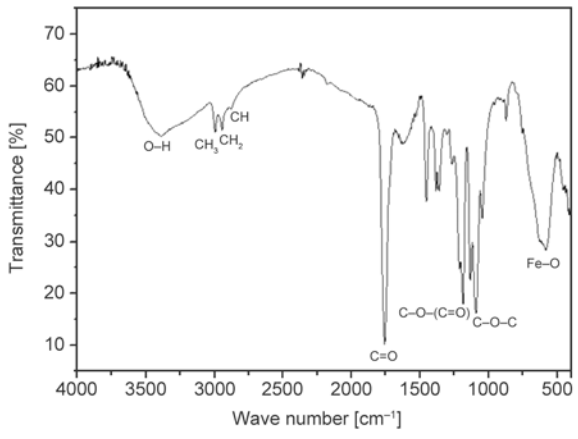

Figure 11. FTIR spectra of Ugi magnetic composite

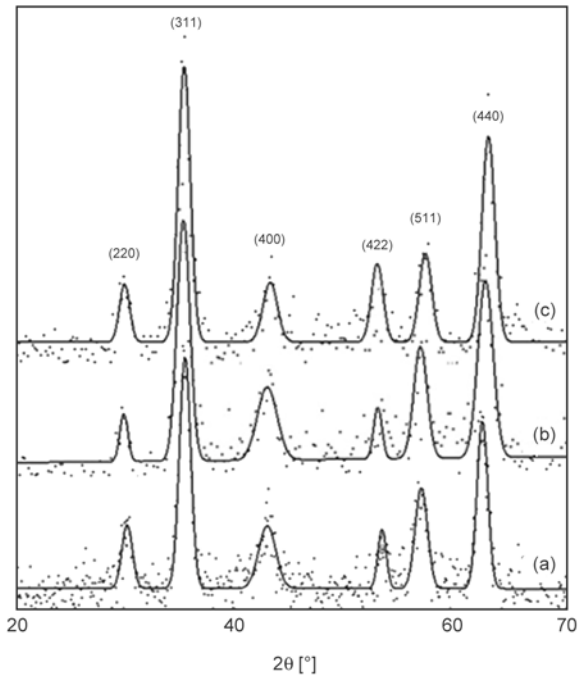

Figure 12. XRD analyses of magnetite 10a, aldehyde magnetite 10b and Ugi magnetic composite 10c

The magnetic products obtained were also characterized by magnetic force tests, the results of which are shown in Table 4 and Figure 13.

As expected, the chemical modification of magnetite and its covalent linkage to PEG and PLA by Ugi four component condensation decreased the values of magnetic force of the composite [40, 74, 75] when compared to free magnetite and aldehyde magnetite. These results are in agreement with those reported for the organic modification of magnetite [76–78].

Taking into account that the crystalline structure of magnetite remains unchanged after Ugi modification, this decrease in the magnetic force of composite is due to the presence of the organic phase on magnetite; this result is in complete agreement with that of TGA.

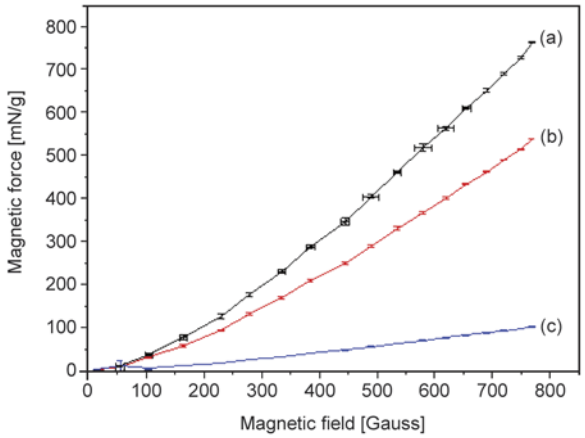

Figure 13. Magnetic force of magnetite (a), aldehyde magnetite (b) and Ugi magnetic composite at 800 Gauss (c)

Table 4. Magnetic force of magnetite, aldehyde magnetite and Ugi magnetic composite

Samples	MF [mN/g]	Relative MF [%]
Magnetite	762.89±1.20	–
Aldehyde magnetite	589.10±0.74	<29.33
Ugi magnetic composite	103.14±1.20	<86.48

MF: magnetic force

Morphology of non-modified magnetite, modified magnetite bonded to PLA and PEG by UFCC and magnetic microspheres was characterized by the scanning electron microscopy technique; the results are shown in Figure 14.

Figure 14 shows the morphological change of magnetite after Ugi four component reaction with PEG and PLA. The particles of pure magnetite (see Figures 14a and 14b) present a smooth surface. On the other hand, the UFCC-modified magnetic particles (see Figure 14c and 14d) presented a different morphology, with an increase of the surface roughness due to the new organic phase bound to the magnetite particles, confirming the success of the chemical modification of magnetite with PEG and PLA by UFCC. In addition, Figure 14e clearly shows that UMC is able to form magnetic microspheres of PLA/PEG/magnetite after the single emulsion-solvent evaporation procedure. The surface structure of all microspheres possesses large pores, which probably influence the amount of PEG linked by UFCC. The ability of PEG to form small pores in the surfaces of the microspheres was reported for microparticles based on blends of PLGA/PLA and PEG and also applies to microparticles composed of diblock polymer [79]. During the precipitation step, the PEG branches of the diblock copolymer orientated toward the internal and surrounding aqueous phase and formed a sponge-like structure [80].

Finally, the heating experiments in AC magnetic field were performed on a medium frequency induction heating apparatus. Figure 15 show the temperature of the samples as function of the electrical current and time. Magnetic PLA-PEG/magnetite microspheres were tested using two concentrations, equal to 10 and 20 mg/mL. All the tests were started at 25 °C. As one can see, the reached temperature is directly related to the used concentration, electrical

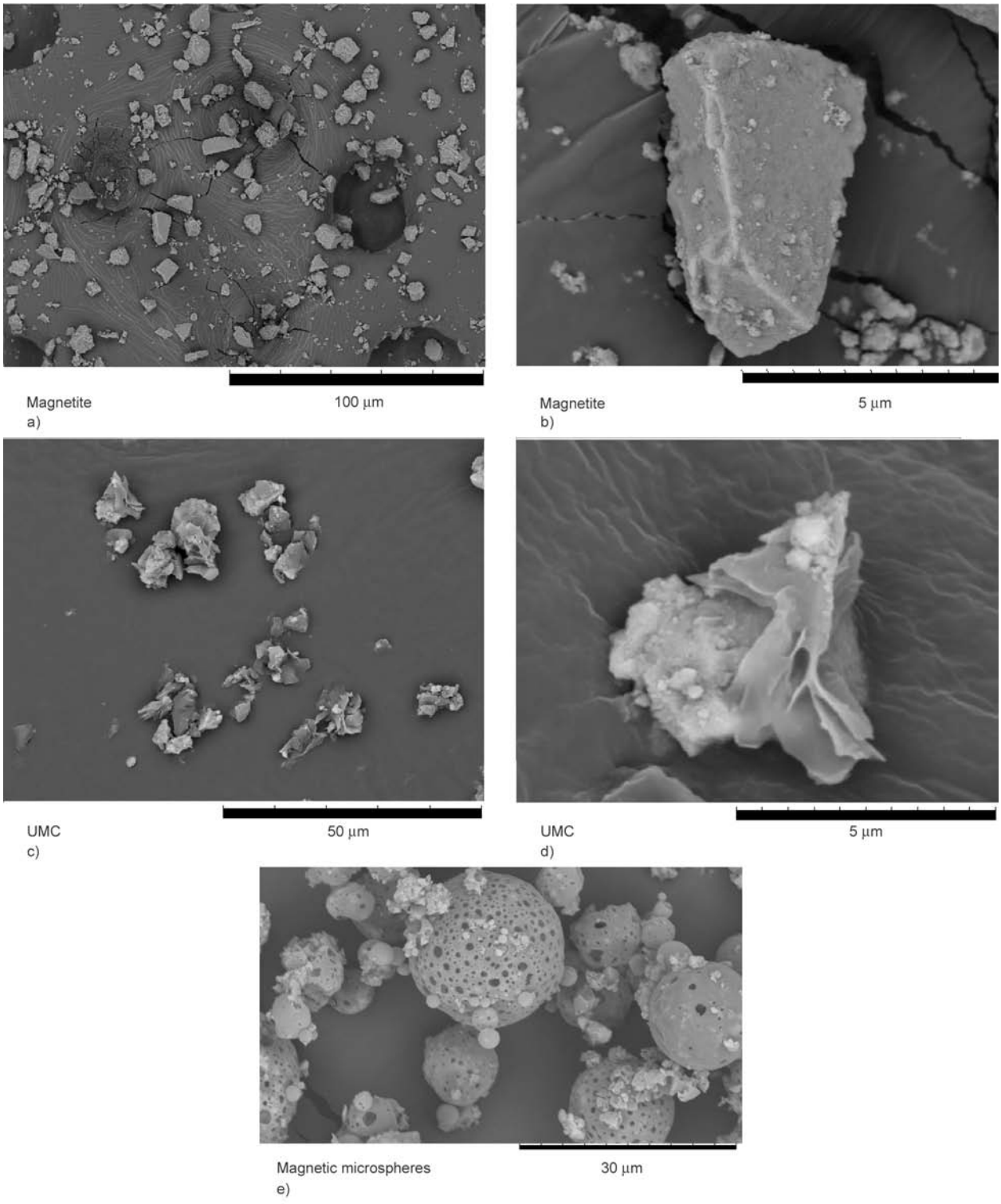

Figure 14. Scanning electron microscopy of magnetite (a and b) and Ugi-magnetic-composite (c and d), magnetic microspheres of PLA/PEG/magnetite (e)

current and time. The use of the highest current values produced the highest temperatures. Thus, the heating effect could be controlled by adjusting the value of the apparent current [28, 81, 82]. In addition, in the best cases, achieved using 600 A, the temperature of samples with concentrations equal to 10 and 20 mg/mL increased from 25 to 37.7 and 47.1 °C, respectively. Similar results were obtained from hypertermic evaluation of particles based on biodegradable polymers [81, 82].

In spite iron magnetic particle generally be well tolerated by the organism, they can be used in the generation of reactive oxygen species, which cause direct damage to DNA, proteins or lipid molecules

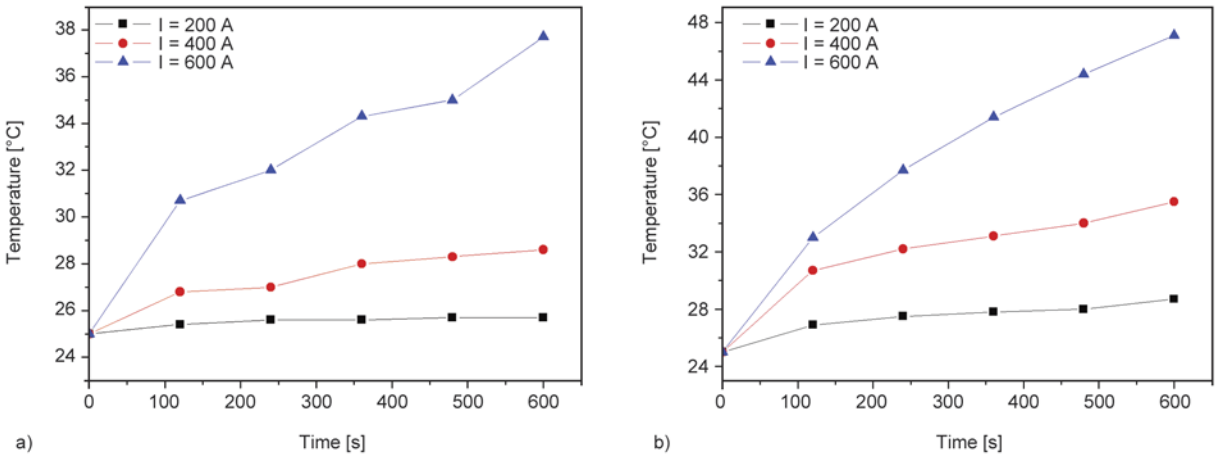

Figure 15. Heating curves of the magnetic microspheres of PLA/PEG/magnetite tested at two different concentration equal to 10 mg/mL (a) and 20 mg/mL (b)

[26]. Thus, magnetic particles are usually surface-modified or coated with biocompatible and biodegradable polymer molecules such as PLA and PEG. In these work the UMC was well characterized by thermogravimetric and spectroscopic techniques, confirming the chemical linkage of PEG and PLA to the magnetite. This result is very encouraging since presented UMC could be biocompatible due to the use of the PLA and PEG, which are widely used in DDS [83, 84].

On the other hand this material could be useful to treat cancers, either alone or in combination with radiotherapy or chemotherapy. Therefore, the presented set of results allow us to infer that presented material, as well as constituting a new application of UFCC, could be very useful for the preparation of biomasked magnetic drug delivery systems.

4. Conclusions

Ugi four component condensation made the PEGylation of PLA and magnetite in a one pot step reaction possible. The results obtained indicate that one application of Ugi reaction is suitable for the PEGylation of magnetic particles. Superficial modification is the most important aspect of particles in biomedical applications to consider in order to improve their biocompatibility with biological entities. As a consequence, superficial modification of magnetite by Ugi reaction was corroborated by FTIR, DSC, TGA, optical and electronic microscopy, which made it possible to identify the copolymer (PLA-PEG) distributed around the magnetic particles. Besides, the synthesized material presented a good magnetic force, which was able to keep the magnetic composite in a specific location in the presence of any external magnetic field. In addition, the synthesized magnetic composite was able to form magnetic microspheres that could potentially be useful for the site-specific delivery of any cytotoxic agent for cancer therapy. Also, these magnetic microspheres are useful to magnetic hyperthermia applications, improving the cancer treatment and even the welfare of the patients.

Acknowledgements

The authors thank Conselho Nacional de Desenvolvimento Científico e Tecnológico (CNPq-474940/2012-8 and 550030/2013-1), Coordenação de Aperfeiçoamento de Pessoal de Nível Superior (CAPES and CAPES-MES Cuba # 154/12), Financiadora de Estudos e Projetos (FINEP PRESAL Ref. 1889/10), Rafael Moraes of LaBios laboratory by the induction magnetic test, LABEST laboratory and Fundação Carlos Chagas Filho de Amparo à Pesquisa do Estado do Rio de Janeiro (FAPERJ) for the financial support and scholarships.

References

[1] Zhou Y., Li H., Yang Y-W.: Controlled drug delivery systems based on calixarenes. Chinese Chemical Letters, **26**, 825–828 (2015). DOI: 10.1016/j.cclet.2015.01.038

[2] Keith D., Cui H.: Fabrication of drug delivery systems using self-assembled peptide nanostructures. in 'Micro and nanofabrication using self-assembled biological nanostructures' (eds.: Castillo-León J., Svendsen W.) William Andrew, Oxford, 91–115 (2015). DOI: 10.1016/B978-0-323-29642-7.00005-9

[3] Yoshida T.: Stimuli-sensitive polymers for drug delivery and diagnostic systems interacting with biosurfaces. in 'Switchable and responsive surfaces and materials for biomedical applications' (ed.: Zhang J.) Woodhead, Oxford, 235–258 (2015).

[4] Yasin M. N., Svirskis D., Seyfoddin A., Rupenthal I. D.: Implants for drug delivery to the posterior segment of the eye: A focus on stimuli-responsive and tunable release systems. Journal of Controlled Release, **196**, 208–221 (2014).
DOI: 10.1016/j.jconrel.2014.09.030

[5] Elgadir M. A., Uddin M. S., Ferdosh S., Adam A., Chowdhury A. J. K., Sarker M. Z. I.: Impact of chitosan composites and chitosan nanoparticle composites on various drug delivery systems: A review. Journal of Food and Drug Analysis, in press (2015).
DOI: 10.1016/j.jfda.2014.10.008

[6] Khanday M. A., Rafiq A.: Variational finite element method to study the absorption rate of drug at various compartments through transdermal drug delivery system. Alexandria Journal of Medicine, **51**, 219–223 (2015).
DOI: 10.1016/j.ajme.2014.09.001

[7] Moulton S. E., Wallace G. G.: 3-dimensional (3D) fabricated polymer based drug delivery systems. Journal of Controlled Release, **193**, 27–34 (2014).
DOI: 10.1016/j.jconrel.2014.07.005

[8] Rodrigues L. R.: Microbial surfactants: Fundamentals and applicability in the formulation of nano-sized drug delivery vectors. Journal of Colloid and Interface Science, **449**, 304–316 (2015).
DOI: 10.1016/j.jcis.2015.01.022

[9] Reddy K. R.: Controlled-release, pegylation, liposomal formulations: New mechanisms in the delivery of injectable drugs. The Annals of Pharmacotherapy, **34**, 915–923 (2000).
DOI: 10.1345/aph.10054

[10] Chen C-C., Chueh J-Y., Tseng H., Huang H-M., Lee S-Y.: Preparation and characterization of biodegradable PLA polymeric blends. Biomaterials, **24**, 1167–1173 (2003).
DOI: 10.1016/S0142-9612(02)00466-0

[11] Perry J. L., Reuter K. G., Kai M. P., Herlihy K. P., Jones S. W., Luft J. C., Napier M., Bear J. E., DeSimone J. M.: PEGylated PRINT nanoparticles: The impact of PEG density on protein binding, macrophage association, biodistribution, and pharmacokinetics. Nano Letters, **12**, 5304–5310 (2012).
DOI: 10.1021/nl302638g

[12] Huang M., Wu W., Qian J., Wan D-J., Wei X-L., Zhu J-H.: Body distribution and *in situ* evading of phagocytic uptake by macrophages of long-circulating poly (ethylene glycol) cyanoacrylate-*co*-*n*-hexadecyl cyanoacrylate nanoparticles. Acta Pharmacologica Sinica, **26**, 1512–1518 (2005).
DOI: 10.1111/j.1745-7254.2005.00216.x

[13] Fontana G., Licciardi M., Mansueto S., Schillaci D., Giammona G.: Amoxicillin-loaded polyethylcyanoacrylate nanoparticles: Influence of PEG coating on the particle size, drug release rate and phagocytic uptake. Biomaterials, **22**, 2857-2865 (2001).
DOI: 10.1016/S0142-9612(01)00030-8

[14] Ohguchi Y., Kawano K., Hattori Y., Maitani Y.: Selective delivery of folate–PEG-linked, nanoemulsion-loaded aclacinomycin A to KB nasopharyngeal cells and xenograft: Effect of chain length and amount of folate–PEG linker. Journal of Drug Targeting, **16**, 660–667 (2008).
DOI: 10.1080/10611860802201464

[15] Wang B., Zhang Y., Guo Z., Cheng J., Fang Z.: Biodegradable aliphatic/aromatic copoly(ester-ether)s: The effect of poly(ethylene glycol) on physical properties and degradation behavior. Journal of Polymer Research, **18**, 187–196 (2011).
DOI: 10.1007/s10965-010-9406-4

[16] Zhong T., Deng C., Gao Y., Chen M., Zuo B.: Studies of *in situ*-forming hydrogels by blending PLA-PEG-PLA copolymer with silk fibroin solution. Journal of Biomedical Materials Research Part A, **100**, 1983–1989 (2012).
DOI: 10.1002/jbm.a.33307

[17] Tawfeek H. M., Evans A. R., Iftikhar A., Mohammed A. R., Shabir A., Somavarapu S., Hutcheon G. A., Saleem I. Y.: Dry powder inhalation of macromolecules using novel PEG-*co*-polyester microparticle carriers. International Journal of Pharmaceutics, **441**, 611–619 (2013).
DOI: 10.1016/j.ijpharm.2012.10.036

[18] Krawczak P.: Medical plastics: Serving healthcare. Express Polymer Letters, **7**, 651 (2013).
DOI: 10.3144/expresspolymlett.2013.61

[19] Nkabinde L. A., Shoba-Zikhali L. N. N., Semete-Makokotlela B., Kalombo L., Swai H., Grobler A., Hamman J. H.: Poly (D,L-lactide-*co*-glycolide) nanoparticles: Uptake by epithelial cells and cytotoxicity. Express Polymer Letters, **8**, 197–206 (2013).
DOI: 10.3144/expresspolymlett.2014.23

[20] Ke Y., Liu G. S., Wang J. H., Xue W., Du C., Wu G.: Preparation of carboxymethyl cellulose based microgels for cell encapsulation. Express Polymer Letters, **8**, 841–849 (2014).
DOI: 10.3144/expresspolymlett.2014.85

[21] Hamad K., Kaseem M., Yang H. W., Deri F., Ko Y. G.: Properties and medical applications of polylactic acid: A review. Express Polymer Letters, **9**, 435–455 (2015).
DOI: 10.3144/expresspolymlett.2015.42

[22] Mahmoudi M., Sant S., Wang B., Laurent S., Sen T.: Superparamagnetic iron oxide nanoparticles (SPIONs): Development, surface modification and applications in chemotherapy. Advanced Drug Delivery Reviews, **63**, 24–46 (2011).
DOI: 10.1016/j.addr.2010.05.006

[23] Laurent S., Dutz S., Häfeli U. O., Mahmoudi M.: Magnetic fluid hyperthermia: Focus on superparamagnetic iron oxide nanoparticles. Advances in Colloid and Interface Science, **166**, 8–23 (2011).
DOI: 10.1016/j.cis.2011.04.003

[24] Pollert E., Veverka P., Veverka M., Kaman O., Závěta K., Vasseur S., Epherred R., Gogliod G., Duguetd E.: Search of new core materials for magnetic fluid hyperthermia: Preliminary chemical and physical issues. Progress in Solid State Chemistry, **37**, 1–14 (2009). DOI: 10.1016/j.progsolidstchem.2009.02.001

[25] Erathodiyil N., Ying J. Y.: Functionalization of inorganic nanoparticles for bioimaging applications. Accounts of Chemical Research, **44**, 925–935 (2011). DOI: 10.1021/ar2000327

[26] Frounchi M., Shamshiri S.: Magnetic nanoparticles-loaded PLA/PEG microspheres as drug carriers. Journal of Biomedical Materials Research Part A, **103**, 1893–1898 (2015). DOI: 10.1002/jbm.a.35317

[27] Pereira E. D., Souza F. G., Pinto J. C. C. S., Cerruti R., Santana C.: Synthesis, characterization and drug delivery profile of magnetic PLGA-PEG-PLGA/maghemite nanocomposite. Macromolecular Symposia, **343**, 18–25 (2014). DOI: 10.1002/masy.201300168

[28] Sun Y., Zheng Y., Ran H., Zhou Y., Shen H., Chen Y., Chen H., Krupka T. M., Li A., Li P., Wang Z., Wang Z.: Superparamagnetic PLGA-iron oxide microcapsules for dual-modality US/MR imaging and high intensity focused US breast cancer ablation. Biomaterials, **33**, 5854–5864 (2012). DOI: 10.1016/j.biomaterials.2012.04.062

[29] Yu D., Zhang Y., Zhou X., Mao Z., Gao C.: Influence of surface coating of PLGA particles on the internalization and functions of human endothelial cells. Biomacromolecules, **13**, 3272–3282 (2012). DOI: 10.1021/bm3010484

[30] Ren J., Hong H., Ren T., Teng X.: Preparation and characterization of magnetic PLA–PEG composite nanoparticles for drug targeting. Reactive and Functional Polymers, **66**, 944–951 (2006). DOI: 10.1016/j.reactfunctpolym.2006.01.002

[31] Ziegler T., Gerling S., Lang M.: Preparation of bioconjugates through an Ugi reaction. Angewandte Chemie International Edition, **39**, 2109–2112 (2000). DOI: 10.1002/1521-3773(20000616)39:12<2109::AID-ANIE2109>3.0.CO;2-9

[32] de Nooy A. E. J., Masci G., Crescenzi V.: Versatile synthesis of polysaccharide hydrogels using the passerini and ugi multicomponent condensations. Macromolecules, **32**, 1318–1320 (1999). DOI: 10.1021/ma9815455

[33] Crescenzi V., Francescangeli A., Capitani D., Mannina L., Renier D., Bellini D.: Hyaluronan networking via Ugi's condensation using lysine as cross-linker diamine. Carbohydrate Polymers, **53**, 311–316 (2003). DOI: 10.1016/S0144-8617(03)00079-1

[34] Yang B., Zhao Y., Ren X., Zhang X., Fu C., Zhang Y., Wei Y., Tao L.: The power of one-pot: A hexa-component system containing π–π stacking, Ugi reaction and RAFT polymerization for simple polymer conjugation on carbon nanotubes. Polymer Chemistry, **6**, 509–513 (2014). DOI: 10.1039/C4PY01323A

[35] Yang B., Zhao Y., Wang S., Zhang Y., Fu C., Wei Y., Tao L.: Synthesis of multifunctional polymers through the Ugi reaction for protein conjugation. Macromolecules, **47**, 5607–5612 (2014). DOI: 10.1021/ma501385m

[36] Sehlinger A., Verbraeken B., Meier M. A. R., Hoogenboom R.: Versatile side chain modification *via* isocyanide-based multicomponent reactions: Tuning the LCST of poly(2-oxazoline)s. Polymer Chemistry, **6**, 3828–3836 (2015). DOI: 10.1039/C5PY00392J

[37] Dömling A., Ugi I.: Multicomponent reactions with isocyanides. Angewandte Chemie International Edition, **39**, 3168–3210 (2000). DOI: 10.1002/1521-3773(20000915)39:18<3168::AID-ANIE3168>3.0.CO;2-U

[38] RuizMoreno R. G., Martinez A. I., Castro-Rodriguez R., Bartolo P.: Synthesis and characterization of citrate coated magnetite nanoparticles. Journal of Superconductivity and Novel Magnetism, **26**, 709–712 (2013). DOI: 10.1007/s10948-012-1790-z

[39] Lucke A., Fustella E., Teßmar J., Gazzaniga A., Göpferich A.: The effect of poly(ethylene glycol)–poly(D,L-lactic acid) diblock copolymers on peptide acylation. Journal of Controlled Release, **80**, 157–168 (2002). DOI: 10.1016/S0168-3659(02)00020-2

[40] Souza F. G., Ferreira A. C., Varela A., Oliveira G. E., Machado F., Pereira E. D., Fernandes E., Pinto J. C., Nele M.: Methodology for determination of magnetic force of polymeric nanocomposites. Polymer Testing, **32**, 1466–1471 (2013). DOI: 10.1016/j.polymertesting.2013.09.018

[41] Ribeiro G. A. P.: Magnetic properties of the matter: A first contact (in Portuguese). Revista Brasileira de Ensino de Física, **22**, 299–305 (2000).

[42] Lu A-H., Salabas E. L., Schüth F.: Magnetic nanoparticles: Synthesis, protection, functionalization, and application. Angewandte Chemie International Edition, **48**, 1222–1244 (2007). DOI: 10.1002/anie.200602866

[43] Martins T. S., Isolani P. C.: Rare earths: Industrial and biological applications (in Portugese). Química Nova, **28**, 111–117 (2005). DOI: 10.1590/S0100-40422005000100020

[44] Rajagopalan S., Gonias S. L., Pizzo S. V.: A nonantigenic covalent streptokinase-polyethylene glycol complex with plasminogen activator function. The Journal of Clinical Investigation, **75**, 413–419 (1985). DOI: 10.1172/JCI111715

[45] Beauchamp C. O., Gonias S. L., Menapace D. P., Pizzo S. V.: A new procedure for the synthesis of polyethylene glycol-protein adducts; Effects on function, receptor recognition, and clearance of superoxide dismutase, lactoferrin, and α_2-macroglobulin. Analytical Biochemistry, **131**, 25–33 (1983).
DOI: 10.1016/0003-2697(83)90131-8

[46] Lukyanov A. N., Sawant R. M., Hartner W. C., Torchilin V. P.: PEGylated dextran as long-circulating pharmaceutical carrier. Journal of Biomaterials Science, Polymer Edition, **15**, 621–630 (2004).
DOI: 10.1163/156856204323046889

[47] Zhang J., Fan X., Liu Y., Bo L., Liu X.: Synthesis of poly(ethylene glycol)–metaxalone conjugates and study of its controlled release *in vitro*. International Journal of Pharmaceutics, **332**, 125–131 (2007).
DOI: 10.1016/j.ijpharm.2006.09.039

[48] Bischo R.: Polyethylene-hirudinea conjugates, preparation and use in thrombosis treatment (in Spanish). Spanish Patent 2 169 037, Spain (1993).

[49] Wang X-L., Mou Y-R., Chen S-C., Shi J., Wang Y-Z.: A water-soluble PPDO/PEG alternating multiblock copolymer: Synthesis, characterization, and its gel–sol transition behavior. European Polymer Journal, **45**, 1190–1197 (2009).
DOI: 10.1016/j.eurpolymj.2008.12.038

[50] Narayan R., Bandyopadhyay A., Bose S.: Biomaterials science: Processing, properties, and applications. Wiley, Westerville (2011).

[51] Liu Q., Yang X., Xu H., Pan K., Yang Y.: Novel nanomicelles originating from hydroxyethyl starch-*g*-polylactide and their release behavior of docetaxel modulated by the PLA chain length. European Polymer Journal, **49**, 3522–3529 (2013).
DOI: 10.1016/j.eurpolymj.2013.08.012

[52] Sin L. T., Rahmat A. R., Rahman W. A. W. A. Polylactic acid: PLA biopolymer technology and applications. William Andrew, Chicago (2012).

[53] Mercado-Pagán Á. E., Kang Y., Ker D. F. E., Park S., Yao J., Bishop J., Yang Y.: Synthesis and characterization of novel elastomeric poly(D,L-lactide urethane) maleate composites for bone tissue engineering. European Polymer Journal, **49**, 3337–3349 (2013).
DOI: 10.1016/j.eurpolymj.2013.07.004

[54] Selukar B. S., Parwe S. P., Mohite K. K., Garnaik B.: Synthesis and characterization of linear polylactic acid-based urethanes using tin modified solid cloisite-30B catalyst. Advanced Materials Letters, **3**, 161–171 (2012).
DOI: 10.5185/amlett.2011.11325

[55] Achmad F., Yamane K., Quan S., Kokugan T.: Synthesis of polylactic acid by direct polycondensation under vacuum without catalysts, solvents and initiators. Chemical Engineering Journal, **151**, 342–350 (2009).
DOI: 10.1016/j.cej.2009.04.014

[56] Xiao L., Wang B., Yang G., Gauthier M.: Poly(lactic acid)-based biomaterials: Synthesis, modification and applications. in 'Biomedical science, engineering and technology' (ed.: Ghista D. N.), Rijeka, 247–282 (2012).
DOI: 10.5772/23927

[57] Zhou S., Deng X., Li X., Jia W., Liu L.: Synthesis and characterization of biodegradable low molecular weight aliphatic polyesters and their use in protein-delivery systems. Journal of Applied Polymer Science, **91**, 1848–1856 (2004).
DOI: 10.1002/app.13385

[58] Chia H-H., Yang Y-Y., Chung T-S., Ng S., Heller J.: Auto-catalyzed poly(ortho ester) microspheres: A study of their erosion and drug release mechanism. Journal of Controlled Release, **75**, 11–25 (2001).
DOI: 10.1016/S0168-3659(01)00362-5

[59] Cavalcante L. C. D., Lage M. C. S. M., Fabris J. D.: Chemical analysis of red pigment in human bone (in Portugese). Química Nova, **31**, 1117–1120 (2008).
DOI: 10.1590/S0100-40422008000500034

[60] Andrade A. L., Souza D. M., Pereira M. C., Fabris J. D., Domingues R. Z.: Synthesis and characterization of magnetic nanoparticles coated with silica through a sol-gel approach. Cerâmica, **55**, 420–424 (2009).
DOI: 10.1590/S0366-69132009000400013

[61] Lehnhoff S., Goebel M., Karl R. M., Klösel R., Ugi I.: Stereoselective syntheses of peptide derivatives with 2-acetamido-3,4,6-tri-*O*-acetyl-1-amino-2-deoxy-β-D-glucopyranose by four-component condensation. Angewandte Chemie International Edition in English, **34**, 1104–1107 (1995).
DOI: 10.1002/anie.199511041

[62] Dömling A.: Recent developments in isocyanide based multicomponent reactions in applied chemistry. Chemical Reviews, **106**, 17–89 (2006).
DOI: 10.1021/cr0505728

[63] Paul M-A., Alexandre M., Degée P., Henrist C., Rulmont A., Dubois P.: New nanocomposite materials based on plasticized poly(L-lactide) and organo-modified montmorillonites: Thermal and morphological study. Polymer, **44**, 443–450 (2003).
DOI: 10.1016/S0032-3861(02)00778-4

[64] Ozkoc G., Kemaloglu S.: Morphology, biodegradability, mechanical, and thermal properties of nanocomposite films based on PLA and plasticized PLA. Journal of Applied Polymer Science, **114**, 2481–-2487 (2009).
DOI: 10.1002/app.30772

[65] Yang J., Zhao T., Liu L., Zhou Y., Li G., Zhou E., Chen X.: Isothermal crystallization behavior of the poly(L-lactide) block in poly(L-lactide)-poly(ethylene glycol) diblock copolymers: Influence of the PEG block as a diluted solvent. Polymer Journal, **38**, 1251–1257 (2006).
DOI: 10.1295/polymj.PJ2006094

[66] Thomas S., Durand D., Chassenieux C., Jyotishkumar P.: Handbook of biopolymer-based materials: From blends and composites to gels and complex networks. Wiley, Weinheim (2013).

[67] Song Y-P., Wang D-Y., Wang X-L., Lin L., Wang Y-Z.: A method for simultaneously improving the flame retardancy and toughness of PLA. Polymers for Advanced Technologies, **22**, 2295–2301 (2011).
DOI: 10.1002/pat.1760

[68] Feuser P. E., dos Santos Bubniak L., dos Santos Silva M. C., da Cas Viegas A., Fernandes A. C., Ricci-Junior E., Nele M., Tedesco A. C., Sayer C., de Araújo P. H. H.: Encapsulation of magnetic nanoparticles in poly(methyl methacrylate) by miniemulsion and evaluation of hyperthermia in U87MG cells. European Polymer Journal, **68**, 355–365 (2015).
DOI: 10.1016/j.eurpolymj.2015.04.029

[69] Pereira E. D., Souza F. G., Santana C. I., Soares D. Q., Lemos A. S., Menezes L. R.: Influence of magnetic field on the dissolution profile of cotrimoxazole inserted into poly(lactic acid-*co*-glycolic acid) and maghemite nanocomposites. Polymer Engineering and Science, **53**, 2308–2317 (2013).
DOI: 10.1002/pen.23606

[70] Xu X. X., Zheng Y. F.: Synthesis and characterization of magnetic nanoparticles and their reinforcement in polyurethane film. Key Engineering Materials, **324–325**, 659–662 (2006).
DOI: 10.4028/www.scientific.net/KEM.324-325.659

[71] Neves J. S., de Souza F. G., Suarez P. A. Z., Umpierre A. P., Machado F.: *In situ* production of polystyrene magnetic nanocomposites through a batch suspension polymerization process. Macromolecular Materials and Engineering, **296**, 1107–1118 (2011).
DOI: 10.1002/mame.201100050

[72] de Souza K. C., Mohallem N. D. S., de Sousa E. M. B.: Magnetic nanocomposites: Potential for applications in biomedicine (in Portugese). Química Nova, **34**, 1692–1703 (2011).
DOI: 10.1590/S0100-40422011001000003

[73] Jeong U., Teng X., Wang Y., Xia Y.: Superparamagnetic colloids: Controlled synthesis and niche applications. Advanced Materials, **19**, 33–60 (2006).
DOI: 10.1002/adma.200600674

[74] de Souza F., Marins J. A., Pinto J., de Oliveira G., Rodrigues C., Lima L.: Magnetic field sensor based on a maghemite/polyaniline hybrid material. Journal of Materials Science, **45**, 5012–5021 (2010).
DOI: 10.1007/s10853-010-4321-y

[75] Grance E. G. O., Souza F. G., Varela A., Pereira E. D., Oliveira G. E., Rodrigues C. H. M.: New petroleum absorbers based on lignin-CNSL-formol magnetic nanocomposites. Journal of Applied Polymer Science, **126**, E304–E311 (2012).
DOI: 10.1002/app.36998

[76] Schimanke G., Martin M.: *In situ* XRD study of the phase transition of nanocrystalline maghemite (γ-Fe_2O_3) to hematite (α-Fe_2O_3). Solid State Ionics, **136–137**, 1235–1240 (2000).
DOI: 10.1016/S0167-2738(00)00593-2

[77] Hui C., Shen C., Tian J., Bao L., Ding H., Li C., Tian Y., Shi X., Gao H-J.: Core-shell Fe_3O_4@SiO_2 nanoparticles synthesized with well-dispersed hydrophilic Fe_3O_4 seeds. Nanoscale, **3**, 701–705 (2011).
DOI: 10.1039/C0NR00497A

[78] Sarkar A., Biswas S. K., Pramanik P.: Design of a new nanostructure comprising mesoporous ZrO_2 shell and magnetite core (Fe_3O_4@mZrO_2) and study of its phosphate ion separation efficiency. Journal of Materials Chemistry, **10**, 4417–4424 (2010).
DOI: 10.1039/B925379C

[79] Lochmann A., Nitzsche H., von Einem S., Schwarz E., Mäder K.: The influence of covalently linked and free polyethylene glycol on the structural and release properties of rhBMP-2 loaded microspheres. Journal of Controlled Release, **147**, 92–100 (2010).
DOI: 10.1016/j.jconrel.2010.06.021

[80] Essa S., Rabanel J. M., Hildgen P.: Effect of polyethylene glycol (PEG) chain organization on the physicochemical properties of poly(D, L-lactide) (PLA) based nanoparticles. European Journal of Pharmaceutics and Biopharmaceutics, **75**, 96–106 (2010).
DOI: 10.1016/j.ejpb.2010.03.002

[81] Shah S. A., Majeed A., Rashid K., Awan S-U.: PEG-coated folic acid-modified superparamagnetic $MnFe_2O_4$ nanoparticles for hyperthermia therapy and drug delivery. Materials Chemistry and Physics, **138**, 703–708 (2013).
DOI: 10.1016/j.matchemphys.2012.12.044

[82] Qu J., Liu G., Wang Y., Hong R.: Preparation of Fe_3O_4–chitosan nanoparticles used for hyperthermia. Advanced Powder Technology, **21**, 461–467 (2010).
DOI: 10.1016/j.apt.2010.01.008

[83] Scott G.: Degradable polymers: Principles and applications. Kluwer, Dordrecht (2002).

[84] Jorgensen L., Nielson H. M.: Delivery technologies for biopharmaceuticals: Peptides, proteins, nucleic acids and vaccines. Wiley, Chichester (2009).

[85] Sarasua J. R., Arraiza A. L., Balerdi P., Maiza I.: Crystallization and thermal behaviour of optically pure polylactides and their blends. Journal of Materials Science, **40**, 1855–1862 (2005).
DOI: 10.1007/s10853-005-1204-8

eXPRESS Polymer Letters Vol.10, No.3 (2016) 204–215
Available online at www.expresspolymlett.com
DOI: 10.3144/expresspolymlett.2016.19

Sequential graft-interpenetrating polymer networks based on polyurethane and acrylic/ester copolymers

R. Ballestero[1], *B. M. Sundaram*[2], *H. V. Tippur*[2], *M. L. Auad*[1*]

[1]Deparment of Chemical Engineering, Auburn University, 36849 Auburn, United States
[2]Deparment of Mechanical Engineering, Auburn University, 36849 Auburn, United States

Received 22 June 2015; accepted in revised form 4 October 2015

Abstract. Highly transparent and tough graft-interpenetrating polymer networks (graft-IPNs) were synthesized using an elastomeric polyurethane phase (PU) and a highly stiff acrylate-base copolymer phase. The grafting points between the two networks were generated with the purpose of minimizing the phase separation process of the polymeric systems. In order to generate the grafting between the networks, an acrylic resin capable of undergoing both free radical and poly-addition polymerization was employed. The thermo-mechanical properties, fracture toughness properties as well as network and surface phase morphology of the graft-IPNs synthesized were evaluated in this work. Data obtained suggested that the minimization of the phase separation was achieved by the generation of crosslinking points between both networks. High transparency was obtained in all samples as an indication of the high level of interpenetration achieved. The relative high values obtained for the fracture toughness tests suggest that generating chemical crosslinks between networks is a good approach for increasing the fracture toughness of polymeric materials.

Keywords: *thermal properties, graft-IPNs, fracture toughness, BisGMA, sequential polymerization*

1. Introduction

Over the past decades, polymer blends also known as multiphase polymeric systems have been employed in a broad number of design applications that require high resistance to fracture, a highly desired characteristic for virtually all engineering materials [1]. These polymeric materials became appealing due to their low density when compared with other engineering materials, due to the ability to synergistically incorporate properties of their individual components and achieve materials with better mechanical properties than the original constituents, as well as for their transparency [2]. The challenges with these multiphase systems are to improve their compatibility and interfacial adhesion between phases, so as to guarantee the desired performance of the final material. It is known that only a relatively small number of polymer pairs form miscible blends, mostly because of these blends have low entropy of mixing. Although the entropy of mixing favors the miscibility of a given system, it also depends on the number of molecules per unit volume. Thus, the higher the molecular weight of the polymers involved, the fewer molecules per unit volume and the lower the entropy of mixing. And since the heat of mixing of polymers pairs is generally unfavorable, polymer blends tend to macroscopically phase separate, leading to systems with poor mechanical properties [3–5]. In order to overcome this problem, many efforts have been made to find different ways to improve the miscibility of multiphase systems, one of this approaches involves the use of interfacial agents. These agents decrease the average domain size of the disperse phase by acting as steric barriers at the interphase

*Corresponding author, e-mail: auad@auburn.edu

region, enhancing the level of interactions between the polymer phases [6–8].

Another well-known method to minimize phase separation in a polymeric system is through interpenetrating polymer networks (IPNs). Mignard *et al.* [5] define an interpenetrating polymer network as a system constituted by two or more polymer networks partially interlaced on a polymeric scale but not chemically crosslinked. Different kinds of IPNs can be found based on the synthesis method; the two most common methods for their synthesis are sequential and simultaneous polymerization [5]. In the synthesis of IPNs, at least one of the polymers in the system is in the form of a monomer, and since most monomers are small molecules they have appreciable entropy of mixing. Also, the presence of physical interlocks give to the IPNs a more uniform phase structure than those of the parent polymer blends, leading to what is called forced miscibility, since the compatibility is not achieved by the mixing enthalpy or entropy [5, 9]. Nevertheless, IPNs usually present some degree of phase separation at some stage of the synthesis. For instance, it has been observed that synthesis of IPNs by simultaneous method results in phase separation [10]. Phase separation in sequential polymerization has also been observed, here, the entropy of mixing is lost during the second polymerization, due to the increase in size of the molecules as the polymerization continues [4]. In early works done by Chen *et al.* [11] and Fan *et al.* [12] they reported the implementation of a vinyl ester resin (VE) with a polyurethane network for the synthesis of simultaneous interpenetrating polymer networks. This VE resin was capable of undergoing both free radical polymerization as well as stepwise polymerization. Here the formation of crosslinks between networks was never the objective. Furthermore, the generation of crosslinks was in fact avoided. Studies on the morphology showed clearly that more than one phase was present in the system, as a result of the phase separation between networks.

In the present work, we addressed the phase separation problem of IPNs by generating chemical crosslink points between two networks, thus, generating a class of IPNs called graft-IPNs as seen in Figure 1a. The graft-IPNs synthesized in this work consisted of a highly stiff copolymer phase, which comprises bisphenol A bis(2-hydroxy-3-methacryloxypropyl) ether (BisGMA) resin and two acrylic monomers: methyl methacrylate (MMA) and triethylene glycol dimethacrylate (TEDGMA), and a soft, rubbery polyurethane phase (PU) with a high capability of energy absorption. The crosslinking of the two networks is accomplished by means of the BisGMA resin. This resin has terminal double bonds and secondary hydroxyl groups, which allows the resin to react with the acrylic monomers by radical polymerization, as well as undergo a polyaddition between the secondary (–OH) groups and the (NCO) groups of the isocyanate [13–15], as seen in Figure 1b.

The synthesis of graft-IPNs was carried out using the sequential methodology, where the PU phase was polymerized first. Then the copolymer, which was swelling the elastomeric phase, was polymerized *in situ* within the PU network. The thermomechanical properties, fracture properties as well as the phase morphology of the graft-IPNs were studied in this work.

2. Experimental

2.1. Materials

For the synthesis of the polyurethane phase (PU), two polyols were employed: 2-ethyl-2-(hydroxymethyl)-

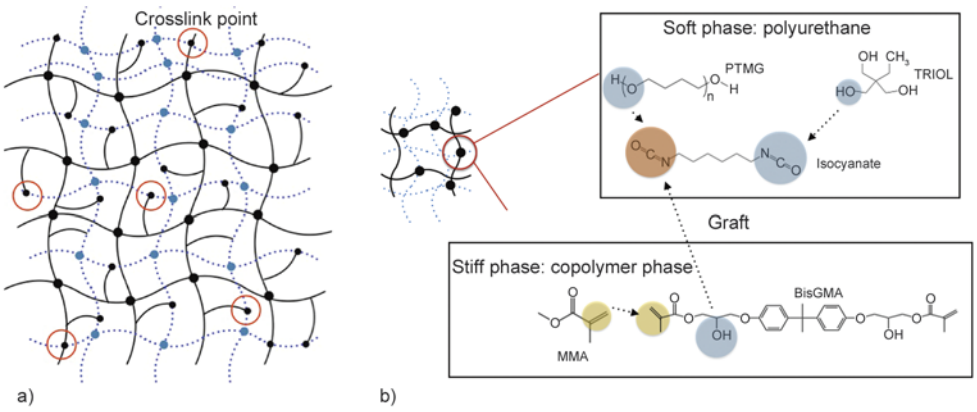

Figure 1. a) Scheme of a graft-IPN, b) scheme of graft formation

1,3propanediol (TRIOL) from Acros Organics, (USA) and poly(tetramethylene ether) glycol (PTMG) average $M_n \sim 650$ and ~ 1400 g·mol^{-1} from Sigma-Aldrich, (USA). Both TRIOL and PTMG were mixed beforehand, through melting. The TRIOL and PTMG mixture was melted in an oven under strong vacuum to remove moisture. This procedure was employed for the different molecular weight PTMGs. The isocyanate used was hexamethylene diisocyanate 98.0% (DCH) from TCI, (USA). Two catalysts were used for the synthesis: dibutylin dilaurate, 98% (DD) distributed by Pfaltz and Bauer, (USA) and triphenylbismuth, 99+% (TB) from Alfa Aesar, (USA). Ethyl acetate was used as an analogue for both catalysts.

The copolymer was synthetized using the bisphenol A bis(2-hydroxy-3-methacryloxypropyl) ether (BisGMA) from Esstech, (USA) and two acrylic monomers: methyl methacrylate 99% stabilized (MMA) from Alfa Aesar, (USA) or triethylene glycol dimethacrylate stabilized (TEGDMA) from TCI, (USA) (see Structure 1) while 2,2′-azobis(2-methylpropionitrile), 98% (AIBN) from Sigma-Aldrich, (USA) was used as an initiator.

2.2. Synthesis of graft-IPNs

The synthesis of the different graft-IPN systems was carried out in a single-step procedure. Both the copolymer phase and the PU phase were prepared separately at room temperature conditions.

First, the copolymer was prepared by mixing the acrylic monomer (MMA or TEGDMA) with the BisGMA resin, keeping a mass ratio of 90:10 acrylate:BisGMA. The amount of radical initiator employed for the polymerization was 1 wt% of the total copolymer mass. For the polyurethane phase, the DCH was added to the PTMG/TRIOL mixture. The following ratio was used to synthesize all polyurethane networks, 0.19 eq TRIOL:0.12 eq PTMG: 0.31 eq DCH. In order to generate the crosslink points between networks, an additional quantity of DCH was added to the polyurethane precursor solution in a eq ration of 1:1 DCH:BisGMA. Then, the polyurethane precursors were added to the copolymer precursor solution. Following this, DD and TB were added to catalyze the polyurethane system. After mixing both solutions, all samples were placed in an oven at 40 °C for 17 h after which the samples were transferred to a water bath where the temperature was raised to 60 °C for 24 h and finally the temperature was raised to 80 °C for 24 h.

Several graft-IPN formulations were prepared following the above-mentioned procedure. The ratio of copolymer to polyurethane content changed from 90 wt% copolymer and 10 wt% PU to 50 wt% copolymer and 50 wt% PU, this was reproduced for the 650 and 1400 g·mol^{-1} PTMG methyl methacrylate based graft-IPNs, as well as for the 650 g·mol^{-1} PTMG triethylene glycol dimethacrylate based graft-IPNs.

2.3. Characterization of graft-IPNs

Fourier transform infrared spectroscopy (FT-IR) was done using a Thermo Scientific Nicolet™ 6700 spectrometer in attenuated total reflection (ATR) infrared mode. The analysis was carried out within the frequency range of 4000–400 cm^{-1} by co-adding 32 scans and at a resolution of 2 cm^{-1}.

Dynamic mechanical analysis (DMA) on a TA Instruments RSA III was carried out to assess the thermomechanical properties by three-point bending. The tests were performed at temperatures ranging from -45 to 200 °C with a heating rate of 5 °C/min. The frequency was fixed a 1 Hz and a sinusoidal strain-amplitude of 0.1% was used for the analysis. The dynamic storage modulus (E') and tan δ curves were plotted as a function of temperature. The temperature at the maximum in the tan δ curve was taken as the T_g. The E' at $T_g + 50$ °C was chosen as the rubbery plateau modulus, E_R, for each system.

The average molecular weight between crosslinks (M_C) for the 650 and 1400 g·mol^{-1} PU based systems was calculated using Equation (1), which is based on the theory of rubber elasticity [16]:

$$M_C = \frac{3\rho RT}{E_R} \tag{1}$$

where ρ is the density of the sample; T is the temperature [K]; R is the universal gas constant, and E_R is the storage modulus in the rubbery plateau at temperature T.

Transmission electron microscopy (TEM) on a Zeiss EM 10C 10CR microscope was used to study the morphology of the different networks. Samples were prepared using Kato's osmium tetroxide (OsO_4) staining method, as described elsewhere

[17]. All samples were stained for 48 hours prior to analysis.

UV- Vis transmittance spectra were collected for the various ratios of MMA based copolymer to 650 and 1400 g·mol^{-1} PTMG based polyurethane. A UV-Vis 2450 spectrophotometer from Shimadzu Scientific Instruments was employed to acquire the spectra data. All samples were analyzed in the 900–400 nm range.

Scanning electron microscopy (SEM) on a Zeiss EVO 50 variable pressure scanning electron microscope with digital imaging and EDS (were the graft-IPNs were sputter coated with an EMS 550X auto sputter coating device with carbon coating attachment) was used to study the fracture surfaces of the 1400 g·mol^{-1} PTMG based system.

In order to characterize the fracture toughness of the graft-IPNs synthesized, in terms of the critical stress intensity factor, KIC, quasi-static fracture tests were performed. The cured graft-IPN sheets were machined into rectangular coupons of dimensions 70 mm×20 mm and 2.8 mm thickness in case of 650 g·mol^{-1} PTMG methyl methacrylate based graft-IPNs and 70 mm×15 mm and 2.8 mm thickness for 1400 g·mol^{-1} PTMG methyl methacrylate based graft-IPNs. An edge notch of 3 mm in length was cut into the samples, and the notch tip was sharpened using a razor blade. An Instron 4465 universal testing machine was used for loading the specimen in tension and in displacement control mode (crosshead speed = 1 mm/min). The load-deflection data was recorded up to crack initiation and during stable crack growth, if any. The crack initiation toughness or critical stress intensity factor, K_{IC}, was calculated using the load (F) recorded at crack initiation. For each graft-IPN category, at least three sets of experiments were performed at laboratory conditions. The mode-I stress intensity factor for a single edge notched (SEN) tensile strip using linear elastic fracture mechanics is given by Equation (2) [18]:

$$K_{\mathrm{Ic}} = \frac{F\sqrt{\pi a}}{Bw} f\left(\frac{a}{w}\right) \tag{2}$$

where $f(a/w)$ is calculated from Equation (3):

$$f\left(\frac{a}{w}\right) = \left[1.12 - 0.23\left(\frac{a}{w}\right) + 10.6\left(\frac{a}{w}\right)^2 - 21.7\left(\frac{a}{w}\right)^3 + 30.4\left(\frac{a}{w}\right)^4\right] \tag{3}$$

where a is the edge crack length, w is the specimen width, B is the specimen thickness and F is the peak load.

To characterize the tensile properties of graft-IPNs in terms of the elastic modulus, yield and ultimate stresses, quasi-static tension tests were performed. For quasi-static tension tests, the cured graft-IPN sheets were machined into dumbbell shaped specimen, which was inspired by ASTM D638 test method [19]. The size of the sheets that could be prepared precluded a complete adherence to ASTM standards. An Instron 4465 universal testing machine was used for loading the specimen in tension and in displacement control mode (crosshead speed = 1 mm/min). An extensometer with 0.25" gauge length was used to record the strain. The load vs strain data was recorded up to 7% strain for 650 g·mol^{-1} PTMG methyl methacrylate based graft-IPNs and up to 20% strain for 1400 g·mol^{-1} PTMG methyl methacrylate based graft-IPNs. Using the geometry of the specimen, stress was evaluated from load measurements to obtain stress vs strain data. For each graft-IPN category, at least three sets of experiments were performed at laboratory conditions. The elastic modulus was evaluated from the slope of the stress-strain curve at less than 2% strain.

Scanning electron microscopy (SEM) on a Zeiss EVO 50 variable pressure scanning electron microscope with digital imaging and EDS (were the graft-IPNs were sputter coated with an EMS 550X auto sputter coating device with carbon coating attachment) was used to study the fracture surfaces of the 1400 g·mol^{-1} PTMG based system.

3. Results and discussion

3.1. Analysis of FTIR measurements

In order to monitor the polymerization process of the polyurethane network infrared spectra were recorded. The analysis if based on the peak change of the functional group isocyanate (NCO) and acrylic double bond during the reaction time. The isocyanate absorption band is assigned at approximately 2300–2200 cm^{-1} in the mid infrared spectrum and its decay can be used to follow the conversion of the NCO

group during the polymerization. For scaling the decrease of the NCO absorbance, the C–H stretch absorption (approx. 2960 cm^{-1}) was used as an internal standard as shown in Figure 2a, since its concentration does not change during the reaction. For the analysis it was assumed that there are no side reactions, and the isocyanate conversion was calculated as shown by Equation (4) [20]:

$$\text{Isocyanate conversion } p = 1 - \frac{\frac{A_{NCO}}{A_{CH_2}}}{\left(\frac{A_{NCO}}{A_{CH_2}}\right)_0} \qquad (4)$$

where A_{NCO} is the integrated absorbance for the isocyanate group, A_{CH_2} is the integrated absorbance for the CH_2 group and $(A_{NCO}/_{ACH2})_0$ is the relative absorbance extrapolated for time zero. All experiments were carried out at temperatures and times use for the synthesis of graft-IPNs. Figure 2b shows the results from the FTIR experiments and the corresponding NCO conversion curves. The samples analyzed by infrared spectroscopy were: 70:30 copolymer:PU graft-IPN, pure PU, PU+BisGMA and DCH+BisGMA. All samples were synthesized using the 650 $g \cdot mol^{-1}$ PTMG. From Figure 2b it can be seen that the PU network and the graft-IPN reached very similar conversion values after 3900 minutes of reaction. One can also notice that the conversion value for the NCO on the graft-IPN sample was close to 93%. For this sample in particular a NCO conversion above 82% is an indication of the reaction of the secondary hydroxyl groups present in the BisGMA resin with free NCO groups in the PU network. Since 18% of the total NCO present in the sample is added with the sole purpose of generating grafts between networks, this means that 62% of the total possible grafts were generated during the reaction time. Moreover, by analyzing these curves it seems that the presence of the methyl methacrylate monomer does not have a strong influence in the formation of the PU network in the graft-IPN system, since their conversion curves are practically overlapping.

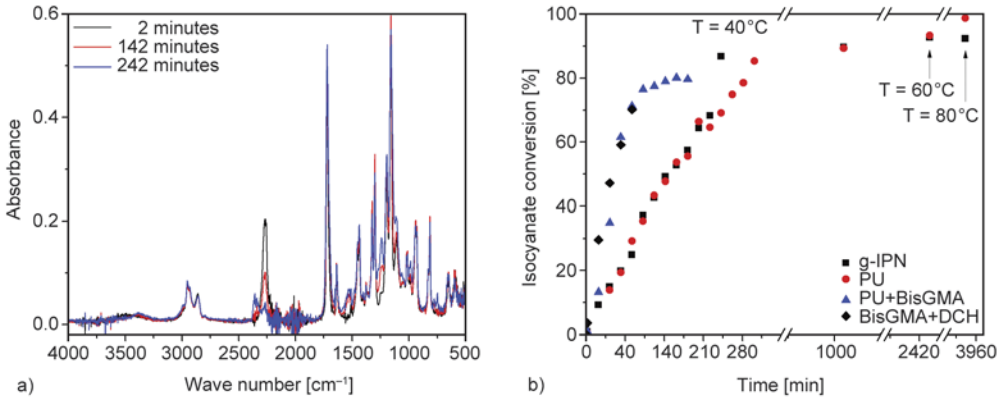

Figure 2. a) FTIR of graft-IPNs at different times during the curing process, b) isocyanate conversion plot

Table 1. Storage modulus (E'), glass transition temperature (T_g), storage modulus at the rubbery plateau (E_R) and M_C for the different graft-IPNs synthesized

Sample	Copolymer content [wt%]	E' at 25 °C [Pa]	T_g [°C]	E_R [Pa]	M_C [$g \cdot mol^{-1}$]
Graft-IPN with 650 $g \cdot mol^{-1}$ PTMG	90	$3.35 \cdot 10^9$	120	$1.20 \cdot 10^7$	890
	80	$3.02 \cdot 10^9$	110	$1.80 \cdot 10^7$	637
	70	$2.07 \cdot 10^9$	98	$1.57 \cdot 10^7$	910
	60	$1.40 \cdot 10^9$	97	$1.84 \cdot 10^7$	655
	50	$0.96 \cdot 10^9$	83	–	–
Graft-IPN with 1400 $g \cdot mol^{-1}$ PTMG	90	$2.73 \cdot 10^9$	120	$1.04 \cdot 10^7$	1360
	80	$2.36 \cdot 10^9$	107	$1.36 \cdot 10^7$	907
	70	$1.39 \cdot 10^9$	97	$9.77 \cdot 10^6$	1265
	60	$0.95 \cdot 10^9$	83	$1.18 \cdot 10^7$	1030
	50	$0.41 \cdot 10^9$	72	–	–
Graft-IPN with 650 $g \cdot mol^{-1}$ PTMG Tri-EDMA	90	$5.28 \cdot 10^9$	141	–	–
	80	$4.41 \cdot 10^9$	121	–	–
	70	$1.08 \cdot 10^9$	118	$1.73 \cdot 10^8$	72
	60	$0.62 \cdot 10^9$	116	–	–

Figure 2a also shows how similar the PU+BisGMA and DCH+BisGMA conversion curves are. One could speculate that the secondary hydroxyl groups from the BisGMA resin are reacting throughout the entire reaction time and not only when the primary hydroxyl groups coming from the PTMG and TRIOL are depleted. Regarding follow up of the copolymer network formation, the conversion of the acrylic double bonds absorption band in the 1630–1650 cm^{-1} was monitored. Although since the data were gathered in the solid state rather than the liquid stated, the data collected was not sufficiently accurate to allow a proper determination of the final double bond conversion of the copolymer network present in the sample. The extent of reaction at the gel point was determined experimentally and theoretically for the samples under analysis. The latter was obtained using Flory and Stockmayer statistical approach to gelation as describe elsewhere [21]. From Table 1 it can be seen that the extent of reaction determined experimentally are really close to the theoretical ones.

3.2. Thermo-mechanical characterization

The variables studied in the present work included the ratio of copolymer to PU, the molecular weight of poly (tetramethylene ether) glycol (PTMG) and the acrylic monomer employed to synthesize the copolymer phase. The ratio between the di- to tri-functionalized monomers (PTMG:TRIOL) for the PU phase was kept constant, since it is related to the crosslink density of the PU network. The ratio between the acrylic monomers to BisGMA resin was also kept constant. The number of possible crosslinks between networks is bounded by the reaction of secondary OH groups present in the BisGMA resin and the free isocyanate groups present in the PU network. If the acrylic monomer to BisGMA ratio were to be changed, the moles of the latter resin would change, thus, altering the number of secondary OH group available for grafting.

All variables under study showed a major impact on the storage modulus of the systems. However, only the ratio of copolymer to PU and the acrylic monomer used had a significant effect on the T_g of the systems. Figure 3 shows the thermo-mechanical properties (storage modulus, E', and $\tan\delta$) of the graft-IPNs synthesized using the 650 $g \cdot mol^{-1}$ PTMG as a function of temperature. In addition, Table 2 summarizes the results for all the different systems studied.

For all systems under study, it was observed that as the copolymer content increased, the samples exhibited higher values for the storage modulus, E'; a highly expected result since the copolymer phase provides the stiffness to the system. Samples consisting of 90 wt% copolymer showed a storage modulus of 3.35, 2.73 GPa at 25 °C for the 650 and 1400 $g \cdot mol^{-1}$ PTMG methyl methacrylate based graft-IPNs. While for the TEGDMA based graft-IPNs a value of 5.28 GPa at 25 °C was obtained using the 650 $g \cdot mol^{-1}$ PTMG. Samples containing less than 70 wt% of copolymer showed inferior values for the storage modulus, which can be attributed to the elastomeric contribution of the PU phase. When comparing the systems with different molecular weight PTMGs, a substantial difference in the storage modulus was observed. As shown in Table 2, the storage modulus values for the system using the 1400 $g \cdot mol^{-1}$ PTMG are inferior to those of the 650 $g \cdot mol^{-1}$. This

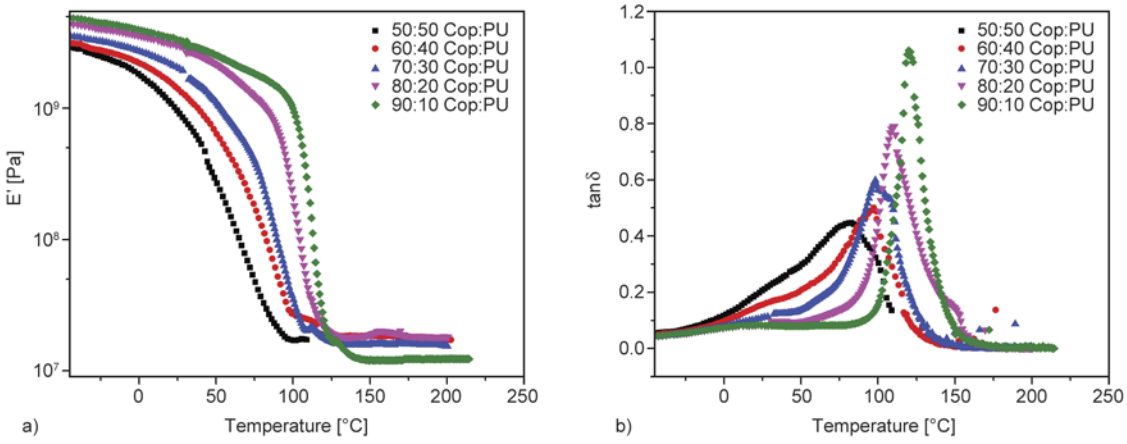

Figure 3. DMA results showing change in (a) E' and (b) tan δ for graft-IPNs with various ratio of MMA based copolymer to 650 $g \cdot mol^{-1}$ PTMG based polyurethane

Table 2. Results obtained for the fracture toughness tests performed on different graft-IPNs synthesized

Sample	Copolymer content [wt%]	K_{Ic} [MPa·m$^{1/2}$]	E [GPa]	Ultimate stress [MPa]	Failure strain [%]
Graft-IPN with 650 g·mol^{-1} PTMG	90	1.17±0.03	3.3±0.05	61.79	3.05
	80	1.16±0.14	3.6±0.03	47.97	2.155
	70	2.70±0.09	2.2±0.02	35.78	>7
	60	1.84±0.06	1.3±0.04	18.06	>7
Graft-IPN with 1400 g·mol^{-1} PTMG	90	1.49±0.05	3.4±0.05	76.50	10.80
	80	2.35±0.08	2.65±0.08	52.29	>20
	70	2.95±0.12	2.5±0.11	34.27	>20
	60	1.73±0.04	1.2±0.08	18.11	>20
Graft-IPN with 650 g·mol^{-1} PTMG Tri-EDMA	70	0.77±0.02	–	–	–

reduction in the storage modulus may be explained by the higher mobility that a longer macrodiol provides to the PU network [10]. When analyzing the storage modulus of the TEGDMA-based samples (see Table 2), it can be seen that the substitution of a single double bond monomer (MMA) in the copolymer for a monomer with two double bonds (TEGDMA) had a major impact on the storage modulus. Samples containing this dimethacrylate monomer had a tendency to present higher storage modulus than those synthesized using MMA. As described by Heatley *et al*. [22], BisGMA-TEGDMA copolymers are characterized by presenting high degrees of crosslinking, due to presence of two double bonds in their chemical structures, which generated more crosslink points within the copolymer network, resulting in an increase in the crosslink density of the network. This increase in the crosslink density diminished to a certain extent the mobility of the network chains, increasing the stiffness of the system, thus, increasing the storage modulus of the samples. To corroborate this statement, the M_C of the MMA and TEGDMA graft-IPNs were experimentally estimated by measuring the equilibrium storage modulus in the rubbery state, using the Equation (1) from the theory of rubber elasticity. The samples analyzed were the 70% copolymer content using the 650 g·mol^{-1} PTMG. The results showed M_C values of 910 and 72 g·mol^{-1} for the MMA and TEGDMA samples respectively. As expected the dimethacrylate-based sample showed the lowest value for M_C, which as stated earlier, provides an explanation for the higher values of storage modulus obtained for all TEGDMA-based samples over its MMA-based counterparts.

Figure 3b, shows the plot of tan δ as a function of temperature for the MMA based graft-IPNs synthesized using the 650 g·mol^{-1} PTMG. In this graph, a maximum peak of the loss factor showed the characteristic relaxation associated with the glass transition temperature of the different systems under study. It was observed that as the weight percentage of copolymer increased in the samples, the maximum peak of the loss factor gained prominence and moved to higher temperatures. The narrow peak of the loss factor in the sample with 80 and 90% copolymer content suggested a high degree of miscibility. For the rest of the samples a broad transition with a shoulder related to the glass transition of the PU phase was observed in the curves, which it is characteristic of a partially miscible system. A similar peak in the loss factor for the 90% copolymer content was also observed for the composition using the 1400 g·mol^{-1} PTMG, as well as broader transitions for samples containing <90 weight percentages of copolymer. This suggests that several different relaxation mechanisms are present in the produced network, and they may be related to the nano-heterogeneity of the system [10, 17].

In the case of the TEGDMA-based graft-IPNs, all samples presented broad transitions, also suggesting a high level of heterogeneity in the system. However, in the case of dimethacrylates, the heterogeneity formed, as explained by Podgórsky [23], results from highly crosslinked structures in which a broad distribution of micro-domains can be found. This kind of polymer networks have shown both loosely connectivity and highly crosslinked regions, as well as regions were unreacted monomer is present. This lack of homogeneity in the network structure has as a result the manifestation of a broad distribution of relaxation times due to the matrix mobility.

3.3. Network morphology

The network morphology of the graft-IPN was studied to corroborate the improvement achieved in the interpenetration of the two polymer networks as a result of the chemical crosslink between networks.

Figure 4 shows TEM photos of sections cut from stained methyl methacrylate copolymer based graft-IPN samples containing 70% copolymer content with different molecular weight PTMGs at different stages of the curing process. Here, the dark zones correspond to PU regions, since the PU phase is the one that absorbed the dye, while the clear zones correspond to the copolymer phase.

In general, the morphology presented by different IPNs is rather complex, since different competing processes may occur simultaneously during polymerization. In sequential polymerization; as is the case in this work, the formation of the first network has a major impact on the formation of the second, limiting the range of compositions and the material's final properties obtained by following this synthetic route.

As shown in Figure 4c, it appears to be a slight formation of PU domains for the 1400 g·mol^{-1} PTMG graft-IPNs at 60 °C. As the curing process of the samples was finalized after 24 h at 80 °C, the PU domains seemed to disappear (see Figure 4d). This observation may be explained by further formation of crosslink points between the two networks by means of the reaction between the hydroxyl groups present in the BisGMA resin with the isocyanate groups present in the PU phase. These TEM pictures are a corroboration of the decrease in size of these domains by the formation of the aforementioned crosslinking points, which improved the system's miscibility, thus minimizing the phase separation between networks [10]. Furthermore, when comparing the two graft-IPNs with different molecular

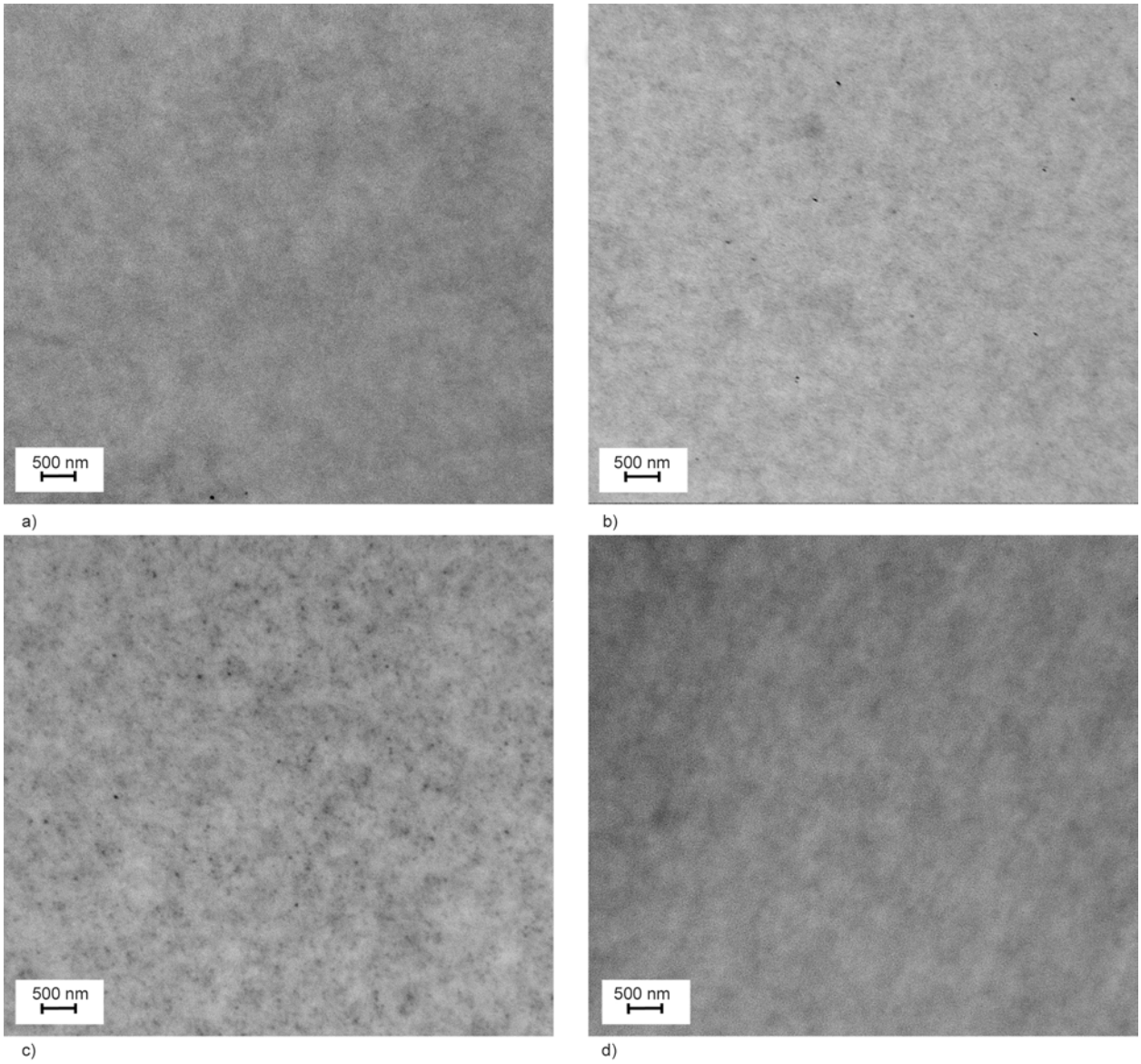

Figure 4. TEM photos of graft-IPNs with 70 wt% MMA based copolymer using the 650 g·mol^{-1} PTMG at (a) 60 °C, (b) 80 °C and 1400 g·mol^{-1} PTMG (c) 60 °C and (d) 80 °C

weight PTMGs, it can be seen from the TEM pictures that both systems presented a fine dispersion of both networks through the entire sample. This is attributed to the successful interpenetration of the two different networks at the molecular level [17].

3.4. Degree of transparency

Transparency of the MMA based copolymer using 650 g·mol^{-1} PTMG samples synthesized was analyzed. The system presented a relative high degree of transparency, showing values of transmittance between 65 and 90%, as shown in Figure 5. The same degree of transparency was also observed for the 1400 g·mol^{-1} PTMG based system. These results are also confirmation of the high degree of interpenetration achieved on both systems regardless of the molecular weight of the PTMG. There is no visible evidence of macroscopic phase separation in the samples studied, supporting the results shown in the plot of tan δ as a function of temperature.

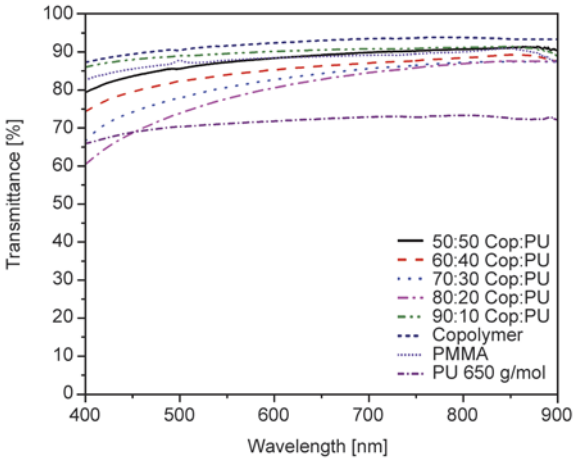

Figure 5. UV-vis spectrum of MMA based copolymer and 650 g·mol^{-1} PTMG based PU graft-IPN

3.5. Stiffness and fracture toughness

The stress vs strain plots obtained from the tension tests in case of 650 and 1400 g·mol^{-1} PTMG are shown in Figure 6a and 6b respectively. It can be seen that the modulus and the peak stress drops progressively with increase in PU resulting in no observed failure within the window of imposed strains.

Table 3 shows results obtained for the quasi-static crack initiation toughness, K_{IC} for the graft-IPNs studied. When both systems are compared, it can be seen that the graft-IPNs synthesized with the 1400 g·mol^{-1} PTMG have a slightly higher value for the quasi-static crack initiation toughness than those synthesized using the 650 g·mol^{-1} PTMG. Furthermore, it can be observed that both systems displayed the highest value of fracture toughness in samples with a 70% of copolymer content, suggesting that there is an optimum copolymer to PU ratio.

3.6. Determination of average molecular weight between crosslinks (M_C) and its relation with fracture toughness

The average molecular weight between crosslinks for the MMA based graft-IPNs was experimentally obtained by measuring the storage modulus in the rubbery plateau, E_R, at 50 °C above the glass transition temperature according to the Equation (1) from

Table 3. Determination of extend of reaction at gel point

Sample	Gel time [min]	Conversion at gel time (Experimental)	Conversion at gel time (Flory and Stockmayer)
Graft-IPN	242	87%	82 %
PU	222	69%	79%
PU+BisGMA	182	80%	82%
DCH+BisGMA	–	–	–

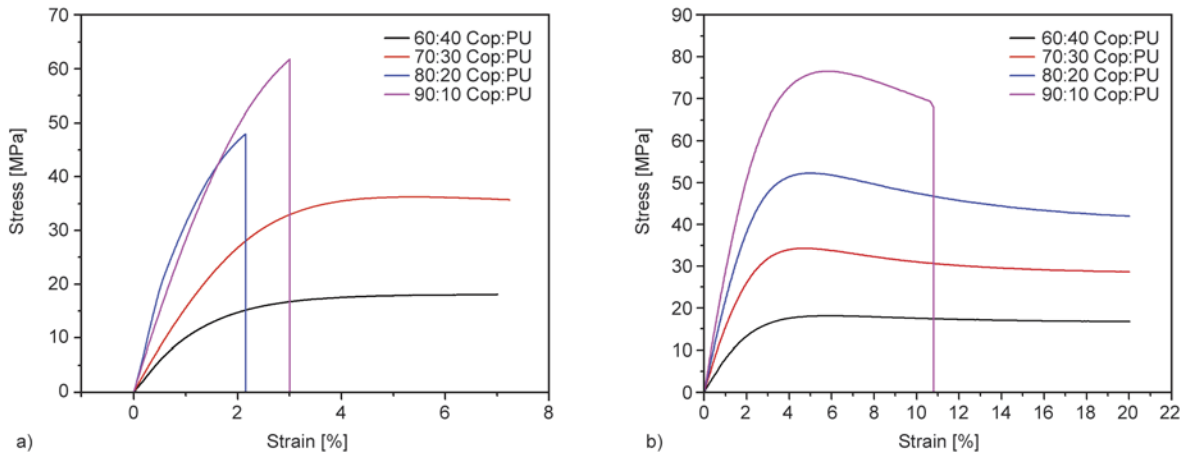

Figure 6. Stress vs. strain plots for MMA based copolymer samples using a) 650 g·mol^{-1} PTMG and b) 1400 g·mol^{-1} PTMG based polyurethane during tension test

the theory of rubber elasticity. In previous studies done by Karger-Kocsis and Gremmels [24], Liang and Pearson [25], Liu *et al.* [26], a linear correlation between the fracture toughness and M_C was found. It was seen that as M_C increased in the system the higher the K_{IC} value became. Sherman *et al.* [27] attribute this to an increase in the free volume of the materials, which allows more space resulting in an increase of chain motions capable to accommodate the applied load. Nevertheless, linear correlation was not found for the system under study, the results showed that the K_{IC} values did not increase as M_C increased. This tendency holds true for both 650 and 1400 g·mol^{-1} PTMG based graft-IPNs.

3.7. Surface morphology

In order to study the fracture mechanics of the graft-IPN systems, SEM images were taken from samples used for fracture testing. Figure 7 shows the fractured surfaces of graft-IPNs samples with different copolymer to polyurethane ratios for the graft-IPNs synthesized using the 1400 g·mol^{-1} PTMG.

From Figure 7 it can be seen that regardless of PU content present in the samples, this factor does not have a significant effect on the surface area created were the fracture propagated through the material. When compared to previous work done by Bird *et al.* [17], the authors were able to observe how an increase in the PU content in the system resulted in an increase on the surface area were the fracture propagated through the material. They also observed how the samples with a higher PU content had better fracture toughness values, which led them to correlate the surface area generated during fracture testing with the fracture toughness properties of the material. However, this correlation between an increase of surface area and fracture toughness was not observed on the graft-IPN systems. Although it was possible to see how samples with a copolymer content equal or superior to 80% show brittle fractures while samples under 80% copolymer content show did not show a brittle fracture. These results suggest that a different fracture mechanism is responsible for the improvement in the fracture toughness values presented by the graft-IPN.

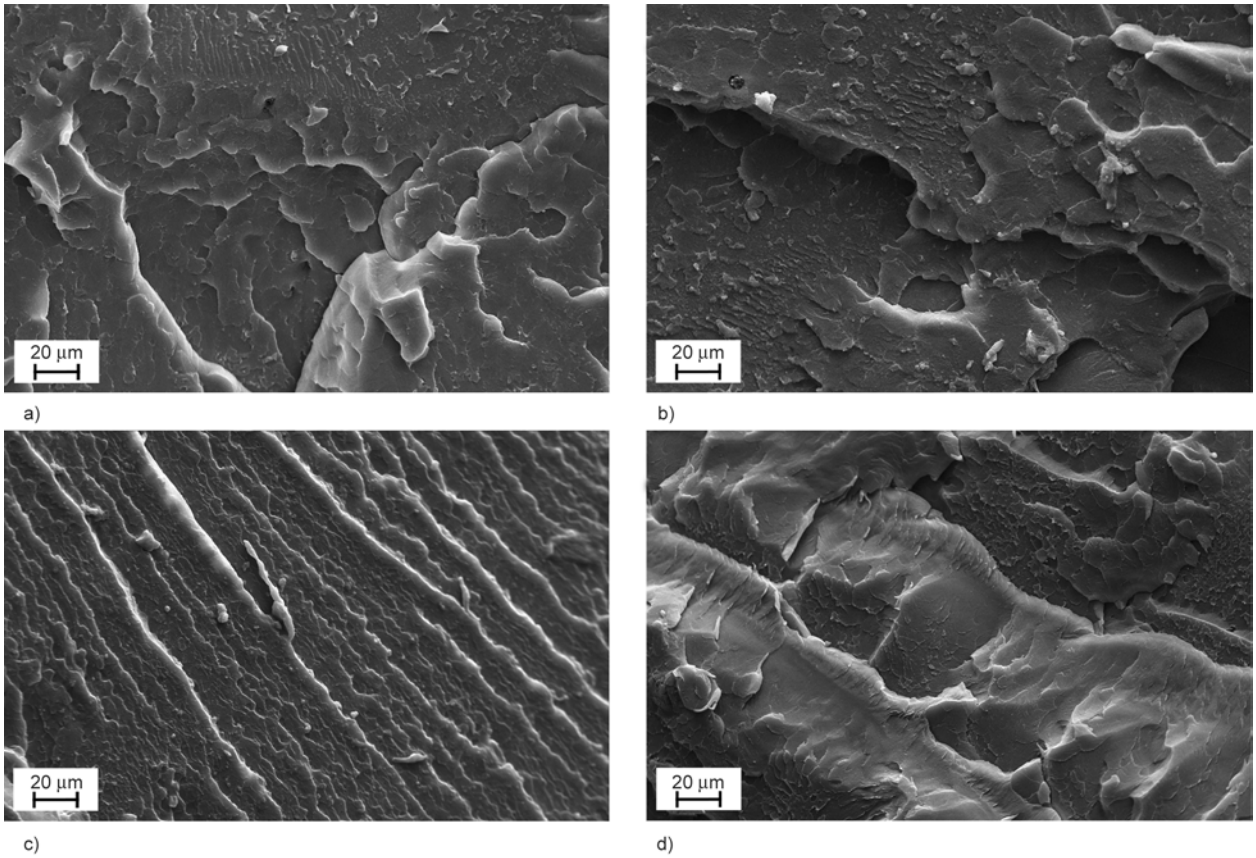

Figure 7. SEM photos of (a) 60 wt% copolymer, (b) 70 wt% copolymer, (c) 80 wt% copolymer and (d) 90 wt% copolymer MMA-graft-IPN samples using the 1400 g·mol^{-1} PTMG

4. Conclusions

In this study, a series of graft interpenetrated polymer networks consisting of a polyurethane and a copolymer network were synthesized. Where, the influence of the copolymer to PU ratio, molecular weight of the PTMG and copolymer's chemical composition on the thermo-mechanical and fracture toughness properties, as well as both network and surface morphology were systematically studied.

As expected, the findings suggest that the toughenability of the graft-IPNs synthesized was highly dependent on all three aforementioned variables. It was found that samples comprising 70wt% MMA based copolymer and 1400 g·mol^{-1} PTMG based polyurethane presented the best combination of high E', T_g and fracture toughness of all systems under study. The network morphology studies showed that there is no clear domains in any of the samples analyzed, what suggests that phase separation was successfully minimized by the generation of crosslink points between the copolymer and PU networks by means of the BisGMA resin. The surface morphology analysis suggests that a different fracture mechanism is accountable for the improvement in the fracture toughness presented by the graft-IPN systems, since there is no clear correlation between an increase on the fracture toughness and an increase in surface area were the fracture propagated in the samples. Additional work is still needed for understanding the fracture mechanism accountable for the high crack initiation toughness showed by graft-IPNs.

Acknowledgements

We kindly acknowledge the support for this research by the U.S. Army Research Office through grant W911NF-12-1-0317.

References

[1] Pfeifer C. S., Silva L. R., Kawano Y., Braga R. R.: Bis-GMA *co*-polymerizations: Influence on conversion, flexural properties, fracture toughness and susceptibility to ethanol degradation of experimental composites. Dental Materials, **25**, 1136–1141 (2009). DOI: 10.1016/j.dental.2009.03.010

[2] Mulliken A. D., Boyce M. C.: Mechanics of the rate-dependent elastic–plastic deformation of glassy polymers from low to high strain rates. International Journal of Solids and Structures, **43**, 1331–1356 (2006). DOI: 10.1016/j.ijsolstr.2005.04.016

[3] Panapitiya N. P., Wijenayake S. N., Huang Y., Bushdiecker D., Nguyen D., Ratanawanate C., Kalaw G. J., Gilpin C. J., Musselman I. H., Balkus K. J., Ferraris J. P.: Stabilization of immiscible polymer blends using structure directing metal organic frameworks (MOFs). Polymer, **55**, 2028–2034 (2014). DOI: 10.1016/j.polymer.2014.03.008

[4] Sperling L. H.: Polymeric multicomponent materials: An introduction. Wiley, New York (1997).

[5] Mignard N., Okhay N., Jegat C., Taha M.: Facile elaboration of polymethylmethacrylate/polyurethane interpenetrating networks using Diels-Alder reactions. Journal of Polymer Research, **20**, 233/1–233/13 (2013). DOI: 10.1007/s10965-013-0233-2

[6] Cerclé C., Favis B. D.: Generalizing interfacial modification in polymer blends. Polymer, **53**, 4338–4343 (2012). DOI: 10.1016/j.polymer.2012.07.027

[7] García-Martínez J. M., Laguna O., Areso S., Collar E. P.: A dynamic–mechanical study of the role of succinil-fluoresceine grafted atactic polypropylene as interfacial modifier in polypropylene/talc composites. Effect of grafting degree. European Polymer Journal, **38**, 1583–1589 (2002). DOI: 10.1016/S0014-3057(02)00051-4

[8] Wang J-J., Li Z-Z., Gu X-P., Feng L-F., Zhang C-L., Hu G-H.: A dissipative particle dynamics study on the compatibilizing process of immiscible polymer blends with graft copolymers. Polymer, **53**, 4448–4454 (2012). DOI: 10.1016/j.polymer.2012.08.030

[9] Li B. Y., Bi X. P., Zhang D. H., Wang F. S.: Forced compatibility and mutual entanglements in poly(vinyl acetate)/poly(methyl acrylate) IPNs. in 'Advances in interpenetrating polymer networks' (Klempner D., Frisch K. C.) Technomic Pusblishing, Lancaster, Vol 1, 203–219 (1989).

[10] Ramis X., Cadenato A., Morancho J. M., Salla J. M.: Polyurethane–unsaturated polyester interpenetrating polymer networks: Thermal and dynamic mechanical thermal behaviour. Polymer, **42**, 9469–9479 (2001). DOI: 10.1016/S0032-3861(01)00492-X

[11] Chen C-H., Chen W-J., Chen M-H., Li Y-M.: Simultaneous full-interpenetrating polymer networks of blocked polyurethane and vinyl ester Part I. Synthesis, swelling ratio, thermal properties and morphology. Polymer, **41**, 7961–7967 (2000). DOI: 10.1016/S0032-3861(00)00173-7

[12] Fan L. H., Hu C. P., Ying S. K.: Thermal analysis during the formation of polyurethane and vinyl ester resin interpenetrating polymer networks. Polymer, **37**, 975–981 (1996) DOI: 10.1016/0032-3861(96)87280-6

[13] Gryshchuk O., Jost N., Karger-Kocsis J.: Toughening of vinylester–urethane hybrid resins by functional liquid nitrile rubbers and hyperbranched polymers. Polymer, **43**, 4763–4768 (2002). DOI: 10.1016/S0032-3861(02)00314-2

[14] Jost N., Karger-Kocsis J.: On the curing of a vinylester–urethane hybrid resin. Polymer, **43**, 1383–1389 (2002). DOI: 10.1016/S0032-3861(01)00702-9

[15] Karger-Kocsis J., Fröhlich J., Gryshchuk O., Kautz H., Frey H., Mülhaupt R.: Synthesis of reactive hyperbranched and star-like polyethers and their use for toughening of vinylester–urethane hybrid resins. Polymer, **45**, 1185–1195 (2004). DOI: 10.1016/j.polymer.2003.12.050

[16] Cho K., Lee D., Park C.: Effect of molecular weight between crosslinks on fracture behaviour of diallylterephthalate resins. Polymer, **37**, 813–817 (1996) DOI: 10.1016/0032-3861(96)87258-2

[17] Bird S. A., Clary D., Jajam K. C., Tippur H. V., Auad M. L.: Synthesis and characterization of high performance, transparent interpenetrating polymer networks with polyurethane and poly(methyl methacrylate). Polymer Engineering and Science, **53**, 716–723 (2013). DOI: 10.1002/pen.23305

[18] Janssen M., Zuidema J., Wanhill R. J. H.: Fracture mechanics. Delft Academic Press/VSSD, Delft (2006).

[19] ASTM D638: Standard test method for tensile properties of plastics (2014).

[20] Cateto C. A., Barreiro M. F., Rodrigues A. E.: Monitoring of lignin-based polyurethane synthesis by FTIR-ATR. Industrial Crops and Products, **27**, 168–174 (2008). DOI: 10.1016/j.indcrop.2007.07.018

[21] Odian G.: Principles of polymerization. Wiley, New York (2004).

[22] Heatley F., Pratsitsilp Y., McHugh N., Watts D. C., Devlin H.: Determination of extent of reaction in dimethacrylate-based dental composites using solid-state ^{13}C m.a.s. n.m.r. spectroscopy and comparison with *FT*i.r. spectroscopy. Polymer, **36**, 1859-1867 (1995). DOI: 10.1016/0032-3861(95)90932-R

[23] Podgórski M.: Structure–property relationship in new photo-cured dimethacrylate-based dental resins. Dental Materials, **28**, 398–409 (2012). DOI: 10.1016/j.dental.2011.11.013

[24] Karger-Kcosis J., Gremmels J.: Use of hygrothermal decomposed polyester–urethane waste for the impact modification of epoxy resins. Journal of Applied Polymer Science, **78**, 1139–1151 (2000). DOI: 10.1002/1097-4628(20001031)78:5<1139::AID-APP240>3.0.CO;2-Q

[25] Liang Y. L., Pearson R. A.: Toughening mechanisms in epoxy–silica nanocomposites (ESNs). Polymer, **50**, 4895–4905 (2009). DOI: 10.1016/j.polymer.2009.08.014

[26] Liu J., Sue H-J., Thompson Z. J., Bates F. S., Dettloff M., Jacob G., Verghese N., Pham H.: Effect of crosslink density on fracture behavior of model epoxies containing block copolymer nanoparticles. Polymer, **50**, 4683–4689 (2009). DOI: 10.1016/j.polymer.2009.05.006

[27] Sherman C. L., Zeigler R. C., Verghese N. E., Marks M. J.: Structure–property relationships of controlled epoxy networks with quantified levels of excess epoxy etherification. Polymer, **49**, 1164–1172 (2008). DOI: 10.1016/j.polymer.2008.01.037

eXPRESS Polymer Letters Vol.10, No.3 (2016) 216–226
Available online at www.expresspolymlett.com
DOI: 10.3144/expresspolymlett.2016.20

Preparation and characterization of cationic Pluronic for surface modification and functionalization of polymeric drug delivery nanoparticles

G. Gyulai[1], *A. Magyar*[2], *J. Rohonczy*[3], *J. Orosz*[1], *M. Yamasaki*[1,4], *Sz. Bősze*[2], *É. Kiss*[1*]

[1]Laboratory of Interfaces and Nanostructures, Institute of Chemistry, Eötvös Loránd University, Budapest 112, PO Box 32, H-1518 Budapest, Hungary
[2]MTA-ELTE Research Group of Peptide Chemistry, Budapest 112, PO Box 32, H-1518 Budapest, Hungary
[3]Department of Inorganic Chemistry, Institute of Chemistry, Eötvös Loránd University, Budapest 112, PO Box 32, H-1518 Budapest, Hungary
[4]GENMAT – Chemistry Department, Federal University of Mato Grosso, Cuiabá/MT – 78060-900, MT – Brazil

Received 16 July 2015; accepted in revised form 4 October 2015

Abstract. Biodegradable poly(lactic-*co*-glycolic acid) copolymer, PLGA nanoparticles (NPs) with a surface layer of poly (ethylene oxide)-poly(propylene oxide)-poly(ethylene oxide) triblock copolymers, Pluronics, are promising drug carrier systems. With the aim to increase the potential of targeted drug delivery the end group derivative of Pluronics was synthesized in a straightforward way to obtain Pluronic-amines. The formation of functional amine groups was confirmed by fluorescamine method and NMR analysis of their N-(tert-Butoxycarbonyl)-L-phenylalanine (Boc-Phe-OH) and N-(9-Fluorenylmethoxycarbonyl)-L-phenylalanine (Fmoc-Phe-OH) conjugates. Pluronic and Pluronic-amine stabilized PLGA NPs prepared by nanoprecipitation were characterized by dynamic light scattering and zeta potential measurements. All of the systems showed high colloidal stability checked by electrolyte induced aggregation, although the presence of Pluronic-amine on the surface decreased the zeta potential in some extent. The introduction of reactive primary amine groups into the surface layer of PLGA NPs while preserving the aggregation stability, provides a possibility for coupling of various ligands allowing targeted delivery and also contributes to the improved membrane affinity of NPs.

Keywords: *biocompatible polymers, Pluronic derivatization, PLGA nanoparticles, colloidal stability, polymeric drug delivery*

1. Introduction

Extensive research went into the development of drug delivery systems in the past decades to reduce the side effects and enhance the therapeutic efficacy of drugs [1]. Biodegradable polymeric nanoparticles (NPs) offer the possibility for prolonged drug release as well as targeted delivery. Poly(lactic-*co*-glycolic acid) copolymers (PLGA) are preferred biomaterials because of their nontoxicity, biocompatibility and biodegradability [2–6]. PLGA readily forms NPs via the nanoprecipitation method as described by Fessi *et al*. [7]. In most cases the drug is encapsulated into the polymeric particle and released in a controlled way by diffusion and erosion of the polymeric matrix [8–11]. It was found however, that the hydrophobic character of the PLGA triggers the nonspecific adsorption of plasma proteins leading to the uptake of the particles by the mononuclear phagocyte system and hence their fast clearance from the body [12–14]. This undesirable process can be prevented by forming a poly(ethylene oxide), PEO corona on the particle to improve its surface biocompatibility [15–18]. Among the various techniques developed for surface immobilization of PEO the

*Corresponding author, e-mail: kisseva@chem.elte.hu

adsorption of poly(ethylene oxide)-poly(propylene oxide)-poly(ethylene oxide) triblock copolymers, the use of Pluronics is a versatile and convenient method to obtain PEO-rich surface on PLGA NPs. The hydrophobic PPO part of the molecule facilitates the anchorage of the surface modifier to the PLGA while the PEO chains form an outer layer introducing steric stability to the NPs [19–22]. In addition to reduced protein adsorption and reasonable colloidal stability the capability of NPs to cross cell membranes and intracellular barriers is also a requirement in drug carrier applications. Previous studies demonstrated that the presence of certain Pluronics on the surface of the PLGA NPs enhances the nonspecific membrane affinity of the system [23]. The specific targeting needs the conjugation of appropriate biospecies to the surface of NPs. PLGA particles contain chain end carboxylic groups on their surface but these are small in number and not easily accessible because of the presence of the Pluronic molecules on the surface. The surface Pluronic layer on the other hand contains only hydroxyl groups at the chain ends which have limited reactivity under normal conditions. Introduction of reactive amino groups onto the surface would provide a convenient way for immobilization of the desired ligand.

Transformation of Pluronic end groups into amine is the aim of our work and furthermore to reveal whether this change influences the physico-chemical and drug carrier properties of the Pluronic stabilized PLGA NPs.

Formation of amine end groups on PEO molecules can be achieved by various methods which usually involve two or more reaction steps. One of those is the conversion of the hydroxyl groups to halide or sulfonyl ester, followed by a reaction with excess amount of ammonia [24, 25]. Another strategy for the introduction of amine functionality is by activating the hydroxyl groups followed by conjugation with diamines and polyamines [26, 27]. A problem with these reactions is the possibility for secondary amine side product formation as well as the risk of cross-linking [28]. Harris *et al*. [29] described a straightforward, two step reaction for the preparation of PEO-amines that involved mild reaction conditions with relatively safe reactants. Hydroxyl group is oxydised to aldehyde followed by reaction with ammonia in the presence of sodium cyanoborohydride.

We adapted the latest procedure to the preparation of amine derivative of Pluronic block copolymers. The advantage of these cationic derivatives in surface modification can be twofold. The introduction of primary amine groups provides the possibility of further coupling allowing e.g. the surface immobilization of targeting ligands on the NP surface. In addition to that the presence of positively charged molecules on a nanoparticle surface enhances their non-specific membrane affinity [23, 30]. It is however, an open question how these cationic derivatives change the physico-chemical properties of PLGA NPs compared to the systems stabilized with Pluronics. The synthesis of Pluronic-amines and their application in the preparation of surface modified PLGA NPs relevant as drug carriers is described in the present work. The nanoparticles were characterized by their size, surface charge and colloidal stability.

2. Experimental

2.1. Materials

Poly(ethylene oxide)/poly(propylene oxide)/poly (ethyleneoxide), PEO–PPO–PEO triblock copolymers, Pluronic F68 (M:8400), Pluronic F127 (M:12 600) and Pluronic F108 (M:14 600) (provided by BASF Hungaria Kft.), were applied as received. The composition of the polymers is characterized by the average length of the PPO chain (27, 56 and 44 monomeric units for F68, F127, and F108, respectively) and the length of the PEO chains (80, 101, and 141 monomeric units for F68, F127, and F108, respectively).

Poly(D,L-lactic-*co*-glycolic acid), PLGA with 50% of lactic and 50% of glycolic acid content (M:50 000–75 000) was obtained from Sigma-Aldrich. Acetic anhydride, ammonium chloride, potassium hydroxide and sodium cyanoborohydride used for the chemical modification of the Pluronics were purchased from Reanal Ltd. (Budapest, Hungary). Fluorescamine, hexylamine and pyrene used in the characterization of Pluronics were acquired from Sigma-Aldrich.

N-(tert-butoxycarbonyl)-L-phenylalanine,9-fluorenylmethoxycarbonyl-L-phenylalanine, isobutyl-chloroformate(Sigma-Aldrich Kft, Budapest, Hungary) and N-methylmorpholine (Fluka,Buchs, Switzerland) were used for conjugation. Sodium chloride (Riedel de Haën), calcium acetate (Reanal Ltd.) and all solvents were of analytical grade.

2.2. Preparation of Pluronic-amines

Primary amine terminated Pluronic derivatives were synthesized according to the method described by

Harris *et al*. [29] for the modification of polyethylene oxides. First 0.4 mmol Pluronic was dissolved in 15 mL freshly distilled DMSO. Following complete dissolution 3.7 mmol acetic anhydride was added and the reaction mixture was stirred for 30 h at room temperature. During this step the hydroxyl end groups of the Pluronic were oxidized into aldehyde form [31]. The reaction was stopped by precipitating the polymer in cold diethyl ether. After filtration the polymer was re-dissolved in dichloromethane then precipitated again in ether. The appearance of aldehyde groups was confirmed using Schiff reagent [32]. Pluronic sample was added to the reagent and the development of a rose color indicated the presence of aldehyde groups.

0.15 mmol Pluronic-aldehyde with 3 mmol ammonium-chloride, and 0.02 g potassium hydroxide was dissolved in 5 mL methanol. 3 mmol sodium cyanoborohydride in 5 mL methanol was added to this solution slowly over 30 min. Then 0.1 g potassium hydroxide was added to the reaction mixture which was stirred for 24 h at room temperature. The reaction was stopped by precipitating the product in cold ether. After filtration the polymer was dissolved in water and purified by dialysis against double distilled water. The purified product was acquired following the liophilization of the aqueous solution. The Pluronic-amines were prepared in three independent batches.

As a comparison the reactions were also carried out using water as a solvent instead of methanol.

2.2.1. Fluorescamine assay

The transformation of hydroxyl groups of Pluronic into amine groups was detected with the aid of the fluorescamine assay, which is a sensitive method for the surveying of primary amines [33–35]. Samples were prepared in 0.1 M borate buffer at pH 9 with a polymer concentration of 0.2 g/L. 150 μL fluorescamine solution in acetone with a concentration of 0.3 g/L was added to 3 mL of sample solution. The solution was vortexed for 10 s at 1000 rpm. Fluorescent spectra of the samples were recorded with a Varian Cary Eclipse fluorescence spectrophotometer (right-angle geometry, 1×1 cm^2 quartz cell). Monochromator slits were set to 5 nm and the excitation wavelength was 390 nm. Emission of the fluorescamine derivative of the Pluronic-amine was recorded at 486 nm. Degree of conversion of the end groups to amine was estimated from measurements using hexylamine as reference material. The measurements were carried out in triplicates.

2.2.2. NMR assay

All NMR spectra were obtained using a BRUKER AVANCE III 500 spectrometer operating at 500 131 MHz for the observation of ^1H nuclei in a 5 mm inverse probe. All spectra were recorded at 27 °C in deuterated chloroform as the lock solvent. To quantify the spectra a long repetition time of 8.3 s and 30° pulse angle were used. 4096 transients were accumulated in order to get excellent sensitivity.

2.2.3. Conjugation with amino acid

The N-(tert-butoxycarbonyl)-L-phenylalanine (Boc-Phe-OH) and 9-fluorenylmethoxycarbonyl-L-phenylalanine (Fmoc-Phe-OH) analogue of Pluronic F127-amine were synthesized manually using mixed anhydride method. The polymer was dissolved in ice cold dimethylformamide (~20 wt%) and 500 equiv of the N-terminus protected amino acid and 550 equiv isobutyl-chloroformate and 4-methylmorpholinein dimethylformamide were added. The mixture was stirred for 2 h at room temperature then left in refrigerator overnight at 4 °C. The resulting polymer-derivatives were purified by repeated dialysis against doubly distilled water (Slide-A-Lyzer G2 Dialysis Casette, MWCO: 10 kDa, ThermoScientic, USA).

2.2.4. Determination of critical micelle concentration

The critical micelle concentration (CMC) of Pluronics and Pluronic-amines was determined by fluorimetric method using pyrene as fluorescence probe. Pyrene is a hydrophobic fluorescence dye which shows different spectral pattern in micellar and non-micellar solution due its sensitivity to the polarity of the medium. 500 μL of pyrene solution in acetone with a concentration of 1.2 mM was added to 1 L of doubly distilled water and left overnight under stirring. A series of Pluronic solutions with increasing concentration were prepared using the filtered pyrene solution as medium. The concentration range was selected according to the CMC of the various Pluronics reported previously (Table 1) [36]. Samples were allowed to equilibrate for 1 h. The measurements were carried out with a Varian Cary Eclipse fluorescence spectrophotometer (right-angle geometry, 1×1 cm^2 quartz cell) at 25 and 37 °C. The exci-

Table 1. Critical micelle concentration of Pluronics and their amine derivatives

Sample	CMC* (25 °C) [g/L]	CMC (25 °C) [g/L]	CMC (37 °C) [g/L]
Pluronic F68	190	>100	>100
Pluronic F68-amine	–	>100	>100
Pluronic F127	1–7	3.3	0.09
Pluronic F127-amine	–	2.4	0.07
Pluronic F108	7– 45	33.4	2.0
Pluronic F108-amine	–	27.1	0.90

*from [36, 42, 43]

tation wavelength was 320 nm with a monochromator slit width of 5 nm while emission slit was set to 2 nm. Ratio of intensity of the first (I_1 at 373 nm) and third peaks (I_3 at 383 nm) is a sensitive parameter characterizing the polarity of the probe's environment. Strong emission at 383 nm with low I_1/I_3 value indicates low polarity of the environment. Hence I_1/I_3 is expected to decrease at the onset of the micelle formation, reflecting a preferential solubilization of pyrene into a less polar microenvironment [37, 38].

2.3. Preparation of Pluronic stabilized PLGA NPs

PLGA NPs were prepared in triplicates by the nanoprecipitation method similar to that employed previously [23, 39]. Briefly PLGA was dissolved in acetone at a concentration of 10 g/L. 6 mL of the organic solution was added to 24 mL aqueous solution of Pluronic or Pluronic-amine under magnetic stirring (500 rpm). Pluronic concentration in the aqueous phase was 2 g/L. NPs were formed and stirring was continued overnight to achieve the complete evaporation of acetone. The aqueous PLGA sol was centrifuged at 3500 g for 10 min to remove the possible polymer aggregates. The sol obtained as supernatant was further purified by centrifugation at 12 000 g for 15 min where the supernatant was removed and the pellet containing the NPs was re-dispersed in doubly distilled water. This procedure was repeated three times in order to remove the dissolved Pluronic from the aqueous medium.

2.3.1. Characterization of the size of NPs

Average hydrodynamic size and polydispersity of the PLGA NPs were determined using a dynamic light scattering (DLS) system (Brookhaven Instruments, USA) consisting of a BI-200SM goniometer and a BI-9000AT digital autocorrelator. As a light source a Coherent Genesis MX488-1000STM laser-diode system operating at 488 nm wavelength and emitting vertically polarized light was used. Measurements were carried out at a detection angle of 90° and a temperature of 25 °C with nanoparticle sample appropriately diluted with doubly distilled water. The recorded autocorrelation functions were analyzed by the second order cumulant expansion method.

2.3.2. Determination of zeta potential of NPs

The measurement of electrophoretic mobility of nanoparticles was carried out by means of Malvern Zetasizer Nano Z apparatus at 25 and 37 °C. Smoluchowski approximation was used to calculate zeta potential from mobility values. Particles were surveyed in aqueous salt solution with constant ionic strength (2 mM NaCl).

2.3.3. Characterization of colloidal stability of NPs

The effect of ionic strength on the colloidal stability of PLGA nanoparticles was investigated by adding salt solutions with increasing concentration to the sols. Sodium chloride and calcium acetate solutions were used as coagulation media. Experiments were carried out at 25 and 37 °C. Turbidity was measured with a spectrophotometer at a wavelength of 400 nm after incubation time of 15 min. The concentration of electrolyte which resulted in three times higher absorbance comparing to that of the original sol was used to estimate the critical aggregation concentrations (CAC). Higher CAC indicates the better colloidal stability of NP system. The electrolyte concentration was increased in 0.1 M steps during the experiments. No deviation was found in CAC during measurements of three separated batches.

3. Results and discussion

3.1. Preparation and characterization of Pluronic-amines

Amine end group derivatives of Pluronic F68, F127 and F108 were prepared via reductive amination of the partially oxidized hydroxyl end groups (Figure 1). Products were acquired with 60–80% yield following the two step reaction. The exact determination of the conversion of the end groups of Pluronics poses a significant challenge. Mass spectrometry could not be employed due to the similarity in the mass of the amine and hydroxyl groups. Classical analytical methods based on the determination of total nitrogen content were also not feasible because of the low

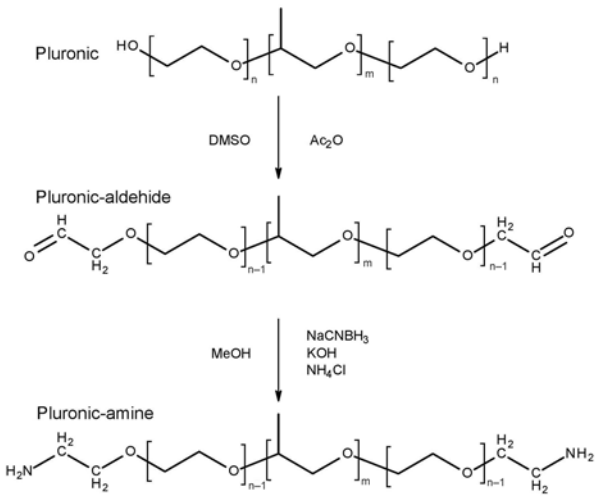

Figure 1. Two step conversion of Pluronics into Pluronic-amines

nitrogen content (appr. 0.1 wt%) of the polymeric compound.

Fluorescamine assay was employed as a selective and sensitive technique to obtain the amine content of the products. Fluorescamine, a nonfluorescent compound, reacts with primary amines to form pyrrolinones. Upon excitation at 390 nm these compounds exhibit strong fluorescence in the 450 to 550 nm range. Addition of fluorescamine to the products resulted in the formation of fluorescent species indicating the presence of primary amines. For the quantitative determination a calibration curve was recorded with hexylamine in the concentration range of 0–60 µmol/L while the Pluronic samples were measured at 0.2 g/L concentration (Figure 2). The fluorescent spectra of the fluorophores formed from the Pluronics and hexylamine had similar shape. Only a slight shift of around 3 nm was observed between the

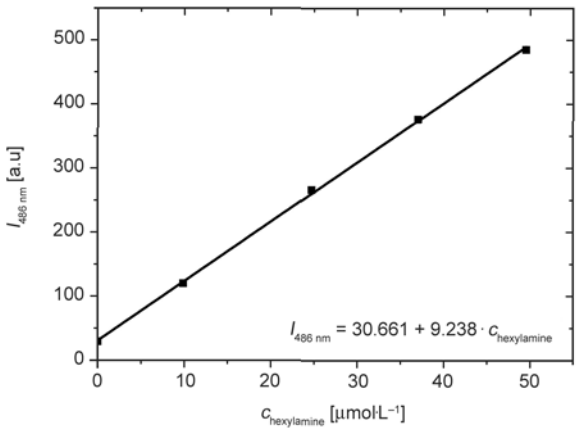

Figure 2. Fluorescence intensity calibration curve recorded with the hexylamine fluorophore

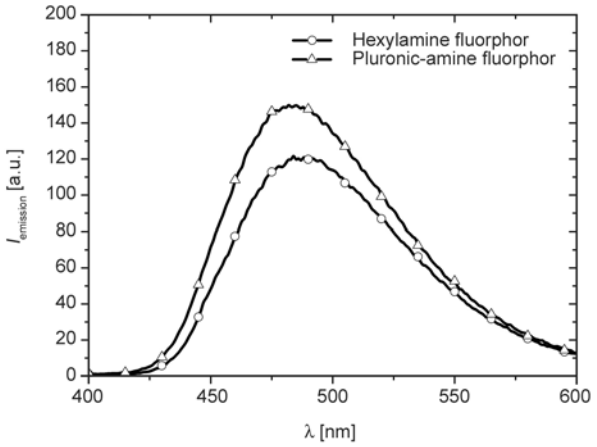

Figure 3. Fluorescent spectra of the hexylamine and Pluronic F127-amine fluorophores

intensity maxima of the two amine functional materials (Figure 3). The method proved to be robust enough for the determination of the amine content of the samples as measured intensities were within 5% error range for the triplicate measurements.

Taking into consideration the average molar masses and structure of the Pluronics the obtained end group amine conversions were 38, 41 and 22% for F68, F127 and F108 respectively with a standard deviation of 1–2%. The batch to batch reproducibility of conversion was also within 5% error. Since the chemical yield of the fluorophore is dependent to some extent on the structure of the amine [40] the acquired conversion values can be considered as approximates.

The transformation reaction to prepare amino-functional Pluronic was repeated in aqueous medium instead of methanol. Only 8 and 14% conversion was determined for F68 and F127 and practically none for F108. These findings indicate that the presence of water reduces the proceeding of the reaction.

The presence and reactivity of functional amino groups on Pluronic molecules were investigated by conjugation with Boc- or Fmoc-L-phenylalanine. The success of the conjugation reaction was checked by ninhydrine test and TLC. ^{1}H NMR spectra of the Boc-Phe and Fmoc-Phe-coupled Pluronic-amines clearly indicated the appearance of aromatic hydrogens in the range of 6.5–7.8 ppm. The ^{1}H NMR spectra of the Pluronic F127-amine and its Fmoc-Phe derivative is shown in Figure 4.

The strong singlet peak at 3.65 ppm belongs to the CH_2 groups of the PEO blocks. The two complex multiplets with 2:1 intensity ratio in the range of 3.3–3.6 ppm are the signals of –CH–CH_2– protons of

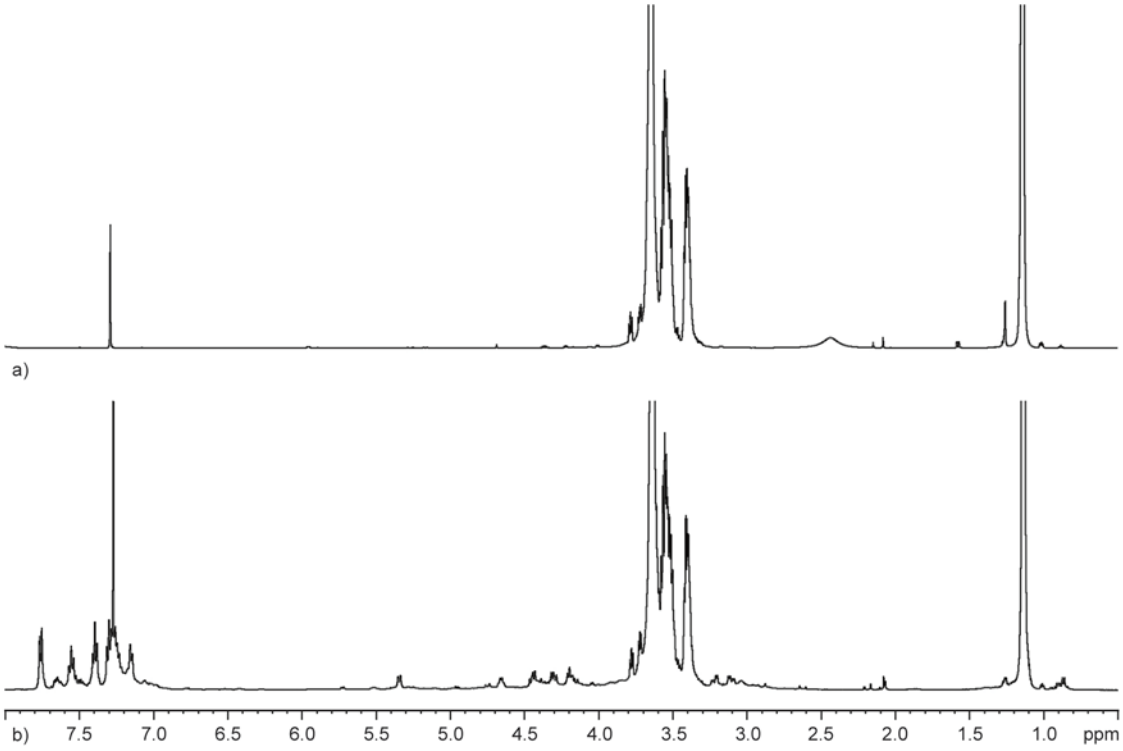

Figure 4. ^{1}H NMR spectra of the Pluronic F127-amine (a) and Pluronic F127-Phe-Fmoc (b)

the PPO block while the peak at 1.14 ppm belongs to PPO methyl groups. The amine derived Pluronic F127 exhibits a broad signal at 2.434 ppm, which indicates the presence of terminal amine groups.

Pluronic F127-Phe-Fmoc shows very similar signals to the amine derived F127 in the spectrum ranges given above. The major difference is the vanishing amine signal at 2.434 ppm and the new aromatic protons in the range of 7–8 ppm. There are new weak proton signals in the 4.0–5.5 ppm and 2.5–3.3 ppm regions which belong to the aliphatic protons of the terminal Phe-Fmoc groups.

The aromatic region contains the multiplets of the ABCD spin systems of the two terminal fluorenyl groups and a strongly overlapping signal of the AA′BB′C system of the phenyl groups. The well separated doublet at 7.763 ppm belongs to the overlapping aromatic protons in positions 4 and 5 of the fluorenyl group.

As amphiphatic block copolymers Pluronics self-associate in aqueous solution forming micellar type aggregates. The concentration range where this association becomes dominant is a characteristic parameter depending on the composition of the molecule and environmental conditions as well. The critical micelle concentration (CMC) of Pluronic F68, F127 and F108 and their amine derivatives were determined in aqueous solution at two temperatures using the pyrene fluorescent probe method. Increasing the concentration of Pluronics a large decrease begins in the I_1/I_3 values after a given point indicating the appearance of hydrophobic domains due to the formation of micelles (Figure 5). At the end of this transition concentration range the solubilization of pyrene reaches the saturation which is represented by steady low value of I_1/I_3.

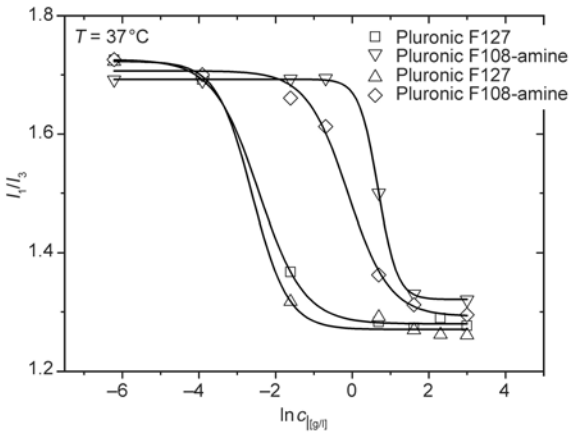

Figure 5. Pyrene I_1/I_3 values as a function of Pluronic concentration at 37 °C

To resolve a definite concentration value of CMC the measured points were fitted with a decreasing Boltzmann type sigmoid, which is given by Equation (1):

$$y = \frac{A_1 - A_2}{1 + e^{(x - x_0)/\Delta x}} + A_2 \quad (1)$$

where the variable y corresponds to the I_1/I_3 values, while x is the total Pluronic concentration. A_1 and A_2 are the upper and lower limiting values, x_0 is the centre of the sigmoid and Δx is the width of the sigmoid. According to Aguiar *et al*. [41] the CMC should be given as x_0 if the ratio $x_0/\Delta_x < 10$ and as $(x_0 + 2\Delta x)$ otherwise. Since the $x_0/\Delta_x < 10$ condition was valid in all of our cases x_0 was selected as CMC. The determined CMC values are shown in Table 1.

CMC values obtained for Pluronics F127 and F108 at 25 °C are in accordance with the results of other studies being within the range reported previously [36, 42, 43]. That is valid for Pluronic F68 too, which did not show association in the investigated concentration range up to 100 g/L.

Considering the Pluronic-amines the CMC of the amine derivatives were found to be in the same concentration range as the corresponding starting material signifying that the present chemical modification of the end groups does not change the association behavior of the Pluronics. Comparing the shapes of I_1/I_3 vs concentration curves for the Pluronics and their amine derivatives however some differences can be observed (Figure 5). The transition of the pyrene probe from a hydrophilic to a hydrophobic environment occurs over a relatively wide concentration range especially for the amine derivatives which could be related to the dispersity of the polymer. This makes the determination of the CMC defined as the centre of the fitted sigmoid somewhat ambiguous. That might be the explanation for the shift of CMC values given in Table 1.

As it is characteristic for PEO-containing surfactants in general a decrease in the micellization concentration was observed at higher temperature. The decrease of CMC is about one order of magnitude in the 25–37 °C temperature range studied here.

3.2. Preparation and characterization Pluronic stabilized nanoparticles

Pluronic and Pluronic-amine stabilized PLGA nanoparticles were prepared by nanoprecipitation. The NPs obtained applying Pluronic F127 and Pluronic F108 as well as their amine derivatives were characterized by dynamic light scattering and zeta potential measurements. The average hydrodynamic diameter (d), polydispersity (PD) and zeta potential (ζ) of the particles are collected in Table 2.

Table 2. Average hydrodynamic diameter (d), polydispersity (PD) and zeta potential (ζ) of PLGA NPs*

Stabilizer	d [nm]	PD	ζ [mV]	
			25 °C	37 °C
Pluronic F127	114	0.05	–11.3	–11.9
Pluronic F127-amine	116	0.08	–6.5	–5.7
Pluronic F108	115	0.06	–14.2	–13.4
Pluronic F108-amine	118	0.06	–10.2	–10.9

*Data were reproducible within 5% error between batches

Mean diameter of the particles was around 115 nm regardless of the stabilizer used. All samples showed a narrow size distribution with PD values below 0.1. The particles had a negative zeta potential due to the carboxylic end groups of the PLGA chains located on the particle surface and partly covered by Pluronic layer. The usage of Pluronic-amine decreased the potential which was valid for both Pluronics and at both temperatures investigated. That decrease in zeta potential is clearly due to the presence of protonated amine groups of Pluronic-amine.

Bare PLGA particles are stabilized in aqueous solution by electrostatic interactions due to their negative surface charge [44]. The stability of such systems vanishes above a certain electrolyte concentration due to the screening effect of ionic strength. Aggregation in these systems happens at as low NaCl concentration as 0.03 M [23]. The role of Pluronic stabilizer however, is to give steric stability of NPs, making the colloidal system less sensitive to the variation of electrolyte concentration in the medium.

Colloidal stability of the Pluronic stabilized PLGA NPs was tested by measuring the turbidity of sols at different electrolyte concentrations in their aqueous media. The determined CAC values are listed in Table 3.

Table 3. Critical aggregation concentration (CAC) of PLGA NP systems stabilized by Pluronics and Pluronic-amines checked by NaCl and Ca-acetate at 25 and 37 °C

Stabilizer	CAC [M]		CAC [M]	
	NaCl electrolyte		Ca-acetate electrolyte	
	25 °C	37 °C	25 °C	37 °C
Pluronic F127	>2.5	>2.5	>1	0.9
Pluronic F127-amine	>2.5	>2.5	>1	1
Pluronic F108	2.0	1.8	0.6	0.6
Pluronic F108-amine	2.3	1.8	0.6	0.6

All samples showed a highly increased colloidal stability compared to the pure PLGA NP system. This is due to the steric stabilization by the Pluronic adsorption layer on the NP surface. Particles stabilized by Pluronic F127 and its amine derivative retained their stability at all concentrations that were tested, with NaCl up till 2.5 M regardless of temperature. The particles stabilized with Pluronic F108 and F108-amine showed a slightly reduced but still remarkably high CAC values. These systems aggregated only around 2 M NaCl. Destabilization occurred earlier at 37 °C due to the fact that the hydrophobic interactions become more prominent between PEO chains with increasing temperature leading to a decrease in the hydration of the Pluronic adsorption layer [45, 46]. Ca-acetate was also used as electrolyte to test the effect of divalent ions on the colloidal stability of the NPs. Due to its lower solubility the concentrations up till 1.0 M were tested. NP systems stabilized by Pluronic F127 were stable, but aggregation occurred in systems where Pluronic F108 was applied. The slightly less stability obtained for all NP systems with Pluronic F108 or Pluronic F108-amine comparing to the corresponding Pluronic F127 samples is probably due to the difference in chemical composition, the block ratio and hence in the structure of adsorption layers. It is important to note, however that practically no difference was observed in the stabilization potential of Pluronics and their amine derivatives, both forms were effective.

4. Conclusions

End group derivative of various Pluronics were synthesized in a simple chemical procedure to obtain Pluronic-amine. The formation of the product was confirmed by the fluorescamine method and NMR analysis of the Boc-Phe-OH and Fmoc-Phe-OH coupled derivatives.

As verified by the CMC measurements the chemical modification did not alter significantly the polarity and association property of the molecules in aqueous environment.

The Pluronic-amines were applied as steric stabilizers for PLGA NPs prepared by the nanoprecipitation technique. The particles formed were in the 110–120 nm range making them ideal for drug delivery applications. No significant changes were observed in the size of the particles when the original Pluronics and their amine derivatives were applied. The presence of the positively charged end groups were however detectable in electrophoretic mobility measurements by a shift in the zeta potential. The colloidal stability of the PLGA NPs was sufficiently high at 25 and 37 °C making them suitable for use in biological environments with high ionic strengths.

The possibility for further chemical modifications of the Pluronic-amines was also demonstrated through the chemical binding of Boc-Phe-OH and Fmoc-Phe-OH to the amine terminal. Such type of modifications open the way for convenient conjugation with e.g. host cell specific peptides as selective targeting moieties making achievable efficient drug delivery.

Direct experimental data support the conclusion that the membrane affinity of Pluronic derivatives (i.e. Pluronic-polyamine) was improved when compared to that of Pluronic [27, 47]. Based on these data we may assume that this feature will be present when Pluronic-amines are on the surface of PLGA NPs. Therefore we may expect that NPs containing Pluronic-amine surface layer show higher cellular uptake rate. This assumption was supported by our experimental data on drug loaded PLGA NPs [48]. When the carriers were functionalized by Pluronic F127 and Pluronic-F127-amine highly increased in vitro efficiency was achieved for an antituberculotic drug candidate. The reason was shown to be the ability for the particles to enter the host cells of the bacteria. When the Pluronic-amine derivative was used for the stabilization of the particles increased internalization and intracellular antibacterial effect was obtained. The presence of cationic charges on the particle surface was shown to increase the non-specific cell membrane affinity of the particles leading to increased cellular uptake rate [48].

Acknowledgements

This work was supported by the National Science Foundation: OTKA 104928, 104275, OTKA NK 105898 and TÁMOP 4.2.4. A/2-11-1-2012-0001 ‘National Excellence Program’.

References

[1] Ganguly K., Chaturvedi K., More U. A., Nadagouda M. N., Aminabhavi T. M.: Polysaccharide-based micro/nanohydrogels for delivering macromolecular therapeutics. Journal of Controlled Release, **193**, 162–173 (2014).
DOI: 10.1016/j.jconrel.2014.05.014

[2] Mohanraj V. J., Chen Y.: Nanoparticles – A review. Tropical Journal of Pharmaceutical Research, **5**, 561–573 (2006).
DOI: 10.4314/tjpr.v5i1.14634

[3] Soppimath K. S., Aminabhavi T. M., Kulkarni A. R., Rudzinski W. E.: Biodegradable polymeric nanoparticles as drug delivery devices. Journal of Controlled Release, **70**, 1–20 (2001).
DOI: 10.1016/S0168-3659(00)00339-4

[4] Mu L., Seow P. H.: Application of TPGS in polymeric nanoparticulate drug delivery system. Colloids and Surfaces B: Biointerfaces, **47**, 90–97 (2006).
DOI: 10.1016/j.colsurfb.2005.08.016

[5] Karger-Kocsis J., Kéki S.: Biodegradable polyester-based shape memory polymers: Concepts of (supra) molecular architecturing. Express Polymer Letters, **8**, 397–412 (2014).
DOI: 10.3144/expresspolymlett.2014.44

[6] Mundargi R. C., Babu V. R., Rangaswamy V., Patel P., Aminabhavi T. M.: Nano/micro technologies for delivering macromolecular therapeutics using poly(D,L-lactide-*co*-glycolide) and its derivatives. Journal of Controlled Release, **125**, 193–209 (2008).
DOI: 10.1016/j.jconrel.2007.09.013

[7] Fessi H., Puisieux F., Devissaguet J. P., Ammoury N., Benita S.: Nanocapsule formation by interfacial polymer deposition following solvent displacement. International Journal of Pharmaceutics, **55**, R1–R4 (1989).
DOI: 10.1016/0378-5173(89)90281-0

[8] Pitt C. G., Gratzl M. M., Kimmel G. L., Surles J., Schindler A.: Aliphatic polyesters II. The degradation of poly (DL-lactide), poly (epsilon-caprolactone), and their copolymers *in vivo*. Biomaterials, **2**, 215–220 (1981).

[9] Li S. M., Garreau H., Vert M.: Structure-property relationships in the case of the degradation of massive poly(α-hydroxy acids) in aqueous media, Part 3 Influence of the morphology of poly(L-lactic acid). Journal of Materials Science: Materials in Medicine, **1**, 198–206 (1990).
DOI: 10.1007/BF00701077

[10] Pistner H., Bendi D. R., Mühling J., Reuther J. F.: Poly (L-lactide): A long-term degradation study *in vivo*: Part III. Analytical characterization. Biomaterials, **14**, 291–298 (1993).
DOI: 10.1016/0142-9612(93)90121-H

[11] Czifrák K., Karger-Kocsis J., Daróczi L., Zsuga M., Kéki S.: Poly(ε-caprolactone) and Pluronic diol-containing segmented polyurethanes for shape memory performance. Macromolecular Chemistry and Physics, **215**, 1896–1907 (2014).
DOI: 10.1002/macp.201400237

[12] Storm G., Belliot S. O., Daemen T., Lasic D. D.: Surface modification of nanoparticles to oppose uptake by the mononuclear phagocyte system. Advanced Drug Delivery Reviews, **17**, 31–48 (1995).
DOI: 10.1016/0169-409X(95)00039-A

[13] Moghimi S. M.: Re-establishing the long circulatory behaviour of poloxamine-coated particles after repeated intravenous administration: Applications in cancer drug delivery and imaging. Biochimica et Biophysica Acta – General Subjects, **1472**, 399–403 (1999).
DOI: 10.1016/S0304-4165(99)00157-9

[14] Gyulai G., Pénzes Cs. B., Mohai M., Lohner T., Petrik P., Kurunczi S., Kiss É.: Interfacial properties of hydrophilized poly(lactic-*co*-glycolic acid) layers with various thicknesses. Journal of Colloid and Interface Science, **362**, 600–606 (2011).
DOI: 10.1016/j.jcis.2011.06.055

[15] Kiss É., Gölander C-G.: Static and dynamic wetting behavior of poly(ethylene oxide) layer formed on mica substrate. Colloids and Surfaces, **58**, 263–270 (1991).
DOI: 10.1016/0166-6622(91)80226-E

[16] Kiss É., Dravetzky K., Hill K., Kutnyánszky E., Varga A.: Protein interaction with a Pluronic-modified poly (lactic acid) Langmuir monolayer. Journal of Colloid and Interface Science, **325**, 337–345 (2008).
DOI: 10.1016/j.jcis.2008.05.057

[17] Kiss É., Kutnyánszky E., Bertóti I.: Modification of poly(lactic/glycolic acid) surface by chemical attachment of poly(ethylene glycol). Langmuir, **26**, 1440–1444 (2010).
DOI: 10.1021/la903373g

[18] Cheng J., Teply B. A., Sherifi I., Sung J., Luther G., Gu F. X., Levy-Nissenbaum E., Radovic-Moreno A. F., Langer R., Farokhzad O. C.: Formulation of functionalized PLGA–PEG nanoparticles for *in vivo* targeted drug delivery. Biomaterials, **28**, 869–876 (2007).
DOI: 10.1016/j.biomaterials.2006.09.047

[19] Moghimi S. M.: Prolonging the circulation time and modifying the body distribution of intravenously injected polystyrene nanospheres by prior intravenous administration of poloxamine-908. A 'hepatic-blockade' event or manipulation of nanosphere surface *in vivo*? Biochimica et Biophysica Acta – General Subjects, **1336**, 1–6 (1997).
DOI: 10.1016/S0304-4165(97)00060-3

[20] Redhead H. M., Davis S. S., Illum L.: Drug delivery in poly(lactide-*co*-glycolide) nanoparticles surface modified with poloxamer 407 and poloxamine 908: *In vitro* characterisation and *in vivo* evaluation. Journal of Controlled Release, **70**, 353–363 (2001).
DOI: 10.1016/S0168-3659(00)00367-9

[21] Kiss É., Varga A., Vargha-Butler É. I.: Interfacial behaviour of poly(lactic acid) and Pluronic6400 mixed monolayers at the air–water interface. Physical Chemistry Chemical Physics, **6**, 1575–1579 (2004).
DOI: 10.1039/B312950K

[22] Kiss É., Takács M. G., Bertóti I., Vargha-Butler E. I.: Surface properties of poly(lactic/glycolic acid)–Pluronic® blend films. Polymers for Advanced Technologies, **14**, 839–846 (2003).
DOI: 10.1002/pat.404

[23] Gyulai G., Pénzes Cs. B., Mohai M., Csempesz F., Kiss É.: Influence of surface properties of polymeric nanoparticles on their membrane affinity. European Polymer Journal, **49**, 2495–2503 (2013).
DOI: 10.1016/j.eurpolymj.2013.02.024

[24] Neal J. C., Stolnik S., Garnett M. C., Davis S. S., Illum L.: Modification of the copolymers Poloxamer 407 and Poloxamine 908 can affect the physical and biological properties of surface modified nanospheres. Pharmaceutical Research, **15**, 318–324 (1998).
DOI: 10.1023/A:1011987206722

[25] Yaniç C., Bredenkamp M. W., Jacobs E. P., Spies H. S. C., Swart P.: NMR spectroscopy as basis for characterization of Pluronic® F108 and its derivatives. Journal of Applied Polymer Science, **78**, 109–117 (2000).
DOI: 10.1002/1097-4628(20001003)78:1<109::AID-APP140>3.0.CO;2-6

[26] Vinogradov S. V., Bronich T. K., Kabanov A. V.: Self-assembly of polyamine–poly(ethylene glycol) copolymers with phosphorothioate oligonucleotides. Bioconjugate Chemistry, **9**, 805–812 (1998).
DOI: 10.1021/bc980048q

[27] Yi X., Batrakova E., Banks W. A., Vinogradov S., Kabanov A. V.: Protein conjugation with amphiphilic block copolymers for enhanced cellular delivery. Bioconjugate Chemistry, **19**, 1071–1077 (2008).
DOI: 10.1021/bc700443k

[28] Zalipsky S.: Functionalized poly(ethylene glycols) for preparation of biologically relevant conjugates. Bioconjugate Chemistry, **6**, 150–165 (1995).
DOI: 10.1021/bc00032a002

[29] Harris J. M., Struck E. C., Case M. G., Paley M. S., Yalpani M., Van Alstine J. M., Brooks D. E.: Synthesis and characterization of poly(ethylene glycol) derivatives. Journal of Polymer Science: Polymer Chemistry Edition, **22**, 341–352 (1984).
DOI: 10.1002/pol.1984.170220207

[30] Tatur S., Maccarini M., Barker R., Nelson A., Fragneto G.: Effect of functionalized gold nanoparticles on floating lipid bilayers. Langmuir, **29**, 6606–6614 (2013).
DOI: 10.1021/la401074y

[31] Kiss É., Bertóti I.: Preparation and characterization of PEO grafted surfaces by wettability measurements. Progress in Colloid and Polymer Science, **97**, 21–26 (1994).
DOI: 10.1007/BFb0115129

[32] Lillie R. D.: Simplification of the manufacture of schiff reagent for use in histochemical procedures. Biotechnic and Histochemistry, **26**, 163–165 (1951).
DOI: 10.3109/10520295109113200

[33] Böhlen P., Stein S., Dairman W., Udenfriend S.: Fluorometric assay of proteins in the nanogram range. Archives of Biochemistry and Biophysics, **155**, 213–220 (1973).
DOI: 10.1016/S0003-9861(73)80023-2

[34] Belal F., Abdine H., Al-Majed A., Khalil N. Y.: Spectrofluorimetric determination of vigabatrin and gabapentin in urine and dosage forms through derivatization with fluorescamine. Journal of Pharmaceutical and Biomedical Analysis, **27**, 253–260 (2002).
DOI: 10.1016/S0731-7085(01)00503-9

[35] Adamou R., Coly A., Douabalé S. E., Saleck M. L. O. C. O., Gaye-Seye M. D., Tine A.: Fluorimetric determination of histamine in fish using micellar media and fluorescamine as labelling reagent. Journal of Fluorescence, **15**, 679–688 (2005).
DOI: 10.1007/s10895-005-2975-7

[36] Alexandridis P., Holzwarth J. F., Hatton T. A.: Micellization of poly(ethylene oxide)-poly(propylene oxide)-poly(ethylene oxide) triblock copolymers in aqueous solutions: Thermodynamics of copolymer association. Macromolecules, **27**, 2414–2425 (1994).
DOI: 10.1021/ma00087a009

[37] Goddard E. D., Turro N. J., Kuo P. L., Ananthapadmanabhan K. P.: Fluorescence probes for critical micelle concentration determination. Langmuir, **1**, 352–355 (1985).
DOI: 10.1021/la00063a015

[38] Wang Y., Zhang M., Moers C., Chen S., Xu H., Wang Z., Zhang X., Li Z.: Block copolymer aggregates with photo-responsive switches: Towards a controllable supramolecular container. Polymer, **50**, 4821–4828 (2009).
DOI: 10.1016/j.polymer.2009.08.005

[39] Kiss É., Schnöller D., Pribranská K., Hill K., Pénzes Cs. B., Horváti K., Bősze S.: Nanoencapsulation of antitubercular drug isoniazid and its lipopeptide conjugate. Journal of Dispersion Science and Technology, **32**, 1728–1734 (2011).
DOI: 10.1080/01932691.2011.616128

[40] de Bernardo S., Weigele M., Toome V., Manhart K., Leimgruber W. B. P., Böhlen P., Stein S., Udenfriend S.: Studies on the reaction of fluorescamine with primary amines. Archives of Biochemistry and Biophysics, **163**, 390–399 (1974).
DOI: 10.1016/0003-9861(74)90490-1

[41] Aguiar J., Carpena P., Molina-Bolívar J. A., Carnero Ruiz C.: On the determination of the critical micelle concentration by the pyrene 1:3 ratio method. Journal of Colloid and Interface Science, **258**, 116–122 (2003).
DOI: 10.1016/S0021-9797(02)00082-6

[42] Chu B., Zhou Z.: Physical chemistry of polyoxyalkylene block copolymer surfactants. in 'Nonionic surfactants: Polyoxyalkylene block copolymers' (ed.: Nace V. M.) Marcel Dekker, New York 78–80 (1996).

[43] Lopes J. R., Loh W.: Investigation of self-assembly and micelle polarity for a wide range of ethylene oxide–propylene oxide–ethylene oxide block copolymers in water. Langmuir, **14**, 750–756 (1998).
DOI: 10.1021/la9709655

[44] Santander-Ortega M. J., Jódar-Reyes A. B., Csaba N., Bastos-González D., Ortega-Vinuesa J. L.: Colloidal stability of Pluronic F68-coated PLGA nanoparticles: A variety of stabilisation mechanisms. Journal of Colloid and Interface Science, **302**, 522–529 (2006). DOI: 10.1016/j.jcis.2006.07.031

[45] Claesson P. M., Kjellander R., Stenius P., Christenson H. K.: Direct measurement of temperature-dependent interactions between non-ionic surfactant layers. Journal of the Chemical Society, Faraday Transactions 1: Physical Chemistry in Condensed Phases, **82**, 2735–2746 (1986). DOI: 10.1039/F19868202735

[46] Kiss É.: Temperature dependence of bovine serum albumin adsorption onto a poly(ethylene oxide)-grafted surface. Colloids and Surfaces A: Physicochemical and Engineering Aspects, **76**, 135–140 (1993). DOI: 10.1016/0927-7757(93)80071-L

[47] Fan W., Wu X., Ding B., Gao J., Cai Z., Zhang W., Yin D., Wang X., Zhu Q., Liu J., Ding X., Gao S.: Degradable gene delivery systems based on Pluronics-modified low-molecular-weight polyethylenimine: Preparation, characterization, intracellular trafficking, and cellular distribution. International Journal of Nanomedicine, **7**, 1127–1138 (2012). DOI: 10.2147/IJN.S27117

[48] Kiss É., Gyulai G., Pénzes Cs. B., Idei M., Horváti K., Bacsa B., Bősze S.: Tuneable surface modification of PLGA nanoparticles carrying new antitubercular drug candidate. Colloids and Surfaces A: Physicochemical and Engineering Aspects, **458**, 178–186 (2014). DOI: 10.1016/j.colsurfa.2014.05.048

eXPRESS Polymer Letters Vol.10, No.3 (2016) 227–236
Available online at www.expresspolymlett.com
DOI: 10.3144/expresspolymlett.2016.21

Barium ferrite/epoxy resin nanocomposite system: Fabrication, dielectric, magnetic and hydration studies

A. Kanapitsas[1], *C. Tsonos*[1], *G. C. Psarras*[2*], *S. Kripotou*[3]

[1]Electronics Engineering Department, Technological Educational Institute of Sterea Ellada, 35100 Lamia, Greece
[2]Department of Materials Science, School of Natural Sciences, University of Patras, 26504 Patras, Greece
[3]Department of Physics, School of Applied Mathematical and Physical Sciences, National Technical University of Athens, Zografou 15780, Athens, Greece

Received 23 July 2015; accepted in revised form 5 October 2015

Abstract. Composite systems of epoxy resin and barium ferrite nanoparticles have been prepared, and studied varying the content of the inclusions. Morphology of prepared samples has been examined via scanning electron microscopy and X-ray diffraction spectra, while electrical and magnetic properties were investigated by means of broadband dielectric spectroscopy, and magnetization tests respectively. Finally, water vapor sorption measurements were conducted in order to study the water sorption dynamics of the system. Electron microscopy images revealed the successful fabrication of nanocomposites. Dielectric permittivity increases with filler content, while three relaxation processes were detected in the relative spectra. These processes are attributed to interfacial polarization, glass to rubber transition of the matrix, and re-orientation of polar side groups of the polymer's chain. Magnetization and magnetic saturation increase with magnetic nano-powder content. Nanocomposites absorb a small amount of water, not exceeding 1.7 wt%, regardless filler content, indicating their hydrophobic character.

Keywords: *nanocomposites, barium ferrite, dielectric properties, magnetic properties, hydration*

1. Introduction

M-type barium ferrite with hexagonal structure ($BaFe_{12}O_{19}$) is a well-known high-performance permanent magnetic material, owing to its high magnetocrystalline anisotropy, high Curie temperature, relatively large magnetization, excellent chemical stability and corrosion resistance. M-type hexaferrites have continuously made inroads in applications such as plastoferrites, injection-molded pieces, microwave devices, and magnetic recording media. With proper design and substitutions, passive elements including mm-wave circulators can be constructed from hexaferrites. Ba-hexaferrites with composition of $BaFe_{12}O_{19}$, are the most widely used among the various hexaferrite compounds. The most significant property is the very high magnetocrystalline anisotropy field (1.7 T), which results in a high coercivity, remanence and a ferromagnetic resonance at around 50 GHz, [1]. Recently increased attention is given to ferrites, ferrite based complex ceramics, and to magnetic semiconductors [2–8]. The majority of these works refers to the variation of magnetic permeability, dielectric permittivity at GHz, and absorption properties, with the composition and the preparation procedure of ceramic compounds. On the other hand studies concerning the magnetic behaviour of polymer based composites are still scarce [9–13].

Polymers exhibit a number of advantages, which include ease processing and forming, thermomechanical stability, high dielectric breakdown strength and low cost. Conductivity, dielectric and magnetic

*Corresponding author, e-mail: G.C.Psarras@upatras.gr

properties of polymers can be substantially altered by embedding suitable reinforcing inclusions. Dielectric and magnetic response can be tuned by controlling the amount and the type of the employed ceramic inclusions [14–17]. Epoxy resins are extensively used for the production of high tech composites in the fields of automotive, aerospace and electronic industries, mostly due to their high stiffness and good adhesion with the inclusions [18–21]. However, a possible drawback in micro or nano epoxy composites' performance could be related to the effect of environmental attack and the resulting degradation. Water uptake due to the exposure in humid environments is a major factor influencing performance and service life of composites.

In this work nanocomposites constituted of an epoxy resin matrix and barium ferrite nanoparticles as the reinforcing phase, have been prepared and studied, at various filler content. It is a first attempt to fabricate a single-filler nanocomposite system with tunable magneto-electric response, suitable for outdoors applications. Specimens' morphology was assessed via scanning electron microscopy (SEM) and X-ray diffraction (XRD) spectra, while dielectric and magnetic response were studied by means of broadband dielectric spectroscopy (BDS) and magnetization measurements, respectively. Finally, hydration studies were performed by water vapor sorption measurements.

2. Experimental

2.1. Materials and nanocomposites manufacturing

Nanocomposite specimens were prepared by employing commercially available materials. In particular a low viscosity epoxy resin (ER) (Epoxol 2004A) was used as a prepolymer, while Epoxol 2004B (operating at a slow rate) was used as curing agent. Both reactants were supplied by Neotex S.A., Athens, Greece. Barium ferrite (BaFe) particles were purchased by Sigma-Aldrich. The mean particle diameter was less than 100 nm. The preparation procedure involved mixing of the resin with the curing agent in a 2:1 (w/w) ratio and then adding, while the polymer system was still in the liquid state, various amounts of the filler. Stirring at a low rate, degassing the mixtures in a vacuum-oven, and ultrasonication were also included in the preparation procedure [21, 22]. The content of barium ferrite in the produced specimens was 0, 3, 10, 20, 30, and 50 parts per hundred resin [phr]. Filler's content and respective volume fractions are listed in Table 1. The initial curing took place at ambient for a week, followed by post-curing at 100 °C for 4 hours. The specimens' morphology, as well as, the achieved quality of the filler dispersion within the polymer matrix was examined via Scanning Electron Microscopy (SEM) (EVO MA 10, ZEISS). X-ray diffraction analyses were made by Siemens diffractometer model Z500, by using Cu-Ka (λ = 1.54056 Å, 40 kV, 30 mA) in wide range of Braggs angles 20–90°.

2.2. Dielectric and magnetic measurements

Dielectric measurements were conducted by means of broadband dielectric spectroscopy (BDS) using an Alpha-N Frequency Response Analyser, supplied by Novocontrol Technologies (Hundsagen, Germany). The applied Vrms was kept constant at 1000 mV, while field's frequency was varied between 10^{-1} to 10^{6} Hz. Isothermal scans were carried out in the temperature range from ambient to 150 °C, in steps of 5 °C. Temperature was controlled via the Novotherm system within ±0.1 °C (Novocontrol Technologies). The employed dielectric test cell was the BDS-1200, parallel-plate capacitor with two gold-plated electrodes system, supplied also by

Table 1 Barium ferrite content in phr and volume fraction in the examined specimens, magnetic saturation and remanence magnetization of nanocompsoites and neat barium ferrite

Specimen	Volume fraction [%]	Magnetic saturation: M_s [emu/g]	Remanence magnetization [emu/gr]
Epoxy resin	0	–	–
Epoxy resin + 3 phr $BaFe_{12}O_{19}$	0.60	0.25	0.08
Epoxy resin + 10 phr $BaFe_{12}O_{19}$	1.98	0.50	0.15
Epoxy resin + 20 phr $BaFe_{12}O_{19}$	3.79	1.59	0.50
Epoxy resin + 30 phr $BaFe_{12}O_{19}$	5.69	1.85	0.56
Epoxy resin + 50 phr $BaFe_{12}O_{19}$	8.80	3.16	0.95
$BaFe_{12}O_{19}$	100	14.00	4.09

Novocontrol Technologies. The dielectric cell was electrically shielded and data acquisition was fully automated and conducted via suitable software.

The magnetization measurements were performed using a Quantum Design superconducting quantum interference device (SQUID), with maximum field at 5 Tesla. The hysteresis loops were measured up to 5 T. The zero-field-cooled (ZFC) and field cooled (FC) processes were recorded at low magnetic fields in temperature range from 5 to 300 K (–268.2 to 26.8 °C). Before each run, samples were demagnetized at 300 K (26.8 °C) by applying an oscillatory magnetic field, and then cooled down in zero fields to 5 K (–268.2 °C). At 5 K (–268.2 °C), a small magnetic field of the order of 100 or 1000 Oe in the powder was applied, and the magnetization was measured as we heated the sample to 300 K (26.8 °C). This procedure was denoted as the ZFC measurement. At 300 K, the small-applied magnetic field was kept as it is and then samples were cooled again to 2 K (–271.2 °C), with a subsequent recording of the magnetization as we heated the sample to 300 K (26.8 °C). Such measurement was denoted as FC measurement.

2.3. Hydration studies

Water vapor sorption measurements were performed using VTI SA+ vapor sorption analyzer supplied by TA Instruments. The sample mass was continuously recorded as a function of time, until equilibrium was reached, at different levels of relative humidity between 10 and 95% both while increasing (sorption) and decreasing (desorption). All the measurements were done at a constant temperature of 25°C.

3. Results and discussion

Figure 1 depicts representative SEM images of the fracture surface of the nanocomposites with 3 (Figure 1a) and 5 phr (Figure 1b) in barium ferrite content. In all examined cases nanodispersions were detected in tandem with small clusters, denoting the successful manufacturing of the $BaFe_{12}O_{19}$/epoxy resin nanocomposites. In the literature there are many studies [23–27], especially for $BaTiO_3$ reinforced polymer nanocomposites, where surface modifications of filler's particles result in better distribution of nanoinclusions. Although, this is the general trend and surface modification is considered as beneficial to both nanodispersions and physical properties, filler's modification should not be considered as a panacea. Surface modification could add a type of coating to nanoinclusions with different electrical properties, being detrimental sometimes to the desired electrical behaviour of the nanocomposites [24, 28, 29].

XRD spectra of barium ferrite nanopowder and the nanocomposite with 3 phr magnetic powder are shown in Figure 2a and 2b, respectively. XRD data revealed the presence of Fe_2O_3 within the magnetic powder. Moreover, grain diameters calculated using the Sherrer formula of 28 nm for $BaFe_{12}O_{19}$ and 26 nm for Fe_2O_3, were found. An analogous picture is obtained for the 3 phr $BaFe_{12}O_{19}$/epoxy resin nanocomposite.

Dielectric spectra of the ER/20 phr $BaFe_{12}O_{19}$ are shown in the 3D graphs of Figure 3. Variation of the real part of dielectric permittivity (ε') as a function of frequency and temperature is presented in Figure 3a. Permittivity increases with diminishing of

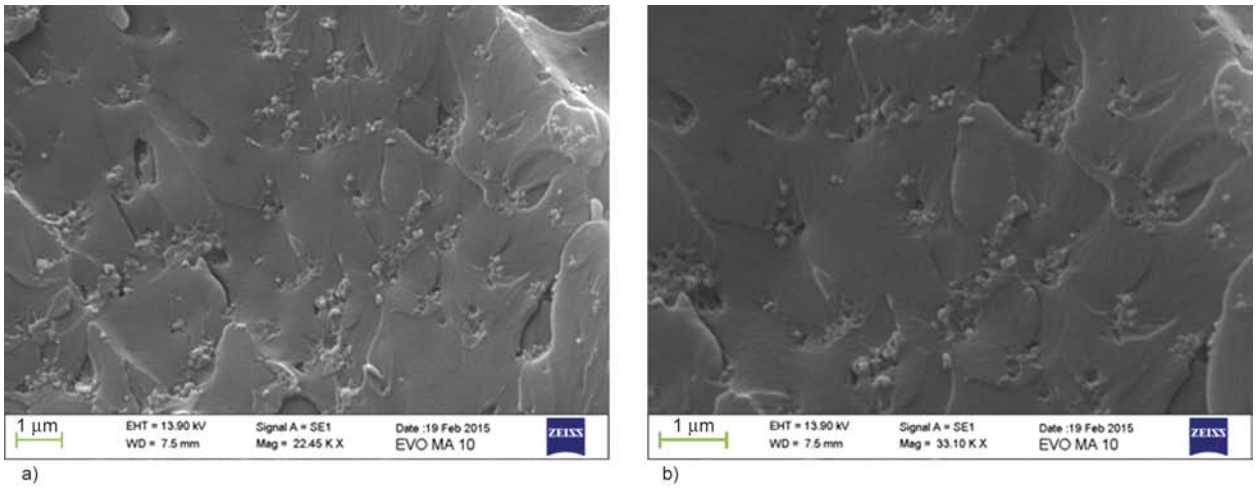

Figure 1. SEM images from the specimens with (a) 3 and (b) 5 phr barium ferrite content

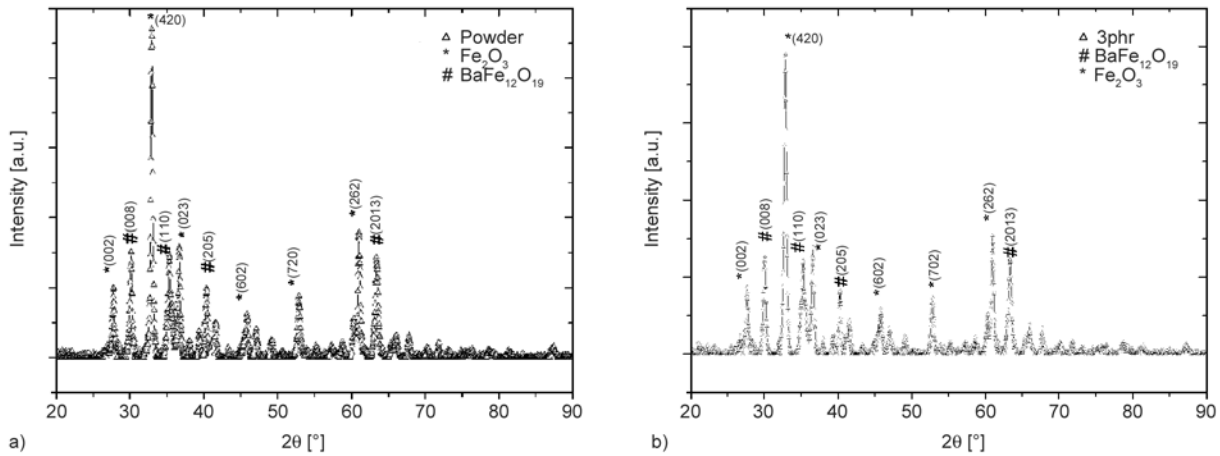

Figure 2. XRD spectra of (a) barium ferrite nanopowder, and (b) the composite with 3 phr barium ferrite

frequency, since dipoles attain sufficient time to orient themselves in the direction of the alternating field. Temperature facilitates this process by supplying thermal agitation to dipoles, and thus ε′ acquires high values in the low frequency and high temperature ranges. Two step-like transitions, recorded in the permittivity's spectra, indicate the presence of dielectric relaxation processes. Relaxation processes became evident in the loss tangent versus frequency and temperature spectra of Figure 3b, by the formation of loss peaks. Three distinct processes can be observed in Figure 3b. The slower process, recorded in the low frequency and high temperature region, characterized by the longer relaxation time, is attributed to Interfacial Polarization (IP). IP occurs in heterogeneous systems, because of the accumulation of unbounded charges at the interface of the constituents [22, 30, 31]. These charges form dipoles at the system's interface, which are forced to follow the alternation of the applied field. Their inertia to be aligned parallel to the field is responsible for the relaxation process, and enhanced polarization is achieved only at a low alternation rate of the field and when adequate amount of thermal energy is provided. In the intermediate zone of Figure 3b, another relaxation mechanism is present. Its physical origin is related to the simultaneous segmental motion of large parts of the macromolecular chains, due to the glass to rubber transition of the amorphous polymer matrix. This process, denoted as α-relaxation, corresponds to a shorter relaxation time compared to IP. It should be noted that glass transition temperature (T_g) of the employed epoxy resin, as determined via differential scanning calorimetry (DSC) studies in a previous work of ours [22], is very close to 60 °C. Above T_g, besides the synergetic motion of macromolecules, the difference of the coefficients of thermal expansion between matrix

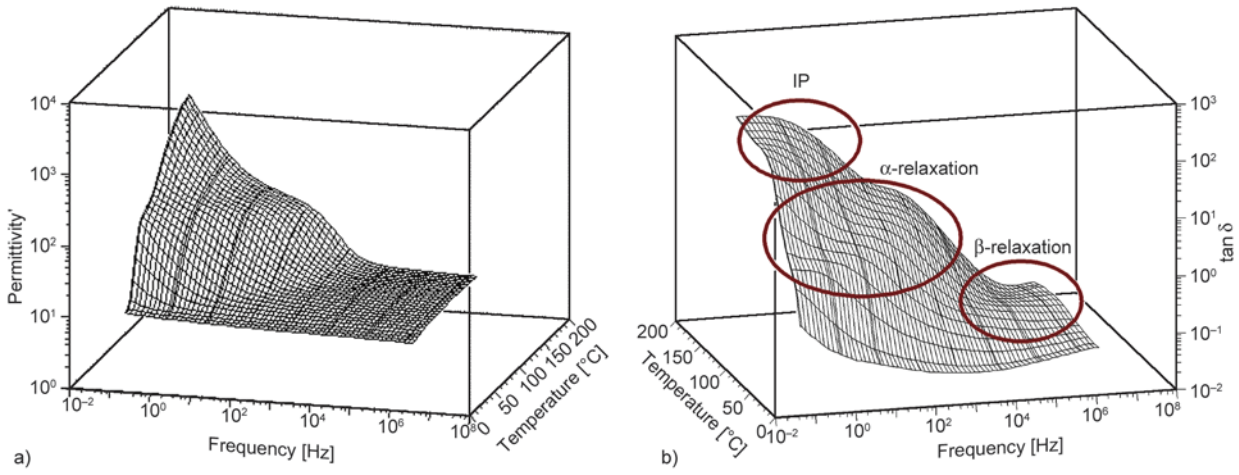

Figure 3. (a) Real part of dielectric permittivity, and (b) loss tangent as a function of frequency and temperature, for the composite with 20 phr barium ferrite

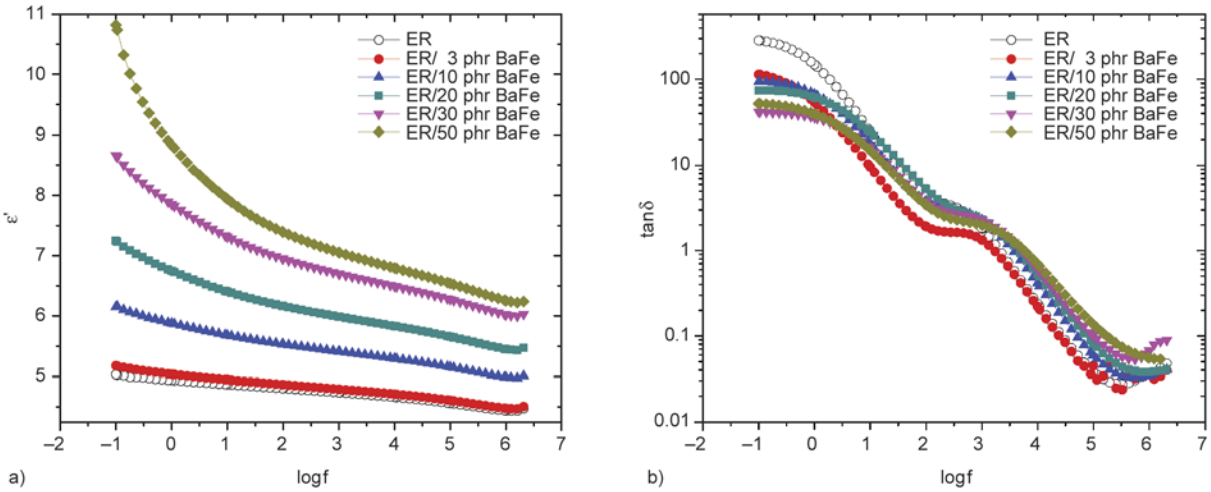

Figure 4. (a) Real part of dielectric permittivity, and (b) loss tangent vs frequency for all tested systems at 30 and 160 °C respectively

and filler could affect the dielectric response of the nanocomposites by the possible disruption of the particle/polymer contacts. The third process, occurring in the low temperature and high frequency region, is a relative weak mechanism ascribed to the re-orientation of polar side groups of the main polymer chains (β-relaxation) [22].

Figure 4a displays comparative plots of the real part of dielectric permittivity (ε'), as a function of frequency, for all the examined specimens, at 30 °C. As expected, ε' increases with filler content in the whole frequency range, since barium ferrite nanoparticles exhibit higher values of permittivity than the polymer matrix. This increase is more pronounced in the low frequency region, because system's heterogeneity increases with barium ferrite content, leading thus to enhanced IP effect. Comparative plots of the loss tangent ($\tan\delta$), as a function of frequency, for all the examined specimens, at 160 °C, are shown in Figure 4b. The previously mentioned relaxations are present in these loss spectra. Interestingly, IP is observed in the neat epoxy spectrum, and loss index attains high values. IP has been detected in loss spectra of many polymers due to the presence of additives, impurities and plasticizers [32–35]. On the other hand, increased values of loss tangent should be related to high values of the dielectric loss (ε''), since tanδ is defined as the ratio of the imaginary to the real part of dielectric permittivity. High values of ε'' in the low frequency region and at high temperatures are related to: (i) enhanced conductivity, (ii) IP, (iii) electrode polarization, or to any combination of these three effects. The low conductivity and low heterogeneity of the employed thermosetting resin implies electrode polarization, as the main reason for the high values of ε'', and thus of tan δ. Considering that the type of electrodes/specimens contact in all cases is the same, it is reasonable to suggest that the contribution of electrode polarization in the recorded values of dielectric loss remains constant. Under this point of view, and recalling the low values of conductivity for the examined systems, variations of dielectric loss and tanδ with filler content should be related to interfacial polarization phenomena. Thus, in the case of nanocomposites, values of tan δ appear to diminish with barium ferrite content, reflecting the increase of ε' due to the enhanced heterogeneity, and denoting IP as the dominating effect.

Magnetization hysteresis curves for barium ferrite nanopowder and $BaFe_{12}O_{19}$/epoxy nanocomposites are depicted in Figure 5a and 5b, respectively. Neat barium ferrite exhibits the highest values of magnetization and coercivity, Figure 5a. Additional nanocomposites' magnetization and coercivity increase systematically with filler content, as expected, Figure 5b.

Figures 5a and 5b show the magnetic hysteresis loops (M-H) of $BaFe_{12}O_{19}$ nanopowder and nanocomposites, respectively. Neat barium ferrite exhibits the highest values of magnetization. M-H curve of pure $BaFe_{12}O_{19}$ nanopowder shows a ferromagnetic hysteresis loop with magnetic saturation (M_s) 14 emu/g, magnetic remanence (M_r) 4.09 emu/g and coercive field (H_c) 1.3 kOe. The coercive field is significantly lower from the nominal value of $BaFe_{12}O_{19}$. The reason is that the $BaFe_{12}O_{19}$ nanoparticles, interacts with oxygen and a new phase Fe_2O_3 is formed

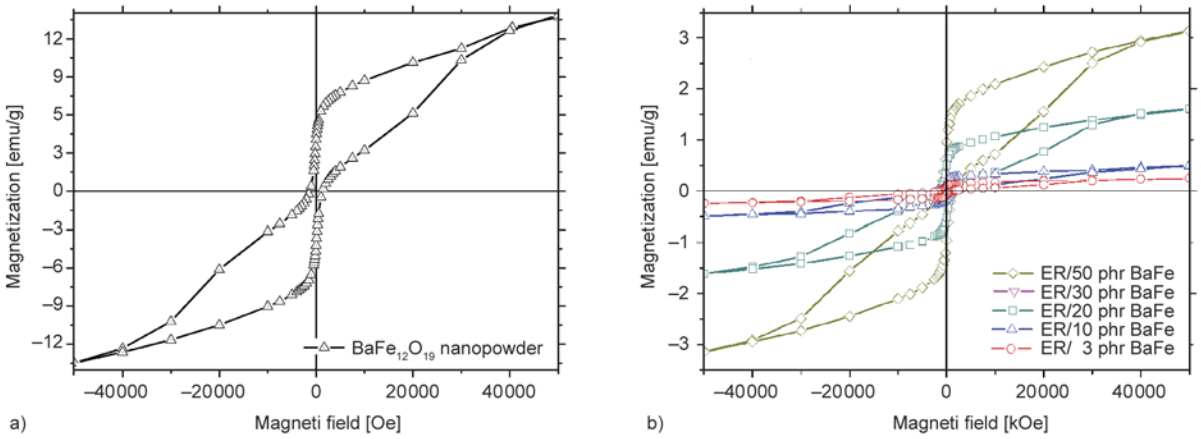

Figure 5. Magnetic hysteresis loops of (a) barium ferrite nanopowder, and (b) nanocomposites with different content of barium ferrite

and coexists with $BaFe_{12}O_{19}$ phase. The coercive field as an intrinsic property of the $BaFe_{12}O_{19}$ nanoparticles remains constant at nanocomposites with the same value of 1.3 kOe.

Increasing the magnetic nanoparticles' content, results in enhanced values of saturation and remanence magnetization in the nanocomposites. Obtained values of magnetic saturation and remanence magnetization are listed in Table 1. Barium ferrite nanoparticles induce magnetic properties to polymer matrix, and thus is quite reasonable the increase of magnetization, magnetic saturation and remanence magnetization of nanocomposites with magnetic phase content.

Figure 6 shows the water vapor sorption measurement for the nanocomposite with10 phr $BaFe_{12}O_{19}$, as a typical example. From the equilibrium mass at each relative humidity the sorption isotherm (equilibrium water content calculated in dry mass basis as a function of water activity (relative humidity/100)) can be constructed. The sorption isotherm for the nanocomposite with10 phr $BaFe_{12}O_{19}$ is shown in Figure 7. Data obtained during desorption are also included in the graph. The sorption isotherm is of Type II in the Brunauer classification [36], which describes adsorption on macroporous adsorbents with strong adsorbate-adsorbent interactions. The percentage of water content at the highest water activity was found close to 1.7 wt% indicating the hydrophobic character of the sample, while no significant hysteresis was found indicating that the adsorbed water do not cause permanent changes in the sample.

Experimental data were fitted by Guggenheim–Anderson–de Boer (GAB) equation (Equation (1)):

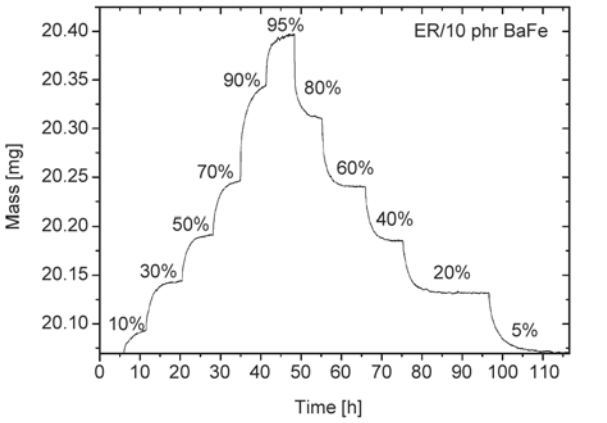

Figure 6. Typical water vapor sorption measurement. Mass as a function of time at 25 °C at different levels of relative humidity during sorption and desorption for the nanocomposite with 10 phr $BaFe_{12}O_{19}$.

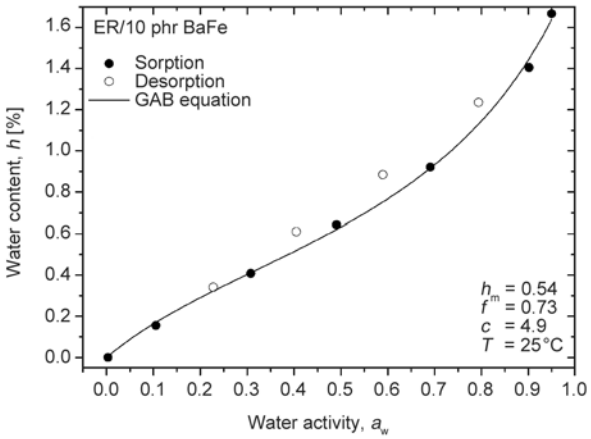

Figure 7. Sorption isotherm for the nanocomposite with 10 phr $BaFe_{12}O_{19}$ at 25 °C. Data during desorption (open symbols) are also included. The line is the best fit of GAB equation to the experimental data. The values of GAB parameters are indicated on the plot.

$$h(a_w) = h_m \cdot \frac{c \cdot f \cdot a_w}{(1 - f \cdot a_w)[1 + (c - 1) f \cdot a_w]} \quad (1)$$

where h is the percentage of water content calculated in dry mass basis $h = [(m_{equil} - m_{dry})/m_{dry}] \cdot 100\%$, a_w is the water activity (relative humidity/100), h_m is the percentage of water content directly bound to the hydrophilic sites, c is the ratio of the binding constants of water molecule directly bound to the sorption site in the first layer and of that bonded indirectly in the succeeding liquid-like layers, and f is the ratio of the standard chemical potential of the indirectly bound water molecule and that of the molecule in the bulk liquid state. The greater the value of c is, the stronger the bond between the water molecule and the hydrophilic site, while low values of f are indicative of hydrophobic character of polymer [37].

The values of the GAB equation parameters (shown on the graph of Figure 7) indicate the hydrophobic character of the sample (value of f) and the strong interaction of water molecules with its sorption sites (value of c). The values for the parameters of GAB equation are in accordance with those published in literature for epoxy resins [37]. No dependence of water sorption on sample composition was found as can be seen in Figure 8, where the sorption isotherms for all the systems studied are shown.

Kinetics of water vapor adsorption was studied and diffusion coefficient was calculated for different water contents from the measurements of the sample mass as a function of time at different levels of relative humidity. Experimental data for all the samples studied, independent of their composition, were well described by the one dimensional case of Fick's second law. The analysis was done as follows:

(i) By fitting the experimental data of mass as a function of time by the Equation (2):

$$m_t = m_{t=0} + (m_{t=\infty} - m_{t=0}) \cdot \left[1 - \exp\left[-7.3\left(\frac{D \cdot t}{l^2}\right)^{0.73}\right]\right] \quad (2)$$

where m_t is the sample mass at each time t, l is the thickness of the sample and $m_{t=0}$ and $m_{t=\infty}$ are the initial and the equilibrium mass, respectively and D is the diffusion coefficient [37].

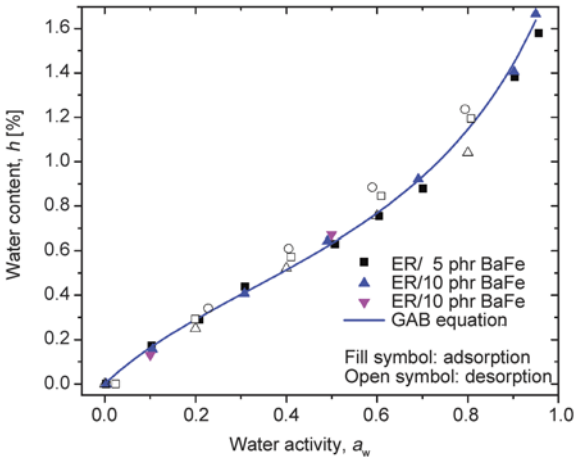

Figure 8. Water content as a function of water activity during adsorption (full symbols) and desorption (open symbols), for the nanocomposites indicated on the plot. The line is the best fit of GAB equation to the experimental data of the 10 phr $BaFe_{12}O_{19}$/epoxy nanocomposite.

(ii) By plotting the data of $(m_t - m_{t=0})/(m_{t=\infty} - m_{t=0})$ as a function of $\sqrt{t}$ and calculated diffusion coefficient from Equation (3):

$$D = slope^2 \cdot \frac{l^2 \cdot \pi^2}{16} \quad (3)$$

where *slope* is the initial slope (for y values up to 0.6) and l is the thickness of the sample [37].

Similar values for the diffusion coefficient were calculated by both ways of fitting described above. The values of diffusion coefficient obtained from the experimental data of sorption as well as of desorption are presented in Figure 9 for all the samples

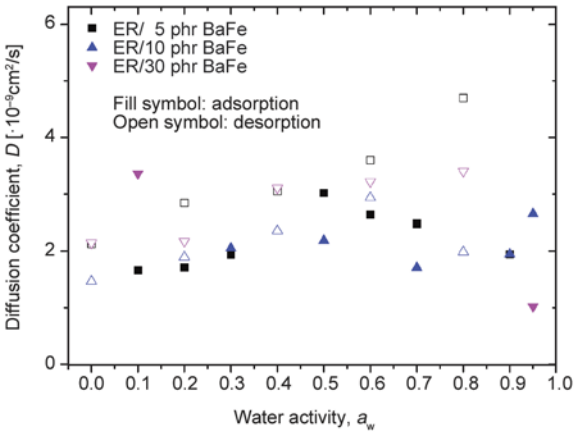

Figure 9. Diffusion coefficient values calculated from experimental data taken during adsorption (full symbols) and desorption (open symbols) as a function of water activity for the nanocomposites indicated on the plot

under investigation. During adsorption a scattering of the data around the value of $2 \cdot 10^{-9}$ cm^2/s independent of the sample composition and water activity (water content) was found, while during desorption diffusion coefficient values decrease with decreasing water activity (water content).

The hydrophobic character of the studied materials could be proved beneficial in their service life, especially in outdoors applications and in environmental conditions with high humidity. The unaffected, by water adsorption, polymer matrix will act as a protective shield for the reinforcing inclusions and thus their magneto-electric performance will not be disturbed.

4. Conclusions

In the present study composite systems of epoxy resin and barium ferrite nanoparticles have been prepared, and studied varying the content of the inclusions. The recorded dielectric relaxations are related to both the polymer matrix and the presence of the reinforcing phase. Dielectric permittivity and loss are increasing with filler and temperature. Effect of temperature is more pronounced in the low frequency range. Permittivity values diminish rapidly with frequency, reflecting the polarization vanishing, since permanent and induced dipoles fail to follow the alternation of the applied electric field. From the magnetization curves the coercive field decreases to 1.3 kOe due to the presence of Fe_2O_3 in the powder. The saturation magnetization of nanocomposites decreases with decreasing of magnetic powder content.

Independent on their composition the nanocomposites absorb a small amount of water (percentage of water content at the highest water activity equal to 1.7 wt%), indicating their hydrophobic character, while the adsorbed water do not cause permanent changes in the sample, which both are of great importance for their service life.

Acknowledgements

This research has been co-financed by the European Union (European Social Fund – ESF) and Greek national funds through the Operational Program 'Education and Lifelong Learning' of the National Strategic Reference Framework (NSRF) – Research Funding Program: THALES, MIS 379346 Investing in knowledge society through the European Social Fund.

References

[1] Walz F., Rivas J., Martínez D., Kronmüller H.: Influence of Ba content on the magnetic after-effect spectra in barium ferrites. Physica Status Solidi (a), **143**, 137–148 (1994).
DOI: 10.1002/pssa.2211430118

[2] Shi S., Yang Y., Xu J., Li L., Zhang X., Hu G-H., Dang Z-M.: Structural, optical and magnetic properties of *co*-doped ZnO nanorods prepared by hydrothermal method. Journal of Alloys and Compounds, **576**, 59–65 (2013).
DOI: 10.1016/j.jallcom.2013.04.011

[3] Zhang L., Zhou P., Zhang H., Lu L., Zhang G., Chen H., Lu H., Xie J., Deng L.: A broadband radar absorber based on perforated magnetic polymer composites embedded with FSS. IEEE Transactions on Magnetics, **50**, 4004305/1–4004305/5 (2014).
DOI: 10.1109/TMAG.2013.2293129

[4] Dong C., Wang X., Zhou P., Liu T., Xie J., Deng L.: Microwave magnetic and absorption properties of M-type ferrite $BaCo_xTi_xFe_{12-2x}O_{19}$ in the Ka band. Journal of Magnetism and Magnetic Materials, **354**, 340–344 (2014).
DOI: 10.1016/j.jmmm.2013.11.008

[5] Huang X., Zhang J., Xiao S., Sang T., Chen G.: Unique electromagnetic properties of the zinc ferrite nanofiber. Materials Letters, **124**, 126–128 (2014).
DOI: 10.1016/j.matlet.2014.03.049

[6] Huang X., Zhang J., Xiao S., Chen G.: The cobalt zinc spinel ferrite nanofiber: Lightweight and efficient microwave absorber. Journal of the American Ceramic Society, **97**, 1363–1366 (2014).
DOI: 10.1111/jace.12909

[7] Huang X., Zhang J., Liu Z., Sang T., Song B., Zhu H., Wong C.: Facile preparation and microwave absorption properties of porous hollow $BaFe_{12}O_{19}/CoFe_2O_4$ composite microrods. Journal of Alloys and Compounds, **648**, 1072–1075 (2015).
DOI: 10.1016/j.jallcom.2015.07.073

[8] Huang X., Chen Y., Yu J., Zhang J., Sang T., Tao G., Zhu H.: Fabrication and electromagnetic loss properties of Fe_3O_4 nanofibers. Journal of Materials Science: Materials in Electronics, **26**, 3474–3478 (2015).
DOI: 10.1007/s10854-015-2857-y

[9] Tan Y., Tang J., Deng A., Wu Q., Zhang T., Li H.: Magnetic properties and microwave absorption properties of chlorosulfonated polyethylene matrices containing graphite and carbonyl-iron powder. Journal of Magnetism and Magnetic Materials, **326**, 41–44 (2013).
DOI: 10.1016/j.jmmm.2012.08.021

[10] Song Z., Xie J., Zhou P., Wang X., Liu T., Deng L.: Toughened polymer composites with flake carbonyl iron powders and their electromagnetic/absorption properties. Journal of Alloys and Compounds, **551**, 677–681 (2013).
DOI: 10.1016/j.jallcom.2012.11.065

[11] Sim B., Chae H. S., Choi H. J.: Fabrication of polyaniline coated iron oxide hybrid particles and their dual stimuli-response under electric and magnetic fields. Express Polymer Letters, **9**, 736–743 (2015). DOI: 10.3144/expresspolymlett.2015.68

[12] Ren L., Zhao J., Wang S-J., Han B-Z, Dang Z-M.: Dielectric and magnetic properties of Fe@Fe_xO_y/epoxy resin nanocomposites as high-performance electromagnetic insulating materials. Composites Science and Technology, **114**, 57–63 (2015). DOI: 10.1016/j.compscitech.2015.04.003

[13] Ren L., Zhao J., Wang S-J., Zha J-W., Hu G-H., Dang Z-M.: Remarkably variable dielectric and magnetic properties of poly(vinylidene fluoride) nanocomposite films with triple-layer structure. Composites Science and Technology, **107**, 107–112 (2015). DOI: 10.1016/j.compscitech.2014.12.008

[14] Raptis C. G., Patsidis A., Psarras G. C.: Electrical response and functionality of polymer matrix-titanium carbide composites. Express Polymer Letters, **4**, 234–243 (2010). DOI: 10.3144/expresspolymlett.2010.30

[15] Vavouliotis A., Fiamegou E., Karapappas P., Psarras G. C., Kostopoulos V.: DC and AC conductivity in epoxy resin/multiwall carbon nanotubes percolative system. Polymer Composites, **31**, 1874–1880 (2010). DOI: 10.1002/pc.20981

[16] Frickel N., Greenbaum A. G., Gottlieb M., Schmidt A. M.: Magnetic properties and dielectrical relaxation dynamics in $CoFe_2O_4$@PU nanocomposites. The Journal of Physical Chemistry C, **115**, 10946–10954 (2011). DOI: 10.1021/jp111348e

[17] Yang W., Yu S., Luo S., Sun R., Liao W-H., Wong C-P.: A systematic study on electrical properties of the $BaTiO_3$–epoxy composite with different sized $BaTiO_3$ as fillers. Journal of Alloys and Compounds, **620**, 315–323 (2015). DOI: 10.1016/j.jallcom.2014.09.142

[18] Psarras G. C.: Charge transport properties in carbon black/polymer composites. Journal of Polymer Science Part B: Polymer Physics, **45**, 2535–2545 (2007). DOI: 10.1002/polb.21278

[19] Toner V., Polizos G., Manias E., Randall C. A.: Epoxy-based nanocomposites for electrical energy storage. I: effects of montmorillonite and barium titanate nanofillers. Journal of Applied Physics, **108**, 074116/1–074116/14 (2010). DOI: 10.1063/1.3487275

[20] Asimakopoulos I. A., Psarras G. C., Zoumpoulakis L.: Barium titanate/polyester resin nanocomposites: Development, structure-properties relationship and energy storage capability. Express Polymer Letters, **8**, 692–707 (2014). DOI: 10.3144/expresspolymlett.2014.72

[21] Tomara G. N., Kerasidou A. P., Patsidis A. C., Karahaliou P. K., Psarras, G. C., Georga S. N., Krontiras C. A.: Dielectric response and energy storage efficiency of low content TiO_2-polymer matrix nanocomposites. Composites Part A: Applied Science and Manufacturing, **71**, 204–211 (2015). DOI: 10.1016/j.compositesa.2015.01.017

[22] Mathioudakis G. N., Patsidis A. C., Psarras G. C.: Dynamic electrical thermal analysis on zinc oxide/epoxy resin nanodielectrics. Journal of Thermal Analysis and Calorimetry, **116**, 27–33 (2014). DOI: 10.1007/s10973-013-3510-8

[23] Maliakal A., Katz H., Cotts P. M., Subramoney S., Mirau P.: Inorganic oxide core, polymer shell nanocomposite as a high *K* gate dielectric for flexible electronics applications. Journal of the American Chemical Society, **127**, 14655–14662 (2005). DOI: 10.1021/ja052035a

[24] Iijima M., Sato N., Lenggoro I. W., Kamiya H.: Surface modification of $BaTiO_3$ particles by silane coupling agents in different solvents and their effect on dielectric properties of $BaTiO_3$/epoxy composites. Colloids and Surfaces A: Physicochemical and Engineering Aspects, **352**, 88–93 (2009). DOI: 10.1016/j.colsurfa.2009.10.005

[25] Xie L., Huang X., Wu C., Jiang P.: Core-shell structured poly(methyl methacrylate)/$BaTiO_3$ nanocomposites prepared by *in situ* atom transfer radical polymerization: A route to high dielectric constant materials with the inherent low loss of the base polymer. Journal of Materials Chemistry, **21**, 5897–5906 (2011). DOI: 10.1039/c0jm04574h

[26] Zhang X., Chen H., Ma Y., Zhao C., Yang W.: Preparation and dielectric properties of core–shell structural composites of poly(1H,1H,2H,2H-perfluorooctyl methacrylate)@$BaTiO_3$ nanoparticles. Applied Surface Science, **277**, 121–127 (2013). DOI: 10.1016/j.apsusc.2013.03.178

[27] Zhang X., Ma Y., Zhao C., Yang W.: High dielectric constant and low dielectric loss hybrid nanocomposites fabricated with ferroelectric polymer matrix and $BaTiO_3$ nanofibers modified with perfluoroalkylsilane. Applied Surface Science, **305**, 531–538 (2014). DOI: 10.1016/j.apsusc.2014.03.131

[28] Tantis I., Psarras G. C., Tasis D.: Functionalized graphene – poly(vinyl alcohol) nanocomposites: Physical and dielectric properties. Express Polymer Letters, **6**, 283–292 (2012). DOI: 10.3144/expresspolymlett.2012.31

[29] Dalle Vacche S., Leterrier Y., Michaud V., Damjanovic D., Månson J. A. E.: The influence of $BaTiO_3$ surface modification on the dielectric and electromechanical properties of poly (vinylidene fluoride) copolymer composites. in 'Proceedings of the Fourth International Conference on Multifunctional, Hybrid and Nanomaterials' Sitges, Spain, P153 (2015).

[30] Psarras G. C., Siengchin S., Karahaliou P. K., Georga S. N., Krontiras C. A., Karger-Kocsis J.: Dielectric relaxation phenomena and dynamics in polyoxymethylene/polyurethane/alumina hybrid nanocomposites. Polymer International, **60**, 1715–1721 (2011).
DOI: 10.1002/pi.3136

[31] Pontikopoulos P. L., Psarras G. C.: Dynamic percolation and dielectric response in multiwall carbon nanotubes/poly(ethylene oxide) composites. Science of Advanced Materials, **5**, 14–20 (2013).
DOI: 10.1166/sam.2013.1425

[32] Singha S., Thomas M. J., Kulkarni A.: Complex permittivity characteristics of epoxy nanocomposites at low frequencies. IEEE Transactions on Dielectrics and Electrical Insulation, **17**, 1249–1258 (2010).
DOI: 10.1109/TDEI.2010.5539697

[33] Singha S., Thomas M. J.: Dielectric properties of epoxy nanocomposites. IEEE Transactions on Dielectrics and Electrical Insulation, **15**, 12–23 (2008).
DOI: 10.1109/T-DEI.2008.4446732

[34] Patsidis A. C., Kalaitzidou K., Psarras G. C.: Dielectric response, functionality and energy storage in epoxy nanocomposites: Barium titanate vs exfoliated graphite nanoplatelets. Materials Chemistry and Physics, **135**, 798–805 (2012).
DOI: 10.1016/j.matchemphys.2012.05.060

[35] Chalashkanov N. M., Dodd S. J., Dissado L. A., Fothergill J. C.: Re-examination of the dielectric spectra of epoxy resins: Bulk charge transport and interfacial polarization peaks. IEEE Transactions on Dielectrics and Electrical Insulation, **21**, 1330–1341 (2014).
DOI: 10.1109/TDEI.2014.6832281

[36] Brunauer S., Deming L. S., Deming W. E., Teller E.: On a theory of the van der Waals adsorption of gases. Journal of the American Chemical Society, **62**, 1723–1732 (1940).
DOI: 10.1021/ja01864a025

[37] Maggana C., Pissis P.: Water sorption and diffusion studies in an epoxy resin system. Journal of Polymer Science Part B: Polymer Physics, **37**, 1165–1182 (1999).
DOI: 10.1002/(SICI)1099-0488(19990601)37:11<1165::AID-POLB11>3.0.CO;2-E

eXPRESS Polymer Letters Vol.10, No.3 (2016) 237–247
Available online at www.expresspolymlett.com
DOI: 10.3144/expresspolymlett.2016.22

Optimization of the crystallinity of polypropylene/submicronic-talc composites: The role of filler ratio and cooling rate

A. Makhlouf[1], *H. Satha*[1*], *D. Frihi*[1], *S. Gherib*[1], *R. Seguela*[2]

[1]Laboratoire des Silicates, Polymères et Nanocomposites, Université 8 Mai 1945, BP 401, 24000 Guelma, Algérie
[2]MATEIS, INSA de Lyon – CNRS UMR5510, Campus LyonTech La Doua, 69621 Villeurbanne, France

Received 31 July 2015; accepted in revised form 12 October 2015

Abstract. Micronic and submicronic mineral fillers recently appeared as efficient reinforcing agents for polyolefins in addition to the benefit of bypassing the exfoliation/dispersion problem encountered in the case of incorporation of nanoscopic fillers such as clay. Submicronic-talc, designated as μ-talc, belongs to this kind of new fillers. This work was aimed at searching to optimize the crystallinity ratio of isotactic polypropylene in the presence of μ-talc in relation to the filler ratio of the composites and the cooling rate from the melt. In order to highlight the efficiency of the μ-talc on the crystallization of polypropylene comparison has been made with PP composites containing conventional talc particles. The study has been carried out on samples having μ-talc weight fractions covering the range 3–30%. In the context of optimizing the crystallinity ratio of the polypropylene matrix in the composites, calorimetric experiments have been planned using a full factorial design. The results were statistically processed by analysis of the variance via mathematical models for predicting the crystallinity ratio in relation to the cooling rate and the filler ratio. Contour graphs have been plotted to determine the effect of each parameter on crystallinity. The cooling rate proved to have a significantly stronger influence on crystallinity than the type and content of filler.

Keywords: *polymer composites, polypropylene composite, micro-talc, crystallinity, ANOVA method*

1. Introduction

Isotactic polypropylene (iPP) filled with mineral particles such as calcium carbonate ($CaCO_3$) or with short glass fibers has been the subject of a lot of research [1–8]. The role of fillers in polymer based composites is multiple: it helps reducing the composite cost as it is generally less expensive than the polymer, but it also contributes to improving the mechanical performances and the physical properties if properly dispersed in the polymer matrix.

Isotactic polypropylene (iPP) is one of the most widely used semi-crystalline polymer for structural applications in the automotive industry, household appliances, construction, packaging, ropes, etc.

Mineral fillers proved to provide a toughening effect on iPP bulk pieces due to the ability to initiate elementary plasticity processes at the particle-matrix interface [3–8].

Since the early 80's, profuse studies have been devoted to the mechanical reinforcement of iPP by nanofillers such as clay [9–11]. Such kinds of nanofillers were shown to noticeably improve the fire-resistance of thermoplastic polymers [12] in addition to the mechanical performances. In the case of polymer matrices such as iPP having poor if any interaction with the nanofillers, surface treatment techniques of the nanoparticles were required as well as

*Corresponding author, e-mail: sathahamid@yahoo.fr

specific preparation methods involving the use of compatibilizing agents.

Among mineral fillers, talc proved to have a good potential of development for iPP-based composites, noticeably in the automotive industry [13–17]. It appeared very soon that talc displayed a strong nucleating effect for iPP [14, 19–23] due to specific physico-chemical interactions between the filler and the polymer matrix that promote epitaxial crystallization [14, 24–27]. This effect was significantly more pronounced than for other common fillers such as $CaCO_3$ or kaolin and therefore give rise to better improvement of mechanical properties [14, 18]. This property makes talc able to be easily incorporated in iPP matrix without the use of a chemical surface treatment [14, 17, 22], though the use of such treatment was reported to be efficient for dispersion of very fine particles at high loading [28–34].

It is worth noticing that talc reduces the efficiency of heat-stabilizing agents in iPP-based composites and by the way the fire-resistance of these composites [35, 36]. However, a significant advantage of talc compared to $CaCO_3$ or kaolin from a practical viewpoint is that it is much less abrasive for the extruder during the compounding and injection-molding stages.

Works regarding the mechanical reinforcement of iPP with talc have been orientated towards submicronic powders, i.e. intermediate size between conventional and nanometric fillers [15–17]. Using such filler particles with sub-micronic size enables to increase the specific area of the filler with respect to the former kind of fillers and to overcome the quite common problem of exfoliation and dispersion of the second kind of fillers. Besides, unlike $CaCO_3$ and kaolin, μ-talc has been developed as a lamellar-like filler thanks to a specific delamination technique from the producer that provides better reinforcing capacities at equivalent volume fraction [17, 37], owing to a very good dispersion that prevents the detrimental formation of aggregates [38]. It was shown in a previous study that the combination of the nucleating effect and the lamellar-like shape of μ-talc particles generates a rigid percolating network of polymer crystallites and filler particles that contributes to the enhancement of the composite stiffness [36]. However, a possible drawback of the nucleation ability of talc on iPP is a reduced toughness due to the increase of crystallinity [39].

Therefore, it appears that the structure-property relationships of μ-talc-reinforced iPP deserved further studies. The aim the present work was to investigate the effect of incorporation of μ-talc on the crystallization potential of an iPP matrix in comparison with conventional PP composites with standard talc particles having a 3-times lower specific surface area. The cooling rate from the melt is also under concern in this study since it is well known to significantly influence the crystallization capabilities of semi-crystalline polymers, especially polypropylene [40–42]. A numerical analysis of the data has been used to optimize the composite crystallinity in relation to the filler ratio and the cooling rate.

2. Experimental

2.1. Materials

The polymer under investigation in this work is an isotactic polypropylene (iPP) from Solvay (Brussels, Belgium) with an isotacticity index of 96% according to the manufacturer. The weight-average molar mass was M_w = 380 000 g/mol and the polydispersity index IP = 12, as determined by size exclusion chromatography. The sub-micronic size talc (μ-talc) without any surface treatment was supplied by Imerys Talc (Luzenac, France) under trade name HAR®Talc (High Aspect Ratio Talc). This new kind of filler was produced by delamination milling instead of gridding or micronizing. Standard talc (S-talc) was also used for the sake of comparison. The specific area of the present μ-talc is 17 m^2/g as compared to 6 m^2/g for S-talc, using the Brunauer-Emmett-Teller method, according to the manufacturer. The average aspect ratio of the platelets, 5.5 and 1.3 for μ-talc and S-talc respectively, was determined by scanning electron microscopy. All the composites were compounded by Multibase/Dow Corning (Saint Laurent du Pont, France) without compatibilizing agent using a Clextral BC21 twin screw extruder (Firminy, France) of length 1200 mm and diameter 25 mm, the temperature being 180–210 °C between feeder and die. The composites were finally injection-molded into 2 mm thick sheets.

The actual filler ratio of the various composites was precisely determined after compounding by means of thermogravimetry [37]. The actual ratio was very close to the nominal value adjusted at the stage of compounding, the standard deviation not exceeding 1%, so that the nominal values were taken into account in this study.

2.2. Thermogravimetric analysis

Thermogravimetric analysis (TGA) was performed on a Shimadzu DTG60 apparatus (Kyoto, Japan) under nitrogen gas flow. The heating rate was 10 °C/min over the temperature range 25–650 °C. The sample weight was about 10 mg.

2.3. Differential scanning calorimetry

Differential scanning calorimetry (DSC) was carried out on a SETARAM apparatus (Lyon, France), model LABSYS evo. The temperature and heat flow scales were calibrated using high purity indium at a heat rate of 10 °C/min. The samples of about 10 mg were heated up from 25 to 210 °C and held at 210 °C for 5 min in order to erase surviving iPP nuclei and thermal history due to processing. This methodology enabled determining the actual nucleating effect of μ-talc. The samples were then cooled down to 25 °C at various cooling rates in the range 2–40 °C/min. Subsequent heating was performed at 10 °C/min in order to record the melting endotherm and determine the melting enthalpy. The crystal weight fraction was then computed from Equation (1):

$$X_c = \frac{\Delta H_f}{\Delta H_f^\circ} \quad (1)$$

where ΔH_f is the melting enthalpy of the polymer and ΔH_f° = 207 J/g is the melting enthalpy of perfectly crystalline PP in the α-crystal form [43]. In the case of composites, the actual weight fraction of the matrix polymer was taken into account.

2.4. Wide-angle X-ray scattering

Wide-angle X-ray scattering (WAXS) experiments were carried out at room temperature in transmission mode on a laboratory bench equipped with a Rigaku rotating Cu-anode (Tokyo, Japan) operated at 100 kV and 40 mA. The X-ray beam was collimated with Göbel mirrors from Xenocs (Grenoble, France) that provided a monochromatic Cu-Kα radiation (wavelength = 0.154 nm) and parallel point focusing thanks to two pairs of anti-scattering slits. The 2D-WAXS patterns were recorded on a SCX2D-CCD camera from Princeton Instruments (Trenton NJ, USA). Data corrections were performed for transmission coefficient and background scattering. Azimuthal integration of the 2D patterns was performed using FitD2 software in order to get intensity profiles as a function of the scattering angle. This enabled to characterize the crystalline texturing of the samples induced by the injection-molding process in addition to the identification of their crystalline form. The samples were punched out from the sheets as shown in Figure 1. All samples were analyzed with the X-ray beam parallel to each of the 3 main directions, i.e. injection, transverse and thickness directions.

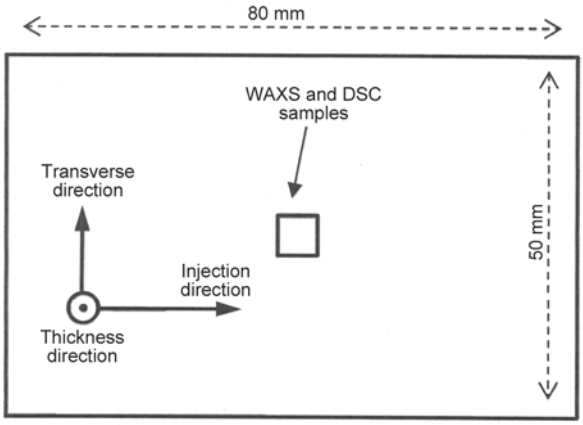

Figure 1. Schematic of the injection-moulded sheet and characteristic directions

2.5. Scanning electron microscopy

Scanning electron microscopy (SEM) experiments were performed on a JOEL JSM 840A apparatus (Tokyo, Japan) in topographic mode at an acceleration voltage of 20 kV. Observations were made from the metal-coated surface of samples broken in liquid nitrogen. The microscope was equipped with an energy-dispersive X-ray (EDX) device that enabled identifying the elements from the talc platelets.

2.6. Design and planning of experiments

A design of experiments (DOE) approach was adopted for optimizing the crystallinity ratio, the two variables being the filler ratio and the cooling rate. The aim of this analysis was to identify the statistical relevance of the factors under investigation and their interactions and consequences on the response [44–47]. The ANOVA variance analysis was used to determine the mathematical law. The 3D response surfaces (RS) were constructed by using the Design-Expert-8 statistics software.

Using the RS method enables 1) to model the response Y under consideration as a function of the independent variables X_1, X_2, …, X_i, … and 2) to determine the interaction of these variables and their respective influence on the response Y. The second order regression used for the modelling is given by Equation (2):

$$Y = a_0 + \sum_{i=1}^{k} a_i X_i + \sum_{i=1}^{k} a_{ii} X_i^2 + \sum_{i<j}^{k} a_{ij} X_i X_j \quad (2)$$

where k is the number of independent variable parameters. In the present study, the response Y is featuring the crystallinity ratio while the independent variables X_1 and X_2 hold for the cooling rate, C_R, and the filler ratio, F_R.

The strategy of planning of the experiments aims at carrying out the experiments in an optimal way for the modelling. The number of trials, N, is related to the number of variables, k, and the level of variation of these variables, q, via Equation (3):

$$N = q^k \quad (3)$$

In the present study, $k = 2$ and $q = 7$ according to Table 1 data, so that $N = 49$. The variable values for the trials are listed in Table 1.

Table 1. Data of the planning of experiments

Level	C_R [°C/min]	F_R [%]
1	2	0
2	5	3
3	10	5
4	15	7
5	20	10
6	30	20
7	40	30

3. Experimental results

In the previous study it was clearly shown that iPP/μ-talc composites exhibit significantly enhanced mechanical properties as compared to iPP/S-talc composites, at equivalent filler loading [36]. Only the thermal and structural behavior of the iPP/μ-talc composites will be addressed here, in comparison with the iPP/S-talc relatives.

3.1. Thermogravimetric analysis

Figure 2 shows the loss of mass plotted versus temperature. The residual mass of the samples after heating beyond 550 °C is very close to that expected from the weight fraction of filler introduced at the processing stage, for all composites. Another observation from Figure 2 is that the curves gradually shift to higher temperature with increasing talc content indicating an improved resistance to thermal decomposition. Moreover, the shift of the curves for the μ-talc composites is more notable than those for the industrial talc composites at the same filler loading. This emphasizes the benefiting effect of μ-talc compared to conventional talc from the viewpoint of fire-resistance owing to its higher specific surface area that enhances the intumescence activity [26].

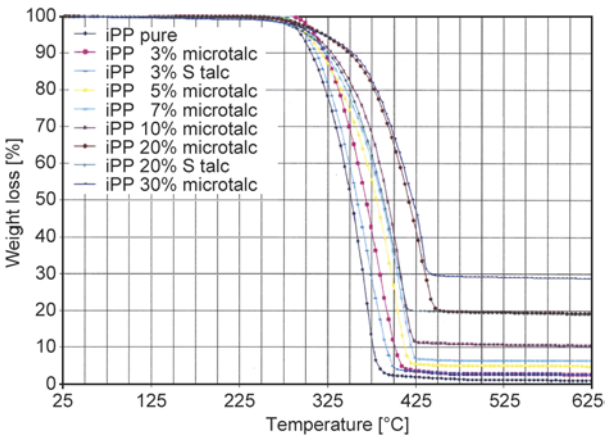

Figure 2. Weight loss of the iPP/μ-talc composites as a function of temperature

3.2. Structural characterization

Figure 3 reports the DSC cooling traces of iPP and iPP/μ-talc composites containing 10 and 30% of μ-talc. The gradual shift to higher temperature of the crystallization exotherm with increasing μ-talc content clearly reveals the nucleating effect of the talc particles that promotes an early initial crystallization of the PP matrix. Regarding the peak of the exotherm that is more relevant to the global crystallization rate including nucleation and growth, the very slight difference between the 10 and 30% μ-talc composites (Figure 3) suggests that a hindrance to the global crystallization occurs at high μ-talc loading. Such a phenomenon has been reported to occur in nanocom-

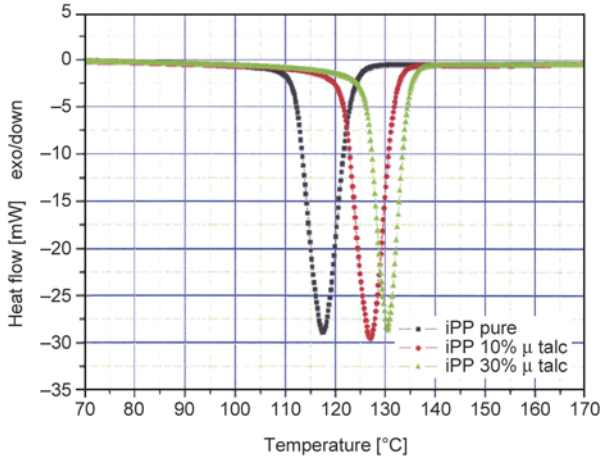

Figure 3. DSC crystallization curves of pure iPP and the composites iPP/10% μ-talc and iPP/30% μ-talc upon cooling at 10 °C/min from 210 °C

posites as well as conventional composites based on various semi-crystalline polymer matrices [48–54]. The current explanation is that at high loads the filler particles generate a physical barrier to the crystal lamella growth and thus limit the crystallization efficiency. This point will be further discussed regarding the effect of μ-talc content on the crystallinity ratio.

The nucleating effect of μ-talc is compared in Figure 4 to that of S-talc through the DSC cooling traces of the composites for the same filler loading value F_R = 20% and same cooling rate C_R = 10 °C/min. The shift to high temperature of the crystallization exotherm is slightly greater for μ-talc, indicating better nucleating effect of the latter one due to its 3-fold higher specific surface area compared to S-talc.

The WAXS intensity profiles along 3 directions of the parallelepipedic samples of iPP and the iPP/7% μ-talc composite are reported in Figures 5 and 6. Only the main reflections of the monoclinic α-form of iPP are observed for both the pure sample and the composite. This is consistent with previous reports that talc is an α-nucleating agent for iPP [19–27]. The 3 intensity profiles of the pure iPP display a great similarity relevant of a structural isotropy (Figure 5). In contrast the strongly different profiles along for the iPP matrix in the iPP/7% μ-talc composite are indicative of a strong crystalline texturing due to both the injection-molding and nucleating effect (Figure 6). Particularly, the very weak intensity of the (040) reflection of iPP in the WAXS profile through the thickness is a clear indication that the iPP chains are lying in the sample plane [23–27]. Moreover, the total absence of the

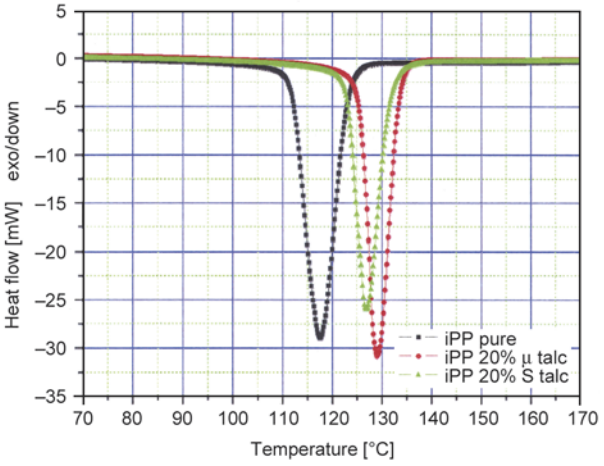

Figure 4. DSC crystallization curves of pure iPP and the composites iPP/20% μ-talc and iPP/20% S-talc upon cooling at 10 °C/min from 210 °C

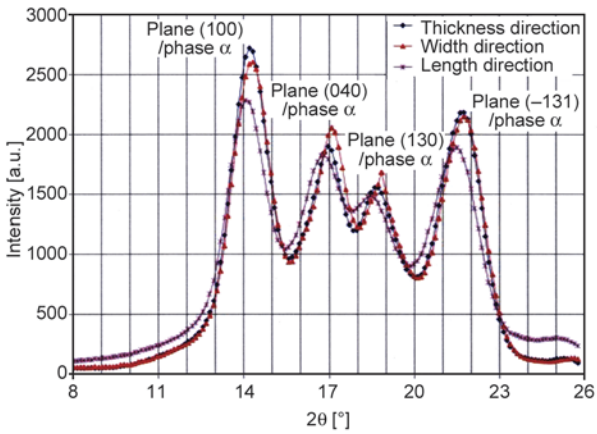

Figure 5. WAXS intensity profiles of pure iPP (injection-molding)

(002) reflection of talc on the WAXS profile through the sample thickness (Figure 6) reveals that the talc platelets are also lying within the sample plane. Indeed, the (002) planes characteristic of the silicate sheets of talc stand along the larger dimensions of the talc platelets. The combination of this crystallographic characteristic of the talc platelets and their nucleating effect results in an orientation of the iPP crystals nearly normal to the talc platelets [23–27]. This concomitance of orientation of the chains and the talc platelets is a common feature of injection-molded composites reinforced with filler of high aspect ratio which tend to align along the flow direction [27, 33, 55–57]. In the case of composites with lamellar fillers, this phenomenon is enhanced by to the so-called shear-amplification effect [58].

The shear-induced nucleation can compete with filler-induced nucleation [59] and may even prevail on it [33]. In the present study, the thermal treatment

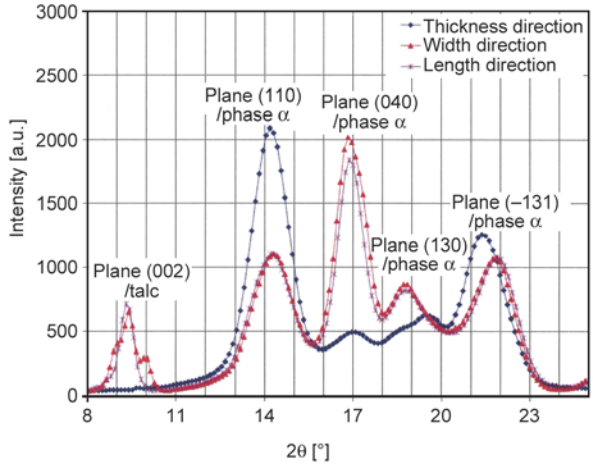

Figure 6. WAXS intensity profiles of the iPP/7% μ-talc composite (injection-molding)

of the samples at $T = 210\,°C$ for 5 min prior to the DSC crystallization experiments was carried out in order to erase any shear-induced chain orientation due to processing. Therefore, the sensitivity of the crystallization kinetics of the iPP/μ-talc composites to the filler content can be assigned to the μ-talc surface nucleation due to favorable surface free energy [26].

Scanning electron ricroscopy was also used for further structural characterization of the composites. Figure 7 shows a SEM image from the facture surface of an iPP/30% μ-talc composite. The talc platelets appear to be fairly well dispersed and aligned along the injection direction. Better identification of the talc platelets and confirmation of both their dispersion and orientation is provided by the corresponding EDX images showing the distributions of the Si and Mg elements from talc.

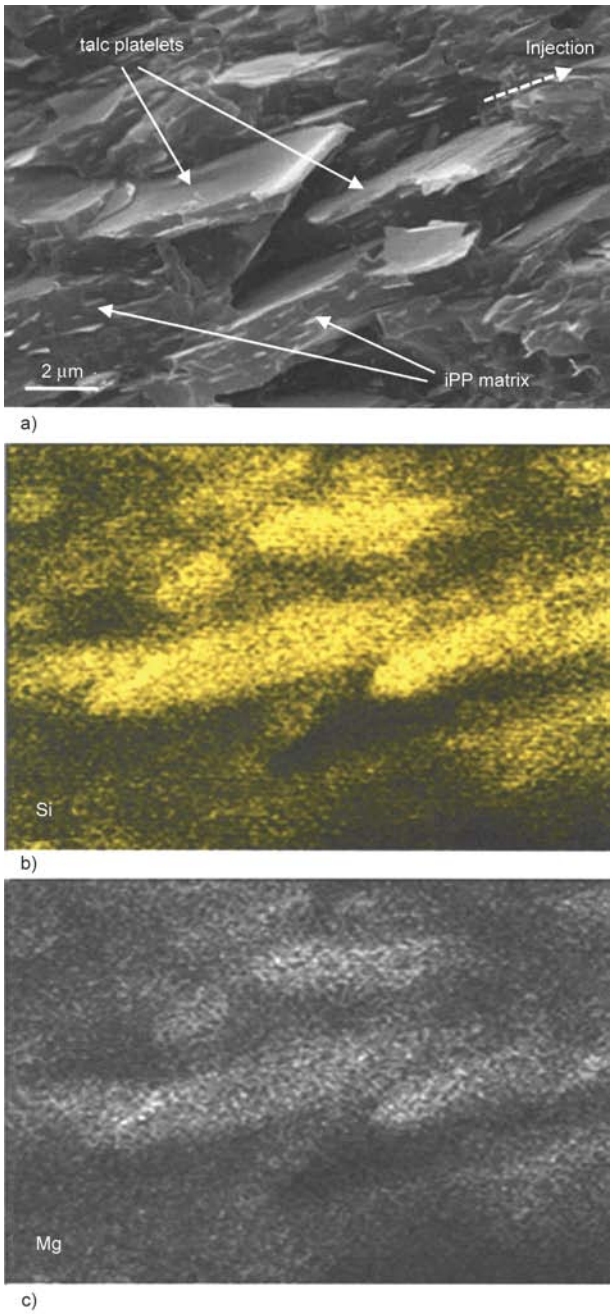

Figure 7. SEM image (a) from the center of a cross-section of an injection-molded iPP/30% μ-talc and corresponding EDX images of the Si (b) and Mg (c) atomic distributions in the talc platelets

3.3. Crystallinity versus talc loading and cooling rate

Crystallinity has been determined for the 49 samples of the series, i.e. pure iPP together with 6 composites of different μ-talc loadings crystallized at 7 different cooling rates. All the XC data are reported in Table 2. An examination of these data reveals that X_C decreases with increasing C_R for a given F_R. Less time is afforded to the iPP matrix for crystallizing in its optimal temperature range ($110 < T_c^{max} < 130\,°C$, see Figure 3) when C_R is high. Conversely, X_C increases with F_R at a given C_R since higher F_R provides more particle surface for iPP nucleation. However, it can be seen in Table 2 that the X_C evolution is different if considering the sensitivity to C_R of the various materials. At low cooling rate, i.e. $C_R = 2\,°C/min$, the rather high X_C data increase quickly in a first step with increasing F_R then tend to level off for $F_R > 7\%$. In contrast, at high C_R, i.e. $C_R = 40\,°C/min$, the significantly lower X_C values display a roughly linear increase with F_R without leveling off. As proposed in the previous subsection, and borrowing from several reports regarding polymer-clay nanocomposites, this finding may be attributed to a physical barrier effect or steric hindrance of the μ-talc platelets to the growth of iPP crystal lamellae at high F_R and low C_R when crystallinity is high. The barrier effect of the μ-talc platelets would be less effective at high C_R due to less steric hindrance to the crystal growth when crystallinity is low.

For the sake of comparison, crystallinity data for S-talc composites are reported in Table 2 as a function of C_R, for two F_R values 3 and 20%. Though differences are not dramatic between the two kinds of composites, the X_C data are systematically higher for the μ-talc composites, irrespective of C_R and F_R, which confirms the better nucleating effect of μ-talc due to higher specific area.

3.4. Statistical analysis and modeling

The statistical analysis of the response to any kind of experiment is a useful tool for probing the incidence

of the various experimental or entry parameters on the response. A numerical relation can be established between the response and the entry parameters [16, 43–45]. The numerical values of the response can be then compared to the experimental data. The Design Expert 8 software was used in this study in combination with the ANOVA variance analysis.

The numerical expression for the crystallinity as a function of the experimental parameters derived from Equation (2) is given by Equation (4):

$$X_C = +53.77850 - 0.42080 \cdot C_R + 1.02231 \cdot F_R + 3.89570 \cdot 10^{-3} \cdot C_R \cdot F_R - 0.015739 \cdot C_R^2 - 0.047613 \cdot F_R^2 - 3.31598 \cdot 10^{-4} \cdot C_R^2 \cdot F_R + 3.35287 \cdot 10^{-4} \cdot C_R \cdot F_R^2 + 3.52478 \cdot 10^{-4} \cdot C_R^3 + 7.63055 \cdot 10^{-4} \cdot F_R^3 \quad (4)$$

with a regression coefficient $R^2 = 98.5$.

The residuals reported in Figure 8 for the 49 experiments or runs do not exceed 2.5% of the X_C value and are randomly distributed about the X_C value of every run. Moreover, Figure 9 shows that the residues fairly obey a normal law distribution.

On Figure 10 is shown the 2D mapping of the predicted crystallinity as a function of C_R and F_R together with the experimental data. The blue to red color range accounts for the full crystallinity range of the present study $34.5\% < X_C < 62.2\%$. The iso-color domains stand for the C_R/F_R coupling that results in iso-crystallinity.

Figure 11 is a 3D diagram of X_C versus C_R and F_R. This figure shows that, in the experimentally accessible ranges of C_R and F_R, X_C is much more sensitive to C_R than to F_R. Indeed, in the high X_C domain, the red zone extends more along the F_R range than along the C_R range. Similarly, in the low X_C domain,

Table 2. Crystallinity data from experimental plan (μ and S superscripts hold for μ-talc and S-talc composites)

Run	C_R [°C/min]	F_R [%]	X_C^{μ} [%]	X_C^{S} [%]
1	2	0	53.8	–
2	2	3	54.3	54.0
3	2	5	55.0	–
4	2	7	59.2	–
5	2	10	59.6	–
6	2	20	61.2	58.2
7	2	30	62.2	–
8	*5*	*0*	*51.4*	–
9	*5*	*3*	*53.7*	52.7
10	*5*	*5*	*54.2*	–
11	*5*	*7*	*56.7*	–
12	*5*	*10*	*59.4*	–
13	*5*	*20*	*61.0*	(58.5)
14	*5*	*30*	*61.9*	–
15	10	0	49.2	–
16	10	3	51.5	50.5
17	10	5	53.2	–
18	10	7	53.4	–
19	10	10	53.5	–
20	10	20	54.9	53.5
21	10	30	58.8	–
22	*15*	*0*	*44.5*	–
23	*15*	*3*	*47.4*	46.1
24	*15*	*5*	*49.8*	–
25	*15*	*7*	*50.2*	–
26	*15*	*10*	*53.0*	–
27	*15*	*20*	*53.5*	52.8
28	*15*	*30*	*57.2*	–
29	20	0	43.9	–
30	20	3	44.0	43.6
31	20	5	45.1	–
32	20	7	46.9	–
33	20	10	48.4	–
34	20	20	52.2	48.2
35	20	30	55.9	–
36	*30*	*0*	*35.2*	–
37	*30*	*3*	*37.3*	36.4
38	*30*	*5*	*38.5*	–
39	*30*	*7*	*42.4*	–
40	*30*	*10*	*42.6*	–
41	*30*	*20*	*43.9*	42.1
42	*30*	*30*	*48.8*	–
43	40	0	34.5	–
44	40	3	36.6	35.7
45	40	5	37.0	–
46	40	7	37.6	–
47	40	10	37.9	–
48	40	20	39.3	37.8
49	40	30	43.4	–

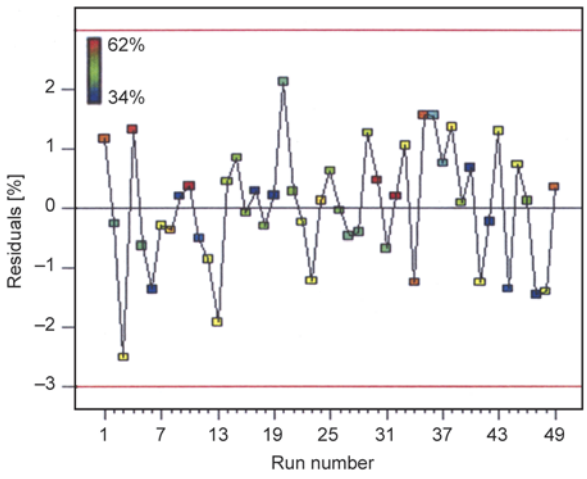

Figure 8. Residuals for the crystallinity ratio from the statistical analysis (same Run N° as in Table 2; symbol color holds for the crystallinity ratio)

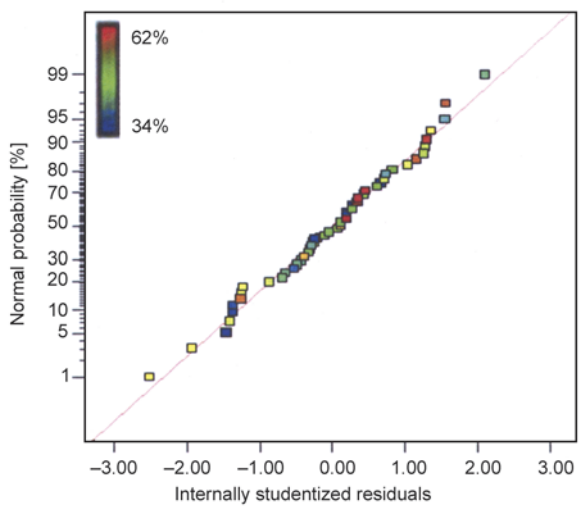

Figure 9. Residual distribution of the crystallinity ratio (same color scale as in Figure 8)

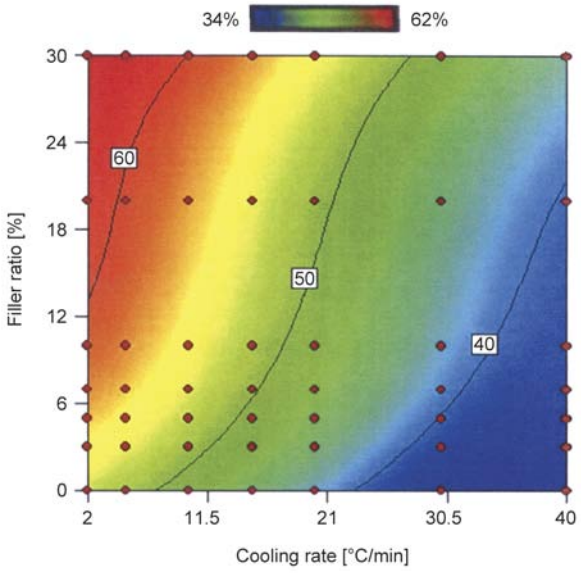

Figure 10. 2D mapping of the predicted crystallinity ratio versus C_R and F_R (the full lines stand for iso-crystallinity curves; symbols hold for experimental data)

the blue zone extends more along the F_R range than along the C_R range.

Figure 11 also reveals that at high talc loading, i.e. $F_R \geq 20\%$, X_C tends to saturate at its maximum value for $C_R \leq 5\,°C/min$ as judged from the nearly zero slope of the predicted X_C variation versus F_R. Therefore, one cannot expect $X_C > 62.2\%$ even with μ-talc loadings $F_R \gg 30\%$. Similarly, the very low slope of the predicted X_C variation with C_R at low C_R values suggests that one may hardly expect $X_C > 62.2\%$ even if using $C_R \ll 2\,°C/min$.

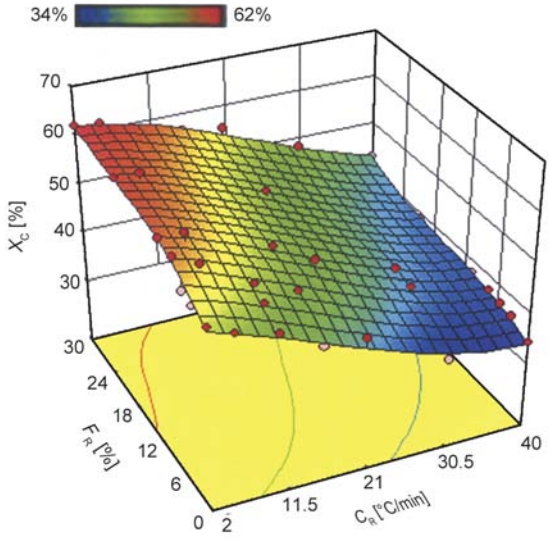

Figure 11. 3D surface plot of X_C versus C_R and F_R

4. Conclusions

The thermal, microscopic and crystallographic study of iPP/μ-talc composites showed that μ-talc is actually a nucleating agent of the iPP matrix, irrespective of potential shear-induced effects due to processing. This nucleating effect is somewhat more pronounced than for standard talc having a surface area about 3 times lower than that of μ-talc. The combination of this nucleating effect with the injection-driven orientation of the platelets generates a strong texturing of the samples.

The use of ANOVA analysis of a set of experimental data of crystallinity (X_C) for various values of the cooling rate (C_R) and various values of the filler content (F_R) allowed to draw a numerical 3D surface $X_C = f(C_R, F_R)$ for predicting the crystallinity of the composites for any cooling rate and filler content with a confidence level greater than of 95%. This 3D surface clearly shows the greater X_C sensitivity to C_R compared to F_R. It also clearly showed the X_C saturation at low cooling rates ($C_R \leq 5\,°C/min$) and high talc loading ($F_R \geq 20\%$). Moreover, it appears that the strong sensitivity of iPP matrix to F_R does not shortcut the intrinsic sensitivity of iPP to C_R, the two effects being clearly additive.

Acknowledgements

The authors are indebted to Multibase/Dow Corning (Saint-Laurent du Pont, France) for the supply of the composites and the characteristics of the components, and to Dr. Patrick Prele from Multibase for fruitful discussions.

References

[1] Karger-Kocsis J.: Polypropylene: Structure, blends and composites; Vol.3: Composites. Chapman and Hall, London (1994).

[2] Karian H. G.: Handbook of polypropylene and polypropylene composites. Marcel Dekker, New York (2003).

[3] McGenity P. M., Hooper J. J., Paynter C. D., Riley A. M., Nutbeem C., Elton N. J., Adams J. M.: Nucleation and crystallization of polypropylene by mineral fillers: Relationship to impact strength. Polymer, **33**, 5215–5224 (1992).
DOI: 10.1016/0032-3861(92)90804-6

[4] Wilbrink M. W. L., Argon A. S., Cohen R. E., Weinberg M.: Toughenability of Nylon-6 with $CaCO_3$ filler particles: New findings and general principles. Polymer, **42**, 10155–10180 (2001).
DOI: 10.1016/S0032-3861(01)00548-1

[5] Thio Y. S., Argon A. S., Cohen R. E., Weinberg M.: Toughening of isotactic polypropylene with $CaCO_3$ particles. Polymer, **43**, 3661–3674 (2002).
DOI: 10.1016/S0032-3861(02)00193-3

[6] Zuiderduin W. C. J., Westzaan C., Huétink J., Gaymans R. J.: Toughening of polypropylene with calcium carbonate particles. Polymer, **44**, 261–275 (2003).
DOI: 10.1016/S0032-3861(02)00769-3

[7] Thio Y. S., Argon A. S., Cohen R. E.: Role of interfacial adhesion strength on toughening polypropylene with rigid particles. Polymer, **45**, 3139–3147 (2004).
DOI: 10.1016/j.polymer.2004.02.064

[8] Hadal R. S., Dasari A., Rohrmann J., Misra R. D. K.: Effect of wollastonite and talc on the micromechanisms of tensile deformation in polypropylene composites. Materials Science and Engineering: A, **372**, 296–315 (2004).
DOI: 10.1016/j.msea.2004.01.003

[9] Alexandre M., Dubois P.: Polymer-layered silicate nanocomposites: Preparation, properties and uses of a new class of materials. Materials Science and Engineering R: Reports, **28**, 1–63 (2000).
DOI: 10.1016/S0927-796X(00)00012-7

[10] Ray S. S., Okamoto M.: Polymer/layered silicate nanocomposites: A review from preparation to processing. Progress in Polymer Science, **28**, 1539–1641 (2003).
DOI: 10.1016/j.progpolymsci.2003.08.002

[11] Százdi L., Pozsgay A., Pukánszky B.: Factors and processes influencing the reinforcing effect of layered silicates in polymer nanocomposites. European Polymer Journal, **43**, 345–359 (2007).
DOI: 10.1016/j.eurpolymj.2006.11.005

[12] Bourbigot S., Duquesne S.: Fire retardant polymers: Recent developments and opportunities. Journal of Materials Chemistry, **17**, 2283–2300 (2007).
DOI: 10.1039/b702511d

[13] Naiki M., Fukui Y., Matsumura T., Nomura T., Matsuda M.: The effect of talc on the crystallization of isotactic polypropylene. Journal of Applied Polymer Science, **79**, 1693–1703 (2001).
DOI: 10.1002/1097-4628(20010228)79:9<1693::AID-APP190>3.0.CO;2-P

[14] Obata Y., Sumitomo T., Ijitsu T., Matsuda M., Nomura T.: The effect of talc on the crystal orientation in polypropylene/ethylene-propylene rubber/talc polymer blends in injection molding. Polymer Engineering and Science, **41**, 408–416 (2001).
DOI: 10.1002/pen.10738

[15] Zhou Y., Mallick P.: Effects of temperature and strain rate on the tensile behavior of unfilled and talc-filled polypropylene. Part I: Experiments. Polymer Engineering and Science, **42**, 2449–2460 (2002).
DOI: 10.1002/pen.11131

[16] Barbosa C. N., Simoes R., Franzen M., Viana J. C.: Thermomechanical environment characterisation in injection moulding and its relation to the mechanical properties of talc-filled polypropylene. Journal of Materials Science, **48**, 2597–2607 (2013).
DOI: 10.1007/s10853-012-7052-4

[17] Prêle P., von Tschammer A., Crépin-Leblond J.: An innovative masterbatch concept for automotive plastics using an extremely high aspect ratio talc. in 'Proceedings of the 22nd World Automotive Congress: Plastics in Motion, Roma, Italy' p.25 (2007).

[18] Leong Y. W., Abu Bakar M. B., Ishak Z. A. M., Ariffin A., Pukánszky B.: Comparison of the mechanical properties and interfacial interactions between talc, kaolin, and calcium carbonate filled polypropylene composites. Journal of Applied Polymer Science, **91**, 3315–3326 (2004).
DOI: 10.1002/app.13542

[19] Menczel J., Varga J.: Influence of nucleating agents on crystallization of polypropylene I. Talc as a nucleating agent. Journal of Thermal Analysis, **28**, 161–174 (1983).
DOI: 10.1007/BF02105288

[20] Rybnikář F.: Orientation in composite of polypropylene and talc. Journal of Applied Polymer Science, **38**, 1479–1490 (1989).
DOI: 10.1002/app.1989.070380806

[21] de Medeiros E. S., Tocchetto R. S., de Carvalho L. H., Santos I. M. G., Souza A. G.: Nucleating effect and dynamic crystallization of a poly(propylene)/talc system. Journal of Thermal Analysis and Calorimetry, **66**, 523–531 (2001).
DOI: 10.1023/A:1013121102536

[22] Kocic N., Kretschmer K., Bastian M., Heidemeyer P.: The influence of talc as a nucleation agent on the non-isothermal crystallization and morphology of isotactic polypropylene: The application of the Lauritzen–Hoffmann, Avrami, and Ozawa theories. Journal of Applied Polymer Science, **126**, 1207–1217 (2012).
DOI: 10.1002/app.36880

[23] Choi W. J., Kim S. C.: Effects of talc orientation and non-isothermal crystallization rate on crystal orientation of polypropylene in injection-molded polypropylene/ethylene–propylene rubber/talc blends. Polymer, **45**, 2393–2401 (2004). DOI: 10.1016/j.polymer.2004.01.058

[24] Fujiyama M., Wakino T.: Crystal orientation in injection molding of talc-filled polypropylene. Journal of Applied Polymer Science, **42**, 9–20 (1991). DOI: 10.1002/app.1991.070420103

[25] Fujiyama M.: Crystal orientation in injection moldings of talc-filled polyolefins. International Polymer Processing, **13**, 284–290 (1998). DOI: 10.3139/217.980284

[26] Ferrage E., Martin F., Boudet A., Petit S., Fourty G., Jouffret F., Micoud P., de Parseval P., Salvi S., Bourgerette C., Ferret J., Saint-Gerard Y., Buratto S., Fortune J. P.: Talc as nucleating agent of polypropylene: Morphology induced by lamellar particles addition and interface mineral-matrix modelization. Journal of Materials Science, **37**, 1561–1573 (2002). DOI: 10.1023/A:1014929121367

[27] Branciforti M. C., Oliveira C. A., de Sousa J. A.: Molecular orientation, crystallinity, and flexural modulus correlations in injection molded polypropylene/talc composites. Polymers for Advanced Technologies, **21**, 322–330 (2010). DOI: 10.1002/pat.1431

[28] Maiti S. N., Sharma K. K.: Studies on polypropylene composites filled with talc particles. Journal of Materials Science, **27**, 4605–4613 (1992). DOI: 10.1007/BF01165994

[29] Liu Z., Gilbert M.: Structure and properties of talc-filled polypropylene: Effect of phosphate coating. Journal of Applied Polymer Science, **59**, 1087–1098 (1996). DOI: 10.1002/(SICI)1097-4628(19960214)59:7<1087::AID-APP5>3.3.CO;2-S

[30] Huneault M. A., Godfroy P. G., Lafleur P. G.: Performance of talc/ethylene-octene copolymer/polypropylene blends. Polymer Engineering and Science, **39**, 1130–1138 (1999). DOI: 10.1002/pen.11500

[31] Zhou X-P., Xie X-L., Yu Z-Z., Mai Y-W.: Intercalated structure of polypropylene/*in situ* polymerization-modified talc composites *via* melt compounding. Polymer, **48**, 3555–3564 (2007). DOI: 10.1016/j.polymer.2007.04.033

[32] Castillo L. A., Barbosa S. E., Capiati N. J.: Surface-modified talc particles by acetoxy groups grafting: Effects on mechanical properties of polypropylene/talc composites. Polymer Engineering and Science, **53**, 89–95 (2013). DOI: 10.1002/pen.23243

[33] Fiorentino B., Fulchiron R., Duchet-Rumeau J., Bounor-Legaré V., Majesté J-C.: Controlled shear-induced molecular orientation and crystallization in polypropylene/talc microcomposites – Effects of the talc nature. Polymer, **54**, 2764–2775 (2013). DOI: 10.1016/j.polymer.2013.03.057

[34] Fiorentino B., Fulchiron R., Bounor-Legare V., Majesté J-C., Leblond J. C., Duchet-Rumeau J.: Chemical modification routes of synthetic talc: influence on its nucleating power and on its dispersion state. Applied Clay Science, **110**, 107–118 (2015). DOI: 10.1016/j.clay.2015.02.026

[35] Rotzinger B.: Talc-filled PP: A new concept to maintain long term heat stability. Polymer Degradation and Stability, **91**, 2884–2887 (2006). DOI: 10.1016/j.polymdegradstab.2006.09.008

[36] Duquesne S., Samyn F., Bourbigot S., Amigouet P., Jouffret F., Shen K.: Influence of talc on the fire retardant properties of highly filled intumescent polypropylene composites. Polymers for Advanced Technologies, **19**, 620–627 (2008). DOI: 10.1002/pat.1127

[37] Frihi D., Masenelli-Varlot K., Vigier G., Satha H.: Mixed percolating network and mechanical properties of polypropylene/talc composites. Journal of Applied Polymer Science, **114**, 3097–3105 (2009). DOI: 10.1002/app.30890

[38] Paul D. R., Bucknall C. B.: Polymer blends, Vol. 2: Performance. Wiley, New York (2000).

[39] van der Wal A., Mulder J. J., Gaymans R. J.: Fracture of polypropylene: The effect of crystallinity. Polymer, **39**, 5477–5481 (1998). DOI: 10.1016/S0032-3861(97)10279-8

[40] Piccarolo S.: Morphological changes in isotactic polypropylene as a function of cooling rate. Journal of Macromolecular Science Part B: Physics, **31**, 501–511 (1992). DOI: 10.1080/00222349208215467

[41] van Drongelen M., van Erp T. B., Peters G. W. M.: Quantification of non-isothermal, multi-phase crystallization of isotactic polypropylene: The influence of cooling rate and pressure. Polymer, **53**, 4758–4769 (2012). DOI: 10.1016/j.polymer.2012.08.003

[42] Gahleitner M., Bernreitner K., Neißl W.: Correlations between rheological and mechanical properties of mineral filled polypropylene compounds. Journal of Applied Polymer Science, **53**, 283–289 (1994). DOI: 10.1002/app.1994.070530304

[43] Wunderlich B.: Macromolecular physics, Vol.1: Crystal structure, morphology and defects. Academic Press, New York (1973).

[44] da Costa M. H., Ramos D. V., de Oliveira G. M.: Degradation of polypropylene (PP) during multiple extrusions: Thermal analysis, mechanical properties and analysis of variance. Polymer Testing, **26**, 676–684 (2007). DOI: 10.1016/j.polymertesting.2007.04.003

[45] Gu R., Kokta B. V.: Maximization of the mechanical properties of birch-polypropylene composites with additives by statistical experimental design. Journal of Thermoplastic Composite Materials, **23**, 239–263 (2010).
DOI: 10.1177/0892705708103402

[46] Hejazi I., Sharif F., Garmabi H.: Effect of material and processing parameters on mechanical properties of polypropylene/ethylene–propylene–diene–monomer/clay nanocomposites. Materials and Design, **32**, 3803–3809 (2011).
DOI: 10.1016/j.matdes.2011.03.017

[47] Raja R. S., Manisekar K., Manikandan V.: Study on mechanical properties of fly ash impregnated glass fiber reinforced polymer composites using mixture design analysis. Materials and Design, **55**, 499–508 (2014).
DOI: 10.1016/j.matdes.2013.10.026

[48] Chabert B., Chauchard J., Cinquin J.: DSC study of the non-isothermal crystallization of the PA66 matrix in glass fiber composites (in French). Makromolekulare Chemie. Macromolecular Symposia, **9**, 99–111 (1987).
DOI: 10.1002/masy.19870090112

[49] Valentini L., Biagiotti J., Kenny J. M., Santucci S.: Morphological characterization of single-walled carbon nanotubes-PP composites. Composites Science and Technology, **63**, 1149–1153 (2003).
DOI: 10.1016/S0266-3538(03)00036-8

[50] Fornes T. D., Paul D. R.: Crystallization behavior of nylon 6 nanocomposites. Polymer, **44**, 3945–3961 (2003).
DOI: 10.1016/S0032-3861(03)00344-6

[51] Lincoln D. M., Vaia R. A., Krishnamoorti R.: Isothermal crystallization of nylon-6/montmorillonite nanocomposites. Macromolecules, **37**, 4554–4561 (2004).
DOI: 10.1021/ma049768k

[52] Yang Z., Huang S., Liu T.: Crystallization behavior of polyamide 11/multiwalled carbon nanotube composites. Journal of Applied Polymer Science, **122**, 551–560 (2011).
DOI: 10.1002/app.34118

[53] Zare Y., Garmabi H.: Nonisothermal crystallization and melting behavior of PP/nanoclay/$CaCO_3$ ternary nanocomposite. Journal of Applied Polymer Science, **124**, 1225–1233 (2012).
DOI: 10.1002/app.35134

[54] Deshmukh G. S., Peshwe D. R., Pathak S. U., Ekhe J. D.: Nonisothermal crystallization kinetics and melting behavior of poly(butylene terephthalate) and calcium carbonate nanocomposites. Thermochimica Acta, **606**, 66–76 (2015).
DOI: 10.1016/j.tca.2015.03.008

[55] Thomason J. L.: The influence of fibre length and concentration on the properties of glass fibre reinforced polypropylene. 6. The properties of injection moulded long fibre PP at high fibre content. Composites Part A: Applied Science and Manufacturing, **36**, 995–1003 (2005).
DOI: 10.1016/j.compositesa.2004.11.004

[56] Thomason J. L.: Structure–property relationships in glass-reinforced polyamide, Part 1: The effects of fiber content. Polymer Composites, **27**, 552–562 (2006).
DOI: 10.1002/pc.20226

[57] Miri V., Elkoun S., Peurton F., Vanmansart C., Lefebvre J-M., Krawczak P., Seguela R.: Crystallization kinetics and crystal structure of nylon6-clay nanocomposites: Combined effects of thermomechanical history, clay content, and cooling conditions. Macromolecules, **41**, 9234–9244 (2008).
DOI: 10.1021/ma801804y

[58] Yalcin B., Valladares D., Cakmak M.: Amplification effect of platelet type nanoparticles on the orientation behavior of injection molded nylon 6 composites. Polymer, **44**, 6913–6925 (2003).
DOI: 10.1016/j.polymer.2003.07.010

[59] Thomason J. L., van Rooyen A. A.: Transcrystallized interphase in thermoplastic composites. Part II Influence of interfacial stress, cooling rate, fibre properties and polymer molecular weight. Journal of Materials Science, **27**, 897–907 (1992).
DOI: 10.1007/BF01197639

eXPRESS Polymer Letters Vol.10, No.3 (2016) 248–258
Available online at www.expresspolymlett.com
DOI: 10.3144/expresspolymlett.2016.23

Synthesis and characterization of high performance superabsorbent hydrogels using *bis*[2-(methacryloyloxy)ethyl] phosphate as crosslinker

*A. A. L. Gonçalves, A. C. Fonseca, I. G. P. Fabela, J. F. J. Coelho, A. C. Serra**

CEMUC, Department of Chemical Engineering, University of Coimbra, Rua Sílvio Lima-Pólo II, 3030-290, Coimbra, Portugal

Received 13 August 2015; accepted in revised form 13 October 2015

Abstract. Various superabsorbent polymers (SAPs) were synthesized by free radical copolymerization at 70 °C using acrylic acid (AA), potassium acrylate (KA), *N*-isopropyl acrylamide (NIPAM) and sulfopropyl methacrylate potassium salt (SPM) as monomers, *bis*[2-(methacryloyloxy)ethyl] phosphate (BMEP) as crosslinker and potassium persulfate (KPS) as initiator. The optimization of the synthesis led to the preparation of a SAP with very high water absorption ability, with a maximum swelling of 2618 g water/g dry hydrogel. The most promising SAP was fully characterized and the absorption capacities were studied at different pH and ionic strengths. When this SAP was mixed with soil, the mixture was able to lose water more slowly. Also, this material revealed high loading capacity and showed good releasing profiles using urea as model fertilizer. Due to these advantageous properties, the synthesized SAP can be used in agricultural applications.

Keywords: *polymer gels, superabsorbent, bis[2-(methacryloyloxy)ethyl] phosphate, agriculture*

1. Introduction

Superabsorbent polymers (SAPs) are a class of hydrogel like materials with increasing interest in agriculture or in polluted lands [1]. These 3D structures can absorb large amounts of water or aqueous fluids in relatively short periods of time, as compared to conventional hydrogels, and generally absorb an amount of water that can reach 1000 times (or more) their dry weight material [2, 3]. Hydrogels can be applied in a wide range of products and areas (e.g., hygiene, biomedical, pharmaceutical, agriculture) due to their unique properties such as hydrophilicity, biocompatibility and especially high absorption capacity and swelling/de-swelling behaviour [3–5]. Particularly, SAPs appear as materials with promising characteristics to improve the use of water in soils. These materials can maximize water availability and increase crop production without adverse consequences for the natural resources and environment. It is known that the largest consumers of fresh water are the agricultural activities, specifically intensively irrigated agriculture, which currently consumes over 85% of the available water. The importance of this comes from the fact that a very high fraction of produced food comes from irrigated lands [6, 7]. Also, the increased water demand in several sectors like industry and domestic, among others, associated to the irregular distribution due to climatic and environmental changes and the practice of some inefficient methods, demands an urgent development of effective technologies to rationalize the use of water. Another important feature that can be explored in SAPs is their capacity to release agrochemicals in a controlled way. This characteristic proves to be quite useful and advantageous for a precise supply of nutrients to plants. Among other

*Corresponding author, e-mail: aserra@eq.uc.pt

aspects, it allows the correction of environmental deficiencies, avoiding additional costs due to excessive fertilization and agrochemical wastes [8], reducing water runoff and erosion, enabling the recovery of desertified and slightly fertile areas and others [7, 9].

The present work involved the synthesis of hydrogels with extremely high swelling properties and a promising potential for use in agricultural applications, either as water reservoirs or as agrochemical release systems. The synthesis of these SAPs was carried out using a combination of monomers, such as AA, KA, NIPAM and SPM. To the best of our knowledge, BMEP has never been used as a crosslinker for the synthesis of hydrogels. The swelling properties of all SAPs were evaluated. For the most promising SAP, the ability to incorporate and release urea (used as fertilizer model compound) and the improvements in water retention capacity by soil were studied.

2. Experimental section

2.1. Materials

Acrylic acid (AA) (99%), 3-sulfopropyl methacrylate potassium salt (98%) (SPM), *bis*[2-(methacryloyloxy)ethyl] phosphate (99.9%) (BMEP), potassium hydroxide (KOH) (90%), hydrochloric acid (HCl) (37%) were purchased from Sigma-Aldrich (St Louis, USA); N-isopropyl acrylamide (98%) (NIPAM) was purchased from TCI Europe (Zwijndrecht, Belgium); potassium persulfate (KPS) (99%) was acquired from Riedel-de-Haën (Seelze, Germany). Sodium hydroxide (NaOH) (97%) was obtained from Panreac Química (Barcelona, Spain). Urea was acquired from VWR International, Ltd (Carnaxide, Portugal). Potassium acrylate (KA) was prepared by neutralization of acrylic acid with the corresponding amount of base (KOH). All the reagents, solvents and other materials were used as received without further purification.

2.2. SAP synthesis

The synthesis of the SAPs was performed in a 150 mL glass reactor, equipped with a Liebig condenser and a mechanical stirrer. The reagents, AA, KA, SPM, NIPAM, BMEP and KPS were added to the reactor with 40 mL of distilled water. The mixture was heated at 70 °C until the gelification of the mixture occurred (generally between 60 and 75 minutes). After the polymerization, the SAP samples were washed with cold methanol to remove unreacted monomers, cut into small pieces and dried at 50 °C for 24 h. Next, the dry SAPs were purified by Soxhlet extraction using acetone-methanol (1:1 v/v), at 50 °C for 24 h, powdered, dried until constant weight and stored. For all reactions, the conversion was calculated gravimetrically and was close to 95%.

2.3. Instrumentation

The Fourier Transform Infrared (FTIR) spectra were recorded on a FTIR-spectrophotometer (Jasco) with 4 cm^{-1} resolution. Attenuated Total Reflection (ATR) mode was used. Scanning electron microscope (SEM) (MEV)/EDS, JEOL, model JSM-5310, at an accelerating voltage of 10 kV was used for SEM analysis. In this especific case, for the analysis of porosity, the SAP samples were first immersed in distilled water until reaching equilibrium swelling, placed in liquid nitrogen, then freeze dried and analysed by SEM. TGA was perfomed in a SDT Q600 equipment (TA instruments), at a heating rate of 10 °C/min, for temperatures ranging from 30 to 600 °C, under a constant nitrogen flow.

2.4. Molecular weight between crosslinks (M_c)

The average molecular weight between crosslinks (M_c) of the hydrogels was calculated from the volume fraction of polymer in the swollen polymer. The polymer volume fraction (v) of the swollen polymer was determined taking into account the swelling capacity of the hydrogels in distilled water and the density of the polymer determined in a pycnometer using heptane, according to Equation (1) [10, 11]:

$$\nu = \frac{W_0 \cdot \rho_w}{W \cdot \rho - W_0 \cdot (\rho - \rho_w)} \quad (1)$$

where W is weight of swollen polymer, W_0 is the initial weight of the sample and ρ_w and ρ are the density of water and the density of the dry hydrogel.

The average molecular weight between crosslinks (M_c) can be estimated using Equation (2) developed by Flory and Rehner [12]:

$$M_c = -\frac{\rho \cdot V_1 \cdot \nu^{1/3}}{\frac{K \cdot \nu^2}{2 + \ln(1 - \nu) + \nu}} \quad (2)$$

where V_1 is the molar volume of water (18.062 cm^3/mol) and $K = 2 \cdot X \cdot V_1/(R \cdot T)$ [12] is the polymer-solvent interaction parameter and indicates the change of interaction energy when solvent and

polymer are mixed together. The value of χ was calculated using Equation (3):

$$\chi \cong \frac{1}{2} + \frac{\nu}{3} \tag{3}$$

2.5. Determination of crosslinking density (q)

The determination of the crosslinking density was done through Equation (4) [13]:

$$q = \frac{M_c}{M_r} \tag{4}$$

where M_r, the pondered molar mass of the repeating unit was determined through the Equation (5) [13], where M_{NIPAM}, M_{KA}, M_{SPM}, M_{AA} are the molar masses and m_{NIPAAm}, m_{KA}, m_{SPM} and m_{AA} are the amount of the used monomers.

$$M_r = \frac{M_{AA} \cdot m_{AA} + M_{NIPAM} \cdot m_{NIPAM} + M_{KA} \cdot m_{KA} + M_{SPM} \cdot m_{SPM}}{m_{AA} + m_{NIPAM} + m_{KA} + m_{SPM}} \tag{5}$$

2.6. Gel content

To determine the gel content of the SAPs, hydrogel samples were cut and dried at 50 °C for 24 h. The dried hydrogels were then extracted in a Soxhlet using acetone-methanol (1:1 v/v) at 50 °C for 24 h. The portion of the hydrogel remaining after extraction, corresponding to the insoluble and crosslinked part, was dried and weighed. The gel content was calculated according to Equation (6) [14]:

$$\text{Gel content [\%]} = \frac{W_1}{W_0} \cdot 100 \tag{6}$$

where W_1 is the weight of the insoluble part of the sample (after the extracion) and W_0 is the weight of dried hydrogel before extraction.

2.7. Swelling Properties

The absorption capacity of the synthesized SAPs was measured both in distilled water and in saline solutions (0.3, 0.6, 0.9 and 1.5 wt% of NaCl), at various pHs (3, 5, 7, 9, 11) using the tea bag method [3].

For the tea bag method, an accurately weighed powdered SAP sample (0.005 and 0.01 g) was placed into a tea-bag (acrylic/polyester gauze with fine meshes) and the bag was immersed in an excess amount of water or of another solution (approximately 1 liter) at room temperature. After a certain period of time, the bag was removed from the solution, the excess of water was removed superficially with tissue paper and the bag was weighted [3]. This process was repeated several times until the swelling equilibrium was reached (approximately 24 hours), i.e. until the bag presented a constant weight. The swelling profiles and the absorption capacity (AC) of the hydrogel in units of amount [g] of water absorbed per gram of SAP, can be defined using Equation (7):

$$\text{AC} = \frac{W_s - W_d}{W_d} \tag{7}$$

where W_s and W_d are the weights of the swollen hydrogel and the dry sample, respectively. The final absorption capacity was calculated by taking an average of three independent measurements.

2.8. Water retention capacity of the soil with SAP

To study the water retention capacity of the soil treated with the SAP, different amounts of hydrogel (0.5, 1 and 2 wt% relative to the soil weight) were mixed with 40 g of sandy soil. Subsequently, the mixtures were uniformly irrigated with a certain amount of distilled water (20 g) and exposed to air at a room temperature. For each mixture, three experiments were performed. A control experiment was also performed using soil without addition of hydrogel [15, 16]. These mixtures were weighed at certain intervals of time and the weight loss by water evaporation was registered. To determine the water retention (WR) percentage of the soil with or without the hydrogel, Equation (8) was used [15].

$$\text{WR [\%]} = \frac{W_0 - W_t}{W_0} \cdot 100 \tag{8}$$

where W_0 and W_t are the initial mixture weight, and the mixture weight at a certain time, respectively.

2.9. Urea loading and release

To perform the urea loading tests, samples of dry hydrogel (0.005 g) were immersed in urea solutions with different concentrations (5, 10, 15 and 20 g/L) for approximately 24 hours (until reaching the maximum swelling) [11, 15]. Subsequently, the swollen and loaded hydrogels were oven dried at 50 °C to constant weight. Knowing the weights of unloaded

(M_0) and loaded dry hydrogels (M_l) it was possible to calculate the percentage of loading of urea using Equation (9) [14]:

$$\text{Loading [\%]} = \frac{M_l - M_0}{M_0} \cdot 100 \quad (9)$$

For each concentration of urea three experiments were performed and an average of these values was used to carried out the calculations.

To investigate the ability of the SAPs to release urea, three samples of urea loaded hydrogels (obtained from the immersion in a urea solution with a concentration of 20 g/L) with weights between 0.120 and 0.170 grams were placed in 500 mL of distilled water at room temperature. At various times, 20 mL of this solution was collected for a glass container and the content was freeze dried. The amount of urea was determined gravimetrically, comparing the weight of the container before and after this process and taking into account a blank experiment with only 20 mL of water. The percentage of urea released was calculated using the Equation (10) [11]:

$$\text{\% of urea released} = (\Delta W)_n \cdot \frac{500-(n-1)\cdot 20}{20} + \sum_{i=1}^{n-1} \frac{(\Delta W)_i}{W_u} \quad (10)$$

where $(\Delta W)_i$ is the weight of urea released from the 20 mL sample, W_u is the amount of urea loaded in SAP, n indicates the number of urea release measurements at various time intervals in a single experiment, $(\Delta W)_n$ is the weight of urea released in the measurement n.

3. Results and discussion

3.1. Synthesis and characterization of the SAPs

The present work describes the synthesis of superabsorbant hydrogels from SPM, AA, NIPAM and KA monomers, which are the common monomers used in the preparation of SAPs, but introducing BMEP, a generally used flame retardant monomer [17], as the difunctional crosslinker. The presence of phosphate groups could bring to the gel higher biocompatibility and biodegradability. SPM was used to increase the osmotic pressure between the interior and the exterior of the hydrogel (due to the difference in the concentration of the K^+ counterion), as a mean to improve the water absorption capacity of the ionic hydrogel [18].The use of this crosslinker in combination with the above refered monomers has never been reported in hydrogel synthesis. NIPAM is known to increase the rate of decomposition of persulfates, and because of that it was used in all the hydrogels prepared in this work [11, 19, 20]. The different reaction conditions for SAP synthesis (SAP1 to SAP10) and the physical properties of the obtained products are presented in Table 1.

3.2. Mechanism of polymerization

The synthesis of SAPs occurred through free radical polymerization as shown in Figure 1. The initiator decomposed thermally to produce sulphate radicals that add to monomers, propagating a chain reaction that produces the crosslinked polymer (SAP) [21].

3.3. Swelling properties

The results for the water absorption capacity of the different synthesized SAPs (Table 1) shows that these

Table 1. Monomer feed composition, average molecular weight between crosslinks (M_c), crosslinking density (q), gel content and absorption capacity (AC) of synthesized SAPs

SAP	[AA] [M]	[KA] [M]	[SPM] [M]	[BMEP] [M]	M_c [g/mol]	q	Gel content [%]	AC [$g_{water}/g_{dry\ hydrogel}$]
SAP1	0.635	0.715	0.635	0.00118	14 093 600	78 997	86	1387
SAP2	1.270	0.358	0.358	0.00118	31 511 864	212 717	92	1715
SAP3	–	0.715	1.270	0.00118	26 630 539	122 481	93	1521
SAP4	0.953	0.715	0.318	0.00118	11 928 455	82 386	87	1175
SAP5	1.270	–	0.715	0.00118	24 793 604	133 867	88	2618
SAP6	1.270	0.538	0.178	0.00118	23 575 791	192 227	85	1469
SAP7	–	–	1.985	0.00118	14 036 977	57 341	92	1587
SAP8	1.270	–	0.715	0.00155	25 217 194	139 719	91	1696
SAP9	1.270	–	0.715	0.00195	25 877 562	136 154	93	1484
SAP10	1.270	–	0.715	0.00233	26 093 318	140 884	90	1376

Constant amounts of NIPAM (0,05 M) and KPS (0,009 M) were used in all experiments for a polymerization volume of 40 mL; AA (acrylic acid); KA (potassium acrylate); SPM (3-sulfopropyl methacrylate potassium salt.); BMEP (*bis*[2-(methacryloyloxy)ethyl] phosphate). AC corresponds to the absorption capacity in distilled water.

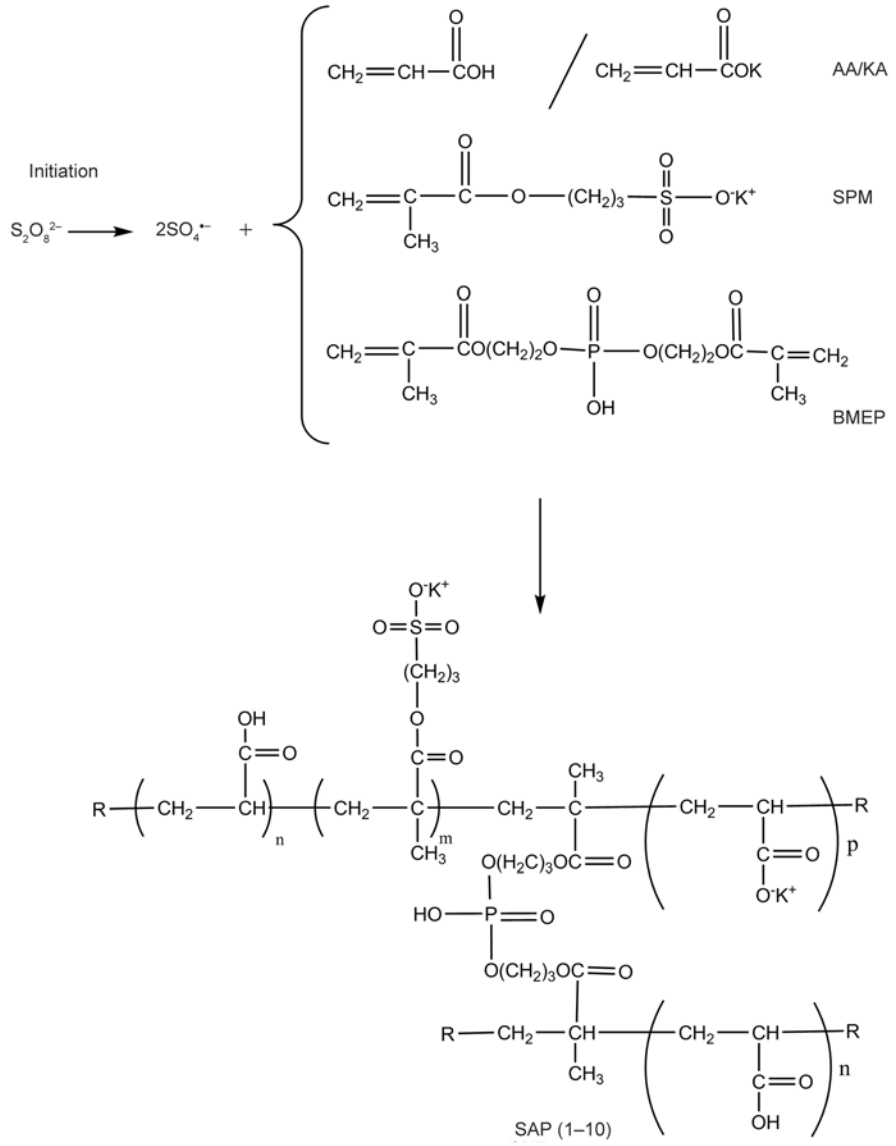

Figure 1. Reaction scheme to originate SAP polymers

materials have, in general, excellent swelling properties with very high water absorption capacities between 1175 and 2618 g water/g dry hydrogel. This fact is explained by the high charge density of the material, and it is particularly relevant in the case of SAP5. From Table 1, it is possible to observe that the gel contents are between 80–90%, suggesting that during the reaction there was an efficient formation of an insoluble copolymer network and that the synthesized hydrogels have a highly crosslinked structure.

The approximate molecular weight between crosslinks, obtained from Equation (2), showed high values for the different SAPs, between 11.928 and 31.511 Mg/mol. Also, the polymers showed a high crosslinking density (60 788 to 221 063). Unfortunately, no direct correlation between values of M_c and q with polymer swelling capacity can be made. The same was observed in the work of Venkatachalam *et al*. [11]. In the case of SAP5, which showed the highest swelling capacity value, the molecular weight between crosslinkings was approximately 24.793 millions with a q value of 140 724. Comparing with related hydrogels [11] using trimethylolpropane as crosslinking agent, the use of BMEP for the same purpose and SPM as a major monomer greatly improved the swelling properties of the materials.

The water absorption capacity of the SAPs is influenced by the nature and relative amounts of monomers used in the synthesis. The maximum water absorption capacity of SAPs with different amounts of monomers (SAP1–SAP7) are represented in Figure 2.

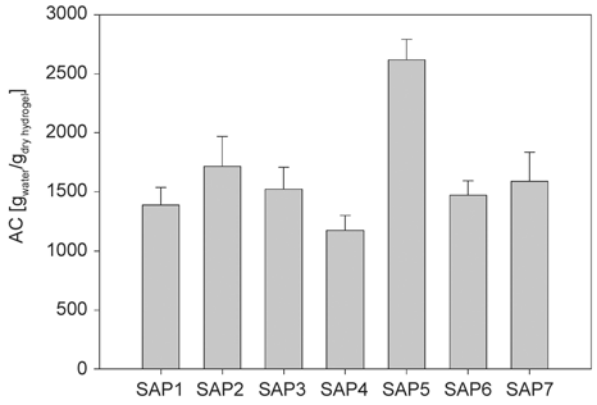

Figure 2. Water absorption capacity for the different SAP

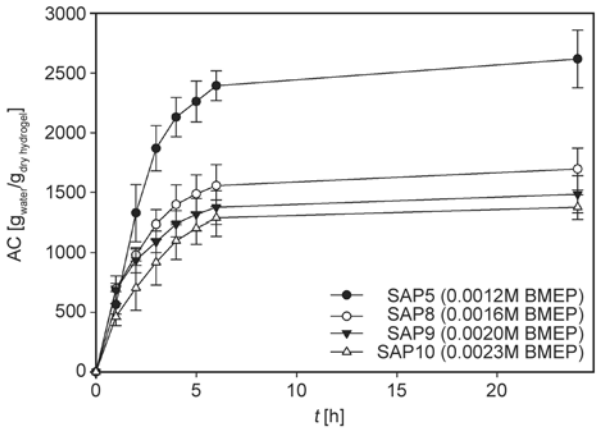

Figure 3. Effect of crosslinker amount (BMEP) on water absorption capacity of SAPs

The results shown in Figure 2 indicate that the water absorption capacity is higher for the hydrogels containing higher amounts of two monomers, AA and SPM (SAP5). When the amount of SPM decreases and KA is used as co-monomer (0.358 KA and 0.358 SPM on SAP2 or 0.178 SPM and 0.538 KA for SAP6), hydrogels with lower absorption capacities are obtained. The presence of AA is essential to afford high swelling properties. Hydrogels prepared in the absence of this monomer (SAP7 and SAP3) originate materials with lower swelling values. It is assumed that the presence of the highly polar sulfonate group in the structure of the SPM has a key role in the absorption capacity of the SAPs [22, 23]. The amount of crosslinker is also determinant for the swelling behaviour of hydrogels [4, 24]. The most promising result was obtained for SAP5, where AA and SPM were used as monomers, and with a BMEP concentration of 0,00118 M. The ratio of charged monomers to BMEP is very low (approximately 1.100) as well as its concentration (0.0018 M). These two parameters contribute to low crosslink density in the gel structure which favours swelling properties. Attempts were made to synthesize SAPs with crosslinker concentrations lower than 0,00118 M, but the obtained material dissolved in water when swelling studies were carried out. At low concentration of crosslinking agent, there is not enough crosslinking density and the formed network is too loose and does not have enough strength to hold water molecules inside the structure [4, 25]. The concentration initially used seems to provide an interesting compromise between the crosslinking level and a stable gel structure. Increasing the amount of BMEP decreases the water absorption capacities (Figure 3).

At crosslinker concentrations higher than 0,00118 M, hydrogels with higher crosslinking densities were obtained, leading to lower water absorption capacities. In these conditions, a tighter network structure, with a high number of crosslinking points is expected, which results in a reduction in the absorption capacity of the hydrogel [9].

The swelling profiles in distilled water (Figure 3) also shows that all SAPs present a fast water absorption capacity. SAP5, with higher swelling capacity, presents almost the same initial water absorption capacity as the other SAPs but mantains this initial absorption rate for a longer time (7 h) unlike the others, that at this time, presents a much lower water absorption value. Interestingly the time to achieved almost the maximum swelling values is the same for all the SAPs (7 h).

Due to the excellent results obtained for SAP5, in terms of water swelling and also in terms of reproducibility (two synthesis carried out at different times led to SAPs with swelling abilities of 2437 and 2618 $g_{water}/g_{dry\ hydrogel}$), it was decided to fully characterize only this SAP in terms of chemical structure, morphology, and thermal stability. Its swelling capacity in solutions with different ionic strengths, and different pHs was also studied. Finally, this SAP was tested as a release system using urea as model compound.

3.4. SAP5 characterization

The FTIR spectra of SAP5, AA and SPM are presented in Figure 4.

From Figure 4a, it is possible to observe the disappearance of the bands corresponding to the double bonds (ν–C=C– at *ca*. 1636 cm^{-1} and δ–C=C– at *ca*. 815 cm^{-1}) in the spectrum of SAP5. In Figure 4b only the spectrum of SAP5 is represented. It is possible to identify a band at *ca*. 1720 cm^{-1} that has con-

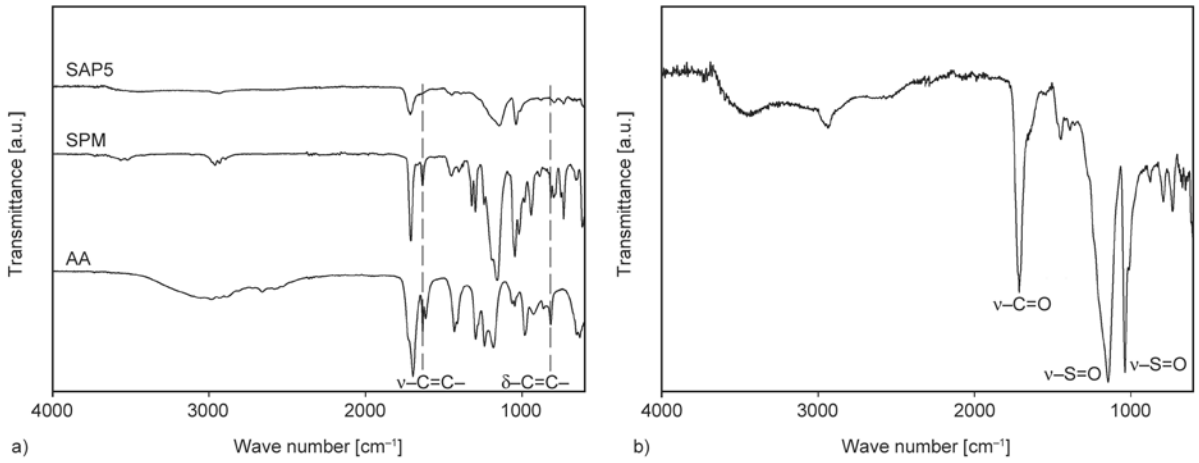

Figure 4. FTIR spectra of SAP5, AA and SPM (a) and SAP5 (b)

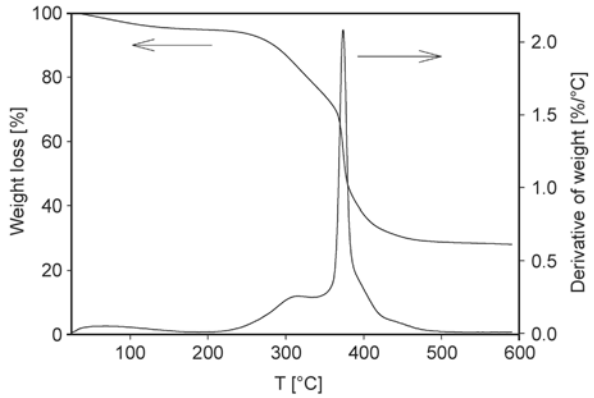

Figure 5. Thermoanalytical curve of SAP5

tributions from both the vibrations of the carbonyl group of ester linkages and from the carbonyl group of the carboxylic acid groups involved in hydrogen bonds. At 1139 and 1038 cm^{-1} the bands corresponding to the stretching vibrations of the –S=O groups appear. The bands corresponding to the stretching vibrations of the –P=O group, that typically appear at 1350–1250 cm^{-1} are overlapped with those corresponding to the –S=O groups [26]. Taking into account the results obtained by the FTIR analysis it is possible to say that the crosslinking reaction was successful.

The thermal stability of SAP5 was evaluated by TGA, from 30 to 600 °C, under a nitrogen flow. Figure 5 gives a global view of the thermal behaviour of SAP5.

It can be observed from Figure 4 that SAP5 undergoes a small initial mass loss of 5% (close to 100 °C), probably due to the existence of residual water in the sample. Around 250 °C, the polymer shows the first relevant and sharp mass loss. This event is due to a degradation of the PAA fractions of the polymer corresponding to the anhydride formation, followed by its decomposition [27]. Finally, the greatest weight loss (approximately 40% of the total mass)

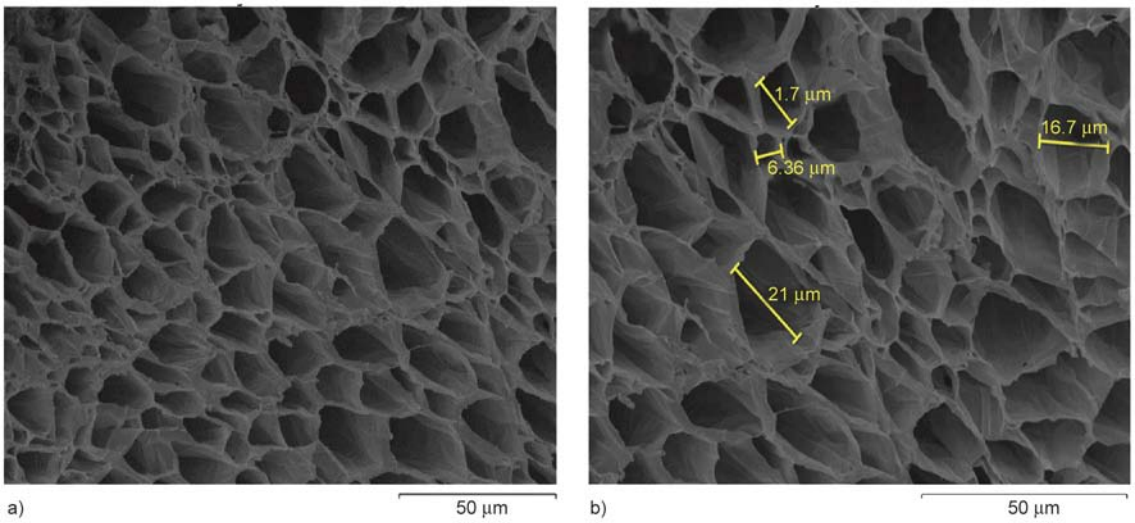

Figure 6. Micrograph of the SAP5 cross-section obtained by SEM: magnification of 750× (a), and magnification of 1000× (b)

from 360 to is close to 450 °C is due to main chain degradation events [28].

In order to get information about the internal morphology of SAP5, a previously swolen sample was freeze dried and SEM images were taken. Figure 6 presents the images of the SAP5 cross-section obtained by the SEM analysis.

From Figure 6 it is possible to see that SAP5 has a honeycomb like morphology and a high porosity. The highly porous structure presented by SAP5 with pore sizes between 6 and 21 μm and with a predominance of large pores allows an easy access of water, which contributes to the good swelling properties of the hydrogel, particularly to the fast kinetics of absorption (Figure 2). Additionally, the great number of pores creates a considerable number of reservoirs for water.

3.4.1. SAP5 swelling studies in different conditions

The swelling behaviour of this kind of hydrogels is highly dependent on the ionic strength of the solutions [29]. The effect of the concentration of salt solutions on the swelling behaviour of SAP5 is shown in Figure 7.

As observed in Figure 7, the maximum swelling values for SAP5 in different saline solutions are much lower than those obtained in distilled water, with a reduction of two orders of magnitude, from 2600 to around 60 $g_{water}/g_{dry\ hydrogel}$ (1.5 wt% NaCl). This result is expected, taking into account the mechanism of swelling of this charged hydrogel and suggests that the developed SAP can be very responsive to salt concentration. As the ionic strength increases, the osmotic pressure, that is the main the driving force of swelling, is reduced due to a less difference in concentrations of mobile ions between the charged polymer network in the gel and environment solution [30, 31]. Also, as the solution presents high ionic strength, electrostatic repulsion between charged polymer chains is decreased due to shielding effect thus reducing volume availability.

In order to investigate the SAP5 sensibility to the pH, swelling equilibrium experiments were performed to study water absorption at different pHs (3, 5, 7, 9 and 11). The results are presented in Figure 8.

From Figure 8 it is possible to observe that SAP5 exhibits different water absorption values, depending on the pH of the water solution. The highest water absorption capacity (*ca*. 2600 $g_{water}/g_{dry\ hydrogel}$) was achieved in neutral medium. It is possible to see that at pH values lower or higher than 7, the absorption capacity of the SAP5 is significantly reduced. When SAP5 is in an acidic pH there is an increase in the degree of protonation of the carboxylate (first) and then of the sulfonic groups. With these conditions, the electrostatic repulsion between the negatively charged groups is diminished, causing a contraction of the polymer network [32–34]. The results revealed that for neutral conditions (pH = 7), a maximum number of ionized carboxylate and sulfonate groups are achieved and the electrostatic repulsive force between them is at its highest value, contributing to the great water absorption capacity shown by the SAP sample. At pH higher than 7, the increase in the concentration of the sodium cations exerts a screening effect over the anions and the amount of ions inside the network also increases. These effects prevent the repulsive forces between the polymeric charged chains and increases the ionic strength of the solution

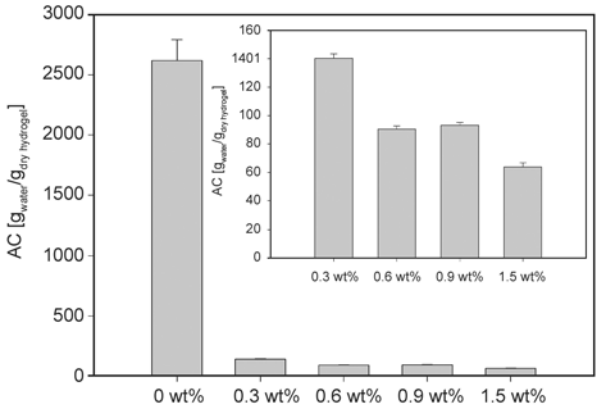

Figure 7. Maximum water absorption capacity of SAP5 in distilled water and in NaCl solutions with different concentrations, after 24 hours

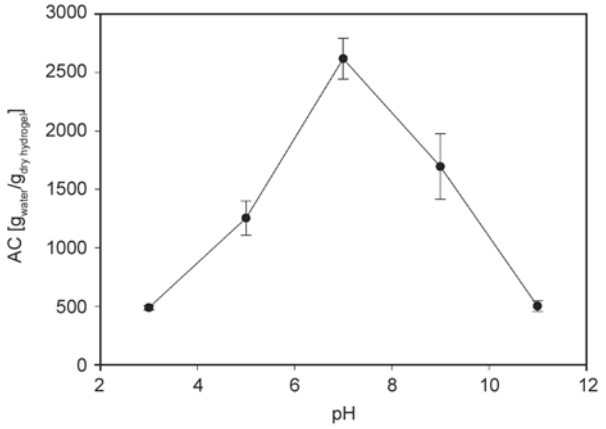

Figure 8. Water absorption capacity of SAP5 at different pHs, after 24 hours

near polymer surfaces, reducing the total swelling capacity [28].

3.4.2. Water retention in mixture soil/SAP5

For agricultural use it is important to evaluate the ability of the hydrogel to retain water in the soil, as well as the benefits of this material for the improvements in soil water absorption capacity. Figure 9 shows the percentage of water retained by the soil for several days after an initial irrigation of a soil sample (50% of water relatively to initial soil mass) with different amounts of SAP5 [15]. The value of 100% corresponds to the initial weight of water/soil/polymer mixtures.

From Figure 9, it can be seen that the amount of water in the control soil (without SAP) reaches zero after 11 days. In the soil with 0.5 wt% SAP the amount of water only reaches 0% between 12 and 14 days. In soils with 1 and 2 wt% of SAP, there is still water present in the soil even after 15 days. These results show the clear role of SAP 5 in the improvement of soil humidity which results in a gain of 50% of time to reach soil dryness. During the first 2 days of the test the curves have a similar profile, which indicates that the water being lost corresponds to water bonded to the soil. Near day 3, the slope of the curves diverges according to the amount of SAP present in the mixture. This observation indicates that, beyond this time, the water loss corresponds to water bonded to the hydrogel [15, 16].

3.4.3. SAP 5 urea release ability

In addition to the water absorption properties, superabsorbent hydrogels could also be useful in the controlled release of fertilizers and particularly urea, one of the most frequently used compounds [35]. First, the hydrogel's capacity to load urea was studied using urea solutions with different concentrations. After promoting the swelling of SAP5 in these solutions, the hydrogels were freeze dried and, by measuring their weights, it was possible to calculate the amount of loaded urea (Figure 10).

As expected, the loading capacity increases for higher amounts of urea available in the solution, due to a higher diffusion to the hydrogel structure. SAP5 shows a urea loading capacity that reaches the maximum value of 30 $g_{of\ urea}/g_{polymer}$ (corresponding to 3000%) when in contact with a urea solution with 20 g/L of concentration. This value of loading capacity is significantly higher than those presented in literature for agricultural hydrogels [14], and is a direct consequence of the high absorption capacity of SAP5.

Also important is the ability of the hydrogel to release the urea. The dry hydrogel obtained in the experiment with the urea solution of 20 g/L was placed in distilled water and the amount of urea released with time was monitored gravimetrically. The results are shown in Figure 11.

In terms of urea release, it can be seen from Figure 11 that the process is quite slow, especially when compared with other works reported [14]. After 8 hours, only 50% of the absorbed urea was released, and only after 48 hours did the release achieve a plateau, corresponding to the release of 91% of urea originally present in the SAP. Taking into account the fast kinetics of water absorption (see Figure 3), a faster release of the urea from the SAP was expected. However, it is known that urea can interact with carboxylic acid groups by hydrogen bonding [36,

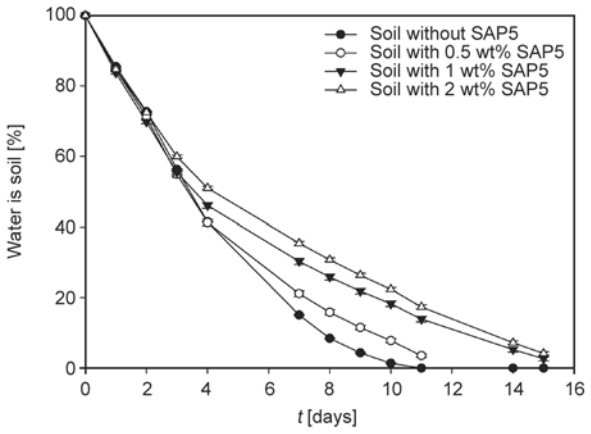

Figure 9. Water retention in soil and in mixtures soil/SAP5. Control soil without any SAP (blank) and soils with increasing amount of SAP (0.5, 1 and 2 wt%).

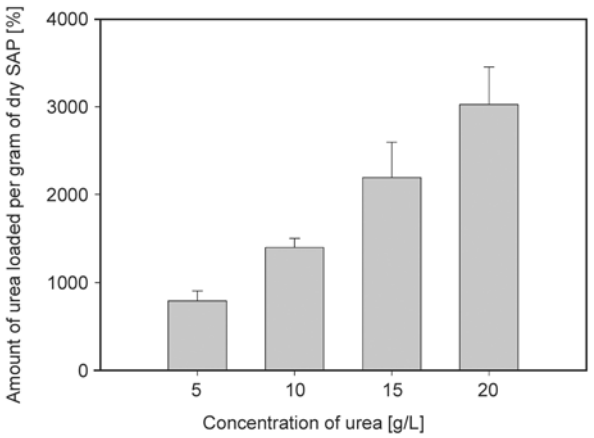

Figure 10. Effect of urea solution on the loading [%] of SAP5

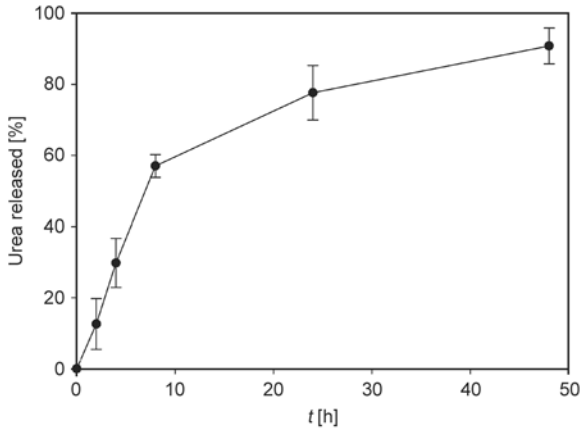

Figure 11. Urea release profile of urea loaded SAP5

37], a fact that might contribute to a slower urea release.

4. Conclusions

A set of novel SAPs based on AA, KA, SPM and NIPAM monomers, and BMEP bifunctional crosslinker, were prepared by free radical polymerization, using KPS as initiator. Several formulations were tested and the best results were obtained for a SAP (SAP5) made from AA (1,270 M), SPM (0,715 M), with a concentration of BMEP of 0,00118 M. SAP5 presents excellent water absorption capacity (2618 $g_{water}/g_{dry\ hydrogel}$) when compared to the commonly reported hydrogels. It has a highly porous structure and good thermal stability. Moreover, when mixed with the soil it allows improvements in water retention. This hydrogel has the capacity of being loaded with high amounts of urea (30 $g/g_{dry\ hydrogel}$) and presents a slow urea release when placed in water. To sum up, the results obtained in this work indicate that, by its characteristics, SAP5 can be a potential candidate for agricultural applications.

Acknowledgements

This work was developed during the Agrofoam project in collaboration with Flex2000 and the authors gratefully acknowledge Qren Program 34022 for financial support.
The NMR data was collected at the UC-NMR facility which is supported in part by FEDER – European Regional Development Fund through the COMPETE Programme (Operational Programme for Competitiveness) and by National Funds through FCT – Fundação para a Ciência e a Tecnologia (Portuguese Foundation for Science and Technology) through grants REEQ/481/QUI/2006, RECI/QEQ-QFI/0168/2012, CENTRO-07-CT62-FEDER-002012, and Rede Nacional de Ressonância Magnética Nuclear (RNRMN).

References

[1] Hüttermann A., Orikiriza L. J. B., Agaba H.: Application of superabsorbent polymers for improving the ecological chemistry of degraded or polluted lands. CLEAN – Soil, Air, Water, **37**, 517–526 (2009). DOI: 10.1002/clen.200900048

[2] Ahmed E. M.: Hydrogel: Preparation, characterization, and applications: A review. Journal of Advanced Research, **6**, 105–121 (2015). DOI: 10.1016/j.jare.2013.07.006

[3] Zohuriaan-Mehr M. J., Kabiri K.: Superabsorbent polymer materials: A review. Iranian Polymer Journal, **17**, 451–477 (2008).

[4] Laftah W. A., Hashim S., Ibrahim A. N.: Polymer hydrogels: A review. Polymer-Plastics Technology and Engineering, **50**, 1475–1486 (2011). DOI: 10.1080/03602559.2011.593082

[5] Sannino A., Demitri C., Madaghiele M.: Biodegradable cellulose-based hydrogels: Design and applications. Materials, **2**, 353–373 (2009). DOI: 10.3390/ma2020353

[6] Döll P.: Impact of climate change and variability on irrigation requirements: A global perspective. Climatic Change, **54**, 269–293 (2002). DOI: 10.1023/A:1016124032231

[7] Dabhi R., Bhatt N., Pandit B.: Super absorbent polymers – An innovative water saving technique for optimizing crop yield. International Journal of Innovative Research in Science, Engineering and Technology, **2**, 5333–5340 (2013).

[8] Zohuriaan-Mehr M. J., Omidian H., Doroudiani S., Kabiri K.: Advances in non-hygienic applications of superabsorbent hydrogel materials. Journal of Materials Science, **45**, 5711–5735 (2010). DOI: 10.1007/s10853-010-4780-1

[9] Bakass M., Mokhlisse A., Lallemant M.: Absorption and desorption of liquid water by a superabsorbent polymer: Effect of polymer in the drying of the soil and the quality of certain plants. Journal of Applied Polymer Science, **83**, 234–243 (2002). DOI: 10.1002/app.2239

[10] Bertoldo M., Bronco S., Gragnoli T., Ciardelli F.: Modification of gelatin by reaction with 1,6-diisocyanatohexane. Macromolecular Bioscience, **7**, 328–338 (2007). DOI: 10.1002/mabi.200600215

[11] Venkatachalam D., Vediappan V., Kaliappa Gounder S.: Synthesis and evaluation of trimethylolpropane triacrylate crosslinked superabsorbent polymers for conserving water and fertilizers. Journal of Applied Polymer Science, **129**, 1350–1361 (2013). DOI: 10.1002/app.38826

[12] Flory P. J., Rehner J.: Statistical mechanics of cross-linked polymer networks II. Swelling. The Journal of Chemical Physics, **11**, 521–526 (1943). DOI: 10.1063/1.1723792

[13] Yarimkaya S., Basan H.: Synthesis and swelling behavior of acrylate-based hydrogels. Journal of Macromolecular Science Part A, **44**, 699–706 (2007). DOI: 10.1080/10601320701351268

[14] Raafat A. I., Eid M., El-Arnaouty M. B.: Radiation synthesis of superabsorbent CMC based hydrogels for agriculture applications. Nuclear Instruments and Methods in Physics Research Section B: Beam Interactions with Materials and Atoms, **283**, 71–76 (2012). DOI: 10.1016/j.nimb.2012.04.011

[15] Abd El-Rehim H. A.: Characterization and possible agricultural application of polyacrylamide/sodium alginate crosslinked hydrogels prepared by ionizing radiation. Journal of Applied Polymer Science, **101**, 3572–3580 (2006). DOI: 10.1002/app.22487

[16] Demitri C., Scalera F., Madaghiele M., Sannino A., Maffezzoli A.: Potential of cellulose-based superabsorbent hydrogels as water reservoir in agriculture. International Journal of Polymer Science, **2013**, 435073/1–435073/6 (2013). DOI: 10.1155/2013/435073

[17] Jang J., Jeong Y-K.: Synthesis and flame-retardancy of UV-curable methacryloyloxy ethyl phosphates. Fibers and Polymers, **9**, 667–673 (2008). DOI: 10.1007/s12221-008-0105-2

[18] Okay O.: General properties of hydrogels. in 'Hydrogels sensors and actuators' (eds.: Gerlach G., Arndt K-F.) Springer, Berlin, 1–14 (2010).

[19] Hunkeler D.: Mechanism and kinetics of the persulfate-initiated polymerization of acrylamide. Macromolecules, **24**, 2160–2171 (1991). DOI: 10.1021/ma00009a004

[20] Subramanian K.: Photodecomposition of poly(styrene peroxide) in vinyl monomers and structural features of the formed polymers. European Polymer Journal, **37**, 55–64 (2001). DOI: 10.1016/S0014-3057(00)00076-8

[21] Stevens M. P.: Polymer chemistry: An introduction. Oxford University Press, Oxford (1999).

[22] Peng G., Xu S., Peng Y., Wang J., Zheng L.: A new amphoteric superabsorbent hydrogel based on sodium starch sulfate. Bioresource Technology, **99**, 444–447 (2008). DOI: 10.1016/j.biortech.2007.01.018

[23] Scognamillo S., Alzari V., Nuvoli D., Illescas J., Marceddu S., Mariani A.: Thermoresponsive super water absorbent hydrogels prepared by frontal polymerization of *N*-isopropyl acrylamide and 3-sulfopropyl acrylate potassium salt. Journal of Polymer Science Part A: Polymer Chemistry, **49**, 1228–1234 (2011). DOI: 10.1002/pola.24542

[24] Elliot M.: Superabsorbent hydrogels. BASF report (2014).

[25] Karadağ E., Saraydin D.: Swelling of superabsorbent acrylamide/sodium acrylate hydrogels prepared using multifunctional crosslinkers. Turkish Journal of Chemistry, **26**, 863–875 (2002).

[26] Coates J.: Interpretation of infrared spectra, A practical approach. in 'Encyclopedia of analytical chemistry' (ed.: Meyers R. A.) Wiley, Chichester (2000). DOI: 10.1002/9780470027318.a5606

[27] Garay M. T., Alava C., Rodriguez M.: Study of polymer–polymer complexes and blends of poly(*N*-isopropylacrylamide) with poly(carboxylic acid). 2. Poly (acrylic acid) and poly(methacrylic acid) partially neutralized. Polymer, **41**, 5799–5807 (2000). DOI: 10.1016/S0032-3861(99)00765-X

[28] Chen Y., Tan H-M.: Crosslinked carboxymethylchitosan-g-poly(acrylic acid) copolymer as a novel superabsorbent polymer. Carbohydrate Research, **341**, 887–896 (2006). DOI: 10.1016/j.carres.2006.01.027

[29] Quesada-Pérez M., Maroto-Centeno J. A., Forcada J., Hidalgo-Alvarez R.: Gel swelling theories: The classical formalism and recent approaches. Soft Matter, **7**, 10536–10547 (2011). DOI: 10.1039/C1SM06031G

[30] Khare A. R., Peppas N. A.: Swelling/deswelling of anionic copolymer gels. Biomaterials, **16**, 559–567 (1995). DOI: 10.1016/0142-9612(95)91130-Q

[31] Liu X., Tong Z., Hu O.: Swelling equilibria of hydrogels with sulfonate groups in water and in aqueous salt solutions. Macromolecules, **28**, 3813–3817 (1995). DOI: 10.1021/ma00115a010

[32] Chen J., Zhao Y.: An efficient preparation method for superabsorbent polymers. Journal of Applied Polymer Science, **74**, 119–124 (1999). DOI: 10.1002/(SICI)1097-4628(19991003)74:1<119::AID-APP14>3.0.CO;2-T

[33] Bao Y., Ma J., Li N.: Synthesis and swelling behaviors of sodium carboxymethyl cellulose-g-poly(AA-*co*-AM-*co*-AMPS)/MMT superabsorbent hydrogel. Carbohydrate Polymers, **84**, 76–82 (2011). DOI: 10.1016/j.carbpol.2010.10.061

[34] Mahdavinia G. R., Pourjavadi A., Hosseinzadeh H., Zohuriaan M. J.: Modified chitosan 4. Superabsorbent hydrogels from poly(acrylic acid-*co*-acrylamide) grafted chitosan with salt- and pH-responsiveness properties. European Polymer Journal, **40**, 1399–1407 (2004). DOI: 10.1016/j.eurpolymj.2004.01.039

[35] Zheng T., Liang Y., Ye S., He Z.: Superabsorbent hydrogels as carriers for the controlled-release of urea: Experiments and a mathematical model describing the release rate. Biosystems Engineering, **102**, 44–50 (2009). DOI: 10.1016/j.biosystemseng.2008.09.027

[36] Jones A. O. F., Leech C. K., McIntyre G. J., Wilson C. C., Thomas L. H.: Engineering short, strong hydrogen bonds in urea di-carboxylic acid complexes. CrystEngComm, **16**, 8177–8184 (2014). DOI: 10.1039/C4CE00587B

[37] Ohlam R., Narasimhan B., Ohlan S., Narang R., Judge V.: Synthesis and antimicrobial evaluation of urea inclusion complexes. Organic Communications, **1**, 24–32 (2008).

eXPRESS Polymer Letters Vol.10, No.3 (2016) 259–272
Available online at www.expresspolymlett.com
DOI: 10.3144/expresspolymlett.2016.24

Electrically conducting polymer nanostructures confined in anodized aluminum oxide templates (AAO)

*I. Blaszczyk-Lezak, V. Desmaret, C. Mijangos**

Instituto de Ciencia y Tecnología de Polímeros, CSIC, Juan de la Cierva 3, 28006 Madrid, Spain

Received 16 July 2015; accepted in revised form 15 October 2015

Abstract. Intrinsically or extrinsically conducting polymers are considered good candidates for replacement of metals in specific applications. In order to further expand their applications, it seems necessary to examine the influence of confinement effects on the electric properties of nanostructured conducting polymers in comparison to the bulk. The present study reports a novel way to fabricate and characterize high quality and controllable one-dimensional (1D) polymer nanostructures with promising electrical properties, with the aid of two examples polyaniline (PANI) and poly(vinylidene fluoride) with multiwall carbon nanotubes (PVDF-MWCNT) as representative of intrinsically and extrinsically conducting polymers, respectively. In this work, porous anodic aluminum oxide (AAO) templates have been used both as a nanoreactor to synthesize 1D PANI nanostructures by polymerization of the ANI monomer and as a nanomold to prepare 1D PVDF-MWCNT nanorods by melt infiltration of the precursor PVDF-MWCNT film. The obtained polymer nanostructures were morphologically and chemically characterized by SEM and Confocal Raman Spectroscopy, respectively, and the electrical properties determined by Broadband Dielectric Spectroscopy (BDS) in a non-destructive way. SEM study allowed to establish the final nanostructure of PANI and PVDF-MWCNT and confirmed, in both cases, the well-aligned and uniform rod-like polymer nanostructures. Confocal Raman Microscopy has been performed to study the formation of the conducting emeraldine salt of PANI through all the length of AAO nanocavities. Finally, the electrical conductivity of both types of polymer nanostructures was easily evaluated by means of Dielectric Spectroscopy.

Keywords: *nanocomposites, conducting polymers, Broadband dielectric spectroscopy, AAO template*

1. Introduction

Conducting polymers are considered good candidates to replace traditional metals in specific applications. Indeed, this new generation combines advantages of polymers (lighter weight, mechanical flexibility, easy-processing, biocompatibility, chemical stability) and conducting materials (electrical properties). Among polymers, conduction can be achieved by the intrinsically conducting polymers (ICP), i.e., polymers with alternating double bonds in their chemical structure or by the extrinsically conducting polymers (ECP), i.e., polymers with added conductive nanofillers to the matrix.

In order to further improve the properties of these materials, as well as expand their applications, the study of the polymer nanostructures could have some advantages, like in case of one-dimensional polymer nanostructures (1D). In fact, it was reported that nanofibrils exhibit higher electronic conductivities compared to conventional forms of the same polymer material [1]. It has been also reported potential applications of nanostructured conducting polymers that include electromagnetic [2, 3] and radio frequency interference shielding for electronic devices, electrostatic charge dissipation [4] and conductive paints [5], organic light emitting diodes (OLED) [6], bio- [7] and chemical sensors [8, 9], photovoltaics

*Corresponding author, e-mail: cmijangos@ictp.csic.es

[10, 11], electrochromic devices [12], energy storage [13, 14], corrosion protection [15], plastic digital memory [16], bio-engineering [17] *etc*.

One of the routes to synthesize one-dimensional conducting polymer nanostructures is the use of anodized aluminum (AAO) hard templates since dimension, aspect ratio and electrical properties of the resulting polymer nanostructures can be tailored and therefore it can provide new opportunities for confinement studies and/or for technological challenges. In this sense, a few years ago, Martin and coworkers [18, 19], reported that the polymerization of ANI into the pores of polycarbonate filters improved the conducting properties of the polymer in comparison to bulk. He suggested that the improvement in electronic conductivity results from enhancement in the supermolecular order within the template-synthesized fibers. Authors used four-point conductivity measurement which requires the preparation of thin films.

Some years later, Marquez and coworkers [20, 21], presented a different approach to this topic. The author synthesized patterned polymeric nanostructures by template assisted admicellar polymerization (TAAP) and studied AC impedance measurements (via a current-sensing AFM apparatus). The results revealed a dependence of electrical conductivity values of PANI honeycombs not only on polymerization conditions and doping but on the template size too (biggest spheres, biggest conductivity). Recently, Wu *et al*. [22] investigated the conductivity of doped with different acids PANI nanoarrays prepared through a soft template method. The thermoconductivity measurements showed an organic semiconductor characteristic, so that, the electrical conductivity increase with the rise of temperature. Another way of preparing PANI nanostructures was presented by Khdary *et al*. [23]. Authors produced high surface area mesoporous polyaniline on the surface of glassy carbon electrodes by the electrochemical polymerization from a composite obtaining high value of capacitance.

To our best knowledge, although Broadband dielectric spectroscopy (BDS) is a sensitive technique to evaluate dielectric response of polymer nanostructure [24–28] and to measure polymer conductivity as a function of frequency and temperature, it has never been employed to study the electrical response of confined conducting polymers in AAO templates, even if this type of measurement have been currently done in bulk and thin films [29]. In addition, it is possible to use the template without additional preparation. The aim of this work is to evaluate the electric conducting properties of two kind of conducting polymer confined in the nanocavities of AAO templates. Polyaniline (PANI) has been chosen as representative of an intrinsically conducting polymer (ICP) and PVDF-MWCNT composite, made of poly(vinylidene fluoride) (PVDF) and multiwall carbon nanotubes (MWCNT), as representative of the extrinsically conducting polymer (ECP). Laboratory-made anodized aluminium oxide templates with controlled pore sizes have been employed for polymer nanostructures preparation. Polyaniline nanostructures have been obtained by 'in situ' polymerization of ANI in the AAO nanopores while PVDF-MWCNTs nanorods, by melt infiltration of a PVDF-MWCNTs film in the AAO nanopores. Their posterior morphological, chemical and electrical characterization has been carried out by SEM, Raman and BD spectroscopy.

2. Experimental

2.1. Materials

Aluminium foils of 99.999% were purchased from Goodfellow Cambridge Ltd. (Huntingdon, United Kingdom); Anilyne (≥99.5%) and PVDF ($M_w \approx$ 180 000) supplied by Sigma-Aldrich (Madrid, Spain); Anhydrous N,N-dimethylformamide (DMF) provided by Carlo Erba Reagents (Sabadell, Spain) (purity ~99.9%); and MWCNTs synthesized by the M.A. Lopez Manchado (Instituto de Ciencia y Tecnología de Polímeros, CSIC, Madrid, Spain) (nominal inner diameter d_i ~ 12.5 nm, outer diameter d_0 ~ 44 nm and length l~160 μm).

2.2. AAO template synthesis

Two types of ordered AAO templates have been prepared by a two-step electrochemical anodization process of aluminum foils. Firstly, ultrapure aluminum foils were cleaned and degreased by sonication in solvents of different polarity (acetone, isopropanol, deionized water and ethanol). Then, they were electropolished during 4 min in a solution of perchloric acid/ethanol (1/3) under a constant voltage of 20 V with a maximum current of 1.5 A. After that, in order to prepare templates with 35 nm diameter of pores, the first anodization was achieved using oxalic acid as electrolyte at 40 V and 3–5 °C for 24 h in a subsequent step, the anodic layer was removed into chromic and phosphoric acid solution. This was

followed by a second anodization process also in oxalic acid under the same conditions but during 65 h. After this stage, templates are characterized by an anodic aluminum oxide top layer with pores of 35 nm in diameter arranged into a hexagonal lattice of 100 nm, and by a non-oxidized Al layer substrate at its bottom. With the aim of preparation of templates with 140 nm diameter of pores, the first anodization was carried out in a solution of phosphoric acid (2%) and aluminum oxalate (0.02 M) at 195 V and temperature of 2–3 °C during 6 h. After removing the anodic layer, a second anodization process was carried out during 4 h. Under these conditions, the top layer exhibits pores of 140 nm in diameter and length of 20 μm.

The resulting 35 and 140 nm AAO templates were further treated in phosphoric acid to widen the pores up to 45 and 300 nm of diameter, respectively.

2.3. 'In situ' polymerization of ANI inside the AAO template

Before carrying out the polymerization, the liquid aniline monomer was dropped little by little on top of the AAO template until formation of a uniform layer and left for infiltration into the nanocavities at room temperature. The infiltration process was carried during 45 min for templates of 45 nm of diameter and during 8 h for the templates of 300 nm. Then, the excess of monomer from the aluminum was removed with sharp blades. Finally, infiltrated AAO template was quickly immersed in the 1 M oxidant agent, ammonium peroxidedisulfate (APS) and the doping acid, hydrochloric acid (HCl 1 M) solution and the reaction medium stirred mechanically and kept at 0 °C with the help of a refrigerating ethanol bath. The aniline monomer was polymerized with an APS concentration 1.4 times larger than ANI molar concentration, to ensure a complete reaction. Polymerization started after introduction of the template and was carried out during 2 h 30 min.

2.4. Infiltration of PVDF-MWCNTs films in AAO template

In order to prepare PVDF-MWCNTs composite film, firstly, MWCNTs were separately dispersed in dimethylformamide (DMF) at a desired concentration in two steps, by magnetic stirring and ultrasonication. The temperature of the process was controlled to avoid overheating. The MWCNTs dispersion was then immediately added to the PVDF in DMF solution while ultrasonicated continuously. Meanwhile sonication was still on, distilled water was added little by little to precipitate the solution. Afterwards, the solution was agitated to favor further precipitation. To remove the remaining DMF solvent, the polymer composite was washed with distilled water and centrifuged. The final product was dried using a lyophilization process with Telstar® Lyophilization Freeze Dry model L6-50. At the end the PVDF-MWCNTs composite presents a foamy appearance with uniform distribution of the MWCTNs and to achieve flat bulk films, all compositions were compressed using a Collins hydraulic hot press mold at a pressure of 50 Pa and at 210 °C for 10 min (0.3 mm thick film). Infiltration of PVDF-MWCNT composite was carried out in an oven under vacuum at controlled temperature by placing a PVDF-MWCNT film on the top of the AAO template. The temperature of the oven was maintained at 150 °C during 30 min to evaporate any moisture from the AAO template. Then, in order to infiltrate PVDF-MWCNTs in the nanocavities, the temperature was increased and maintained at 240 °C during 4 h. For infiltration of PVDF, pristine PVDF pellets were placed on the templates at 200 °C during 1 h. The infiltration was favored by application of mechanical force.

2.5. Characterization by scanning electron microscopy (SEM)

The AAO templates and the infiltrated samples were morphologically characterized by SEM/TEM (Philips XL-30ESEM and FESEM Hitachi model SU8000 with TE Detector). In order to perform the analysis of free polymer nanofibers, first, the aluminum substrate was eliminated by treatment with a mixture of HCl, $CuCl_2$ and H_2O, and then, the alumina was dissolved in 10 wt% H_3PO_4. Previously, in order to support the free nanostructures, a polymer coating was placed on the top of the template.

2.6. Raman spectroscopy

Bulk polymers and their polymer nanostructures inside the AAO nanocavities were characterized by Raman spectroscopy. A Renishaw In Via Raman Microscope (Renishaw plc, Wottonunder-Edge, UK) was used fitted with a grating spectrometer of 1200 lines/mm and a Peltier-cooled charge-coupled device (CCD) detector, coupled to a confocal microscope. All spectra were processed using Renishaw

WiRE 3.3 software. For polymer nanostructures, the measurements were carried out for the filled templates, following the methodology described by Maiz *et al*. [30]. Briefly, the Raman scattering was excited with a 785 nm near-infrared diode laser of 320 mW maximum input power. A 100×, NA090 microscope objective lens was used to focus the laser beam with a power of 0.1 W on the sample, giving a laser spot diameter of ±1 μm. With this objective the sampling depth is estimated to be around 4–5 μm (half-width of the confocal depth profile for a silicon wafer) and the lateral resolution is estimated to be about 1 μm with the system operated in the confocal mode. Depth profiles were obtained by focusing the microscope stepwise, at 10 μm intervals through the length of AAO templates of 45 nm of diameter×100 μm length and at 5 μm intervals through AAO templates of 300 nm diameters×20 μm length.

2.7. Broadband dielectric spectroscopy (BDS)

A Broadband dielectric spectrometer, Novocontrol GmbH Concept alpha-S analyzer, was used to measure the complex dielectric function of the bulk polymers and their nanostructures inside the AAO nanocavities, in the frequency range of 10^{-2}–10^{7} Hz in coupling with a nitrogen-jet stream quarto cryosystem to control the temperature in the range 100–600 K. The samples were placed between two gold-plated electrodes for AC conductivity measurements. To ensure good electrical contact with the gold-plated electrodes, the PANI bulk sample was compressed (10 t·mm^{-2}, 10 min) into a thin circular film of 500 μm thickness and 15 mm diameter.

For the polymer infiltrated AAO templates, the bottom part of aluminum layer was kept in contact with electrode, acting as a conducting electrode as well.

3. Results and discussion

3.1. AAO templates

The morphological study by SEM microscopy allows examining AAO templates. Figure 1 illustrates SEM micrographs of both kinds of synthesized alumina templates. Figures 1a and 1b correspond to the lateral and top view of AAO templates obtained by anodization in oxalic acid. The dimensions of the nanocavities are: 43.7 nm of diameter, 98.3 nm of interpore distance and, although no shown here, around 100 μm of length. Figure 1c presents the surface view of an AAO template obtained by anodization in phosphoric acid. The dimensions of the nanocavities are:

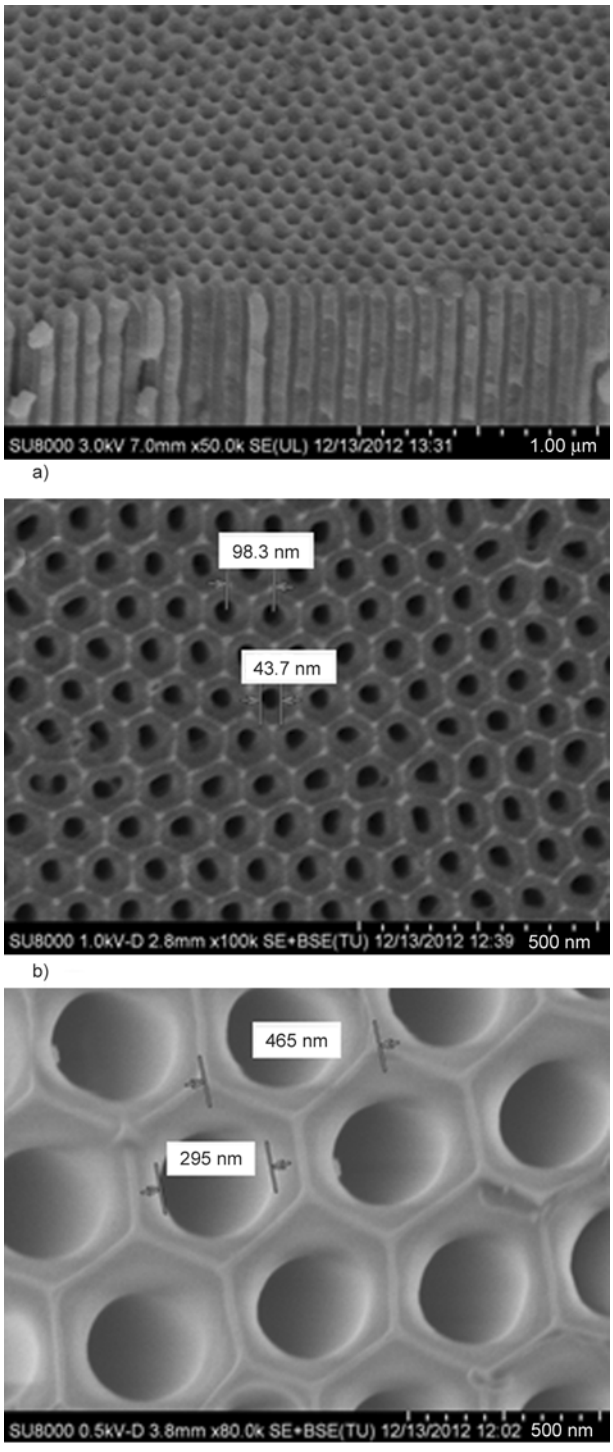

Figure 1. SEM micrographs of AAO template with 45 nm diameter pores, lateral view (a), and top view of 45 nm diameter pores (b) and 300 nm pores (c)

295 nm of diameter and 465 nm of interpore distance and, although no shown here, around 20 μm of length. From the above images, the main characteristic of the templates can be summarized: high quality order pores, regularity in the size of the pores and invariance of the diameter throw the length of template

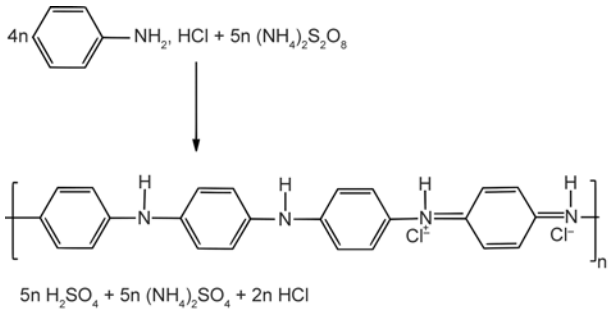

Figure 2. Chemical oxidative polymerization of aniline in a solution of APS/HCl to yield PANI-ES

3.2. PANI system

The oxidative polymerization of ANI, illustrated in Figure 2, is an exothermic process being the acid a by-product of the reaction, therefore, the course of reaction can be continuously monitored by recording the temperature and pH change of the solution medium. Although low temperature results in a polymer of higher molecular weight, less defects and undesirable branching, nevertheless, the polymerization time required is longer, consequently, a temperature of around 0 °C was chosen as a right compromise. This procedure was followed for polymerization in bulk and in AAO templates.

3.3. SEM micrographs

SEM micrographs of the one-dimensional PANI nanostructures obtained after the 'in situ' polymerization in AAO templates, once extracted from the templates, are collected in Figure 3. Figure 3a corresponds to PANI nanostructures obtained in AAO templates of 45 nm of diameter×100 μm of length and Figure 3b and 3c to those obtained in AAO of 300 nm×20 μm. In both cases and up to several tens of microns, it is observed that diameter and length size of nanofibers pattern the dimensions and symmetry of AAO. Nevertheless, some differences between them are found. For PANI nanostructures obtained in AAO nanocavities of dimensions 300 nm ×20 μm (Figure 3b and 3c) it can be clearly observed free-standing arrays of nanopillars. The determining factor for achieving such free-standing nanostructures is the low aspect ratio of nanostructure (about 60), although other factors such as rigidity, surface chemistry and electrostatic interactions could be also taken into consideration. For PANI nanostructures obtained in AAO nanocavities of dimension 45 nm×100 μm (Figure 3a) it is clearly noticed that PANI nanofibers tend to collapse. The collapse is certainly due to their high aspect ratio (order of magnitude 2300). Moreover, it results in an increase in the diameter of nanofibers (to around 70 nm) in comparison to that of template (45 nm). This fact can be explained by the agglomeration of two separated fibers as a consequence of the surface tension and the interaction between individual nanopillars.

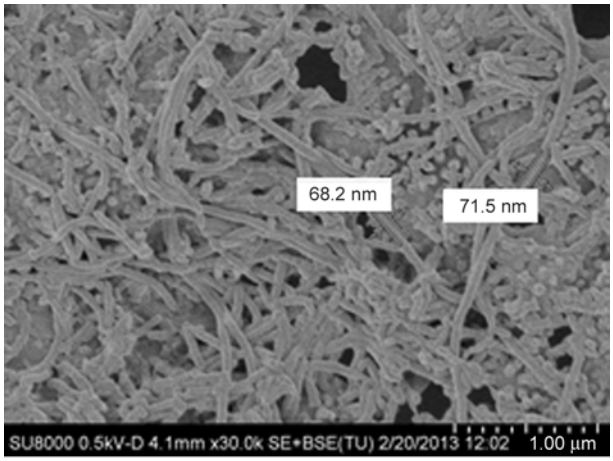

a)

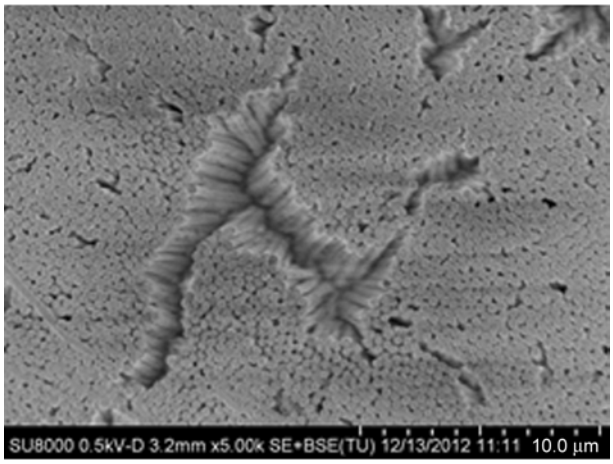

b)

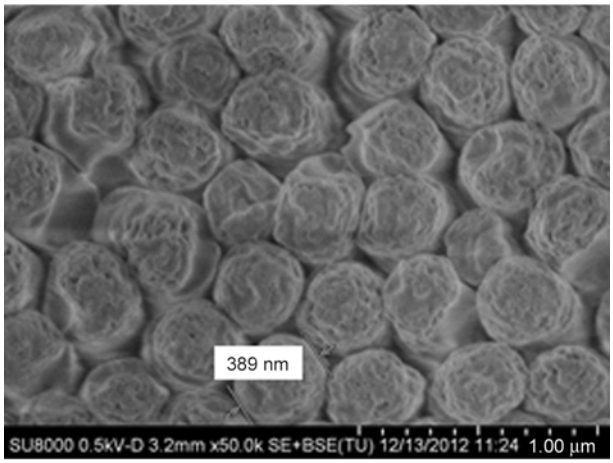

c)

Figure 3. Different magnifications of PANI into 45 nm AAO pores (a), and 300 nm AAO pore (b and c)

Be as it may, PANI nanostructures obtained by polymerization pattern the dimensions of AAO templates,

so their final dimensions can be adjusted as a function of the size of AAO nanocavities.

3.4. Raman spectroscopy

Raman spectroscopy was used to determine if PANI was polymerized correctly in the pores of the template and to check if the conductive (emeraldine salt, ES) form was obtained. First, the Raman spectrum of PANI bulk was analysed to serve as a reference, Figure 4a). The analysis of main regions of PANI-ES and their assignments are supported by data from other works [31–34]. The zone of most interest is the region 1000–1700 cm^{-1}. There are two dominating bands in the spectra, one corresponds to $\nu(C{=}C)_Q$ vibration of quinoid ring localized at 1595–1597 cm^{-1} and the other corresponds to the $\delta(C{-}H)_Q$ bending in-plane vibration of quinoid ring localized at 1167–1169 cm^{-1}.

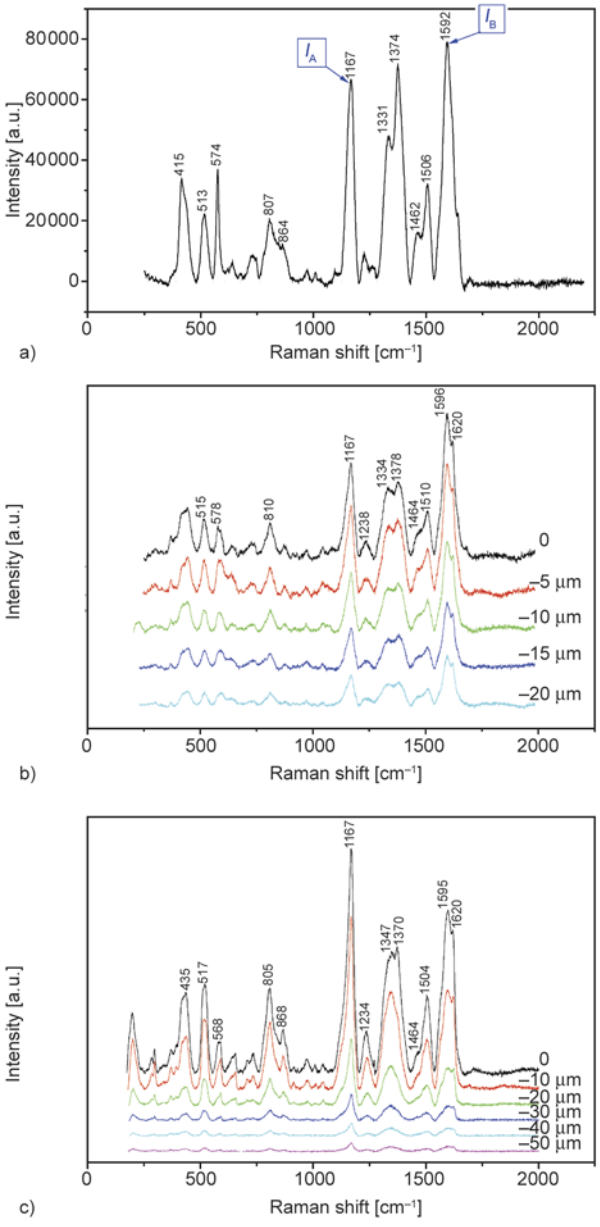

Figure 4. Raman spectrum of PANI bulk (a), PANI polymerized in AAO templates of 300 nm (b) and idem in 45 nm (c)

The confocal Raman spectra of PANI polymerized in AAO nanocavities of 300 and 45 nm, were recorded every 5 and 10 µm and plotted in Figure 4b and 4c, respectively.

The multiple scans every 5 and 10 µm in depth for PANI obtained into AAO of 300 and 45 nm, respectively, prove that the polymerization has been successful down to 20 µm (the length of AAO template) or 50 µm (the limit of confocal detection), respectively. The main difference between the spectra of these samples lies in the relative intensity of the main bands corresponding to $(C{-}H)_Q$ (1167 cm^{-1}) and $(C{=}C)_Q$ (1592 cm^{-1}). For PANI polymerized in AAO templates of 300 nm, the relationship between them is <1 and close to PANI bulk, but, on the contrary, for PANI polymerized in AAO of 45 nm the intensity of band $(C{-}H)_Q$ is much higher than the intensity of $(C{=}C)_Q$. This difference can be explained in terms of the orientation of the polymer chains and confinement effects. Confinement effects would bring about a change in the intensity of the orientation of the chains. Indeed, orientation affects the intensity of the Raman scattered-light for a given polarization of the incident light [35]. Owing to the smaller pore diameter, uniaxial symmetry is more pronounced for polyaniline obtained in AAO of 45 nm than of 300 nm, so the polymer chains tend to have a preferred orientation (parallel to the AAO walls) [36] thus increasing the intensity of the band at 1167 cm^{-1}, as observed.

To summarize, the spectra of PANI obtained in pores of 300 nm diameter present the same tendency than that of PANI bulk while spectra of PANI obtained in pores of 45 nm illustrate a confinement effect which is not seen in 300 nm. Moreover, from the quantitative analysis of spectra it can be inferred that ANI polymerization takes place quantitatively along the length of nanocavities, in agreement with SEM results.

3.5. PVDF-MWCNTs system

The preparation of PVDF-MWCNTs composites and the chemical characterization by Raman spectroscopy is described in experimental part. The morphological characterization by SEM spectroscopy of PVDF-

MWCNT (3%) nanofibers, once extracted from the templates, is shown in Figure 5. Figure 5a corresponds to PVDF-MWCNT nanostructures obtained in AAO templates of 45 nm and Figure 5b and 5c to nanostructures from templates of 300 nm. As in PANI case, Figure 5b and 5c shows a compact array of numerous PVDF-MWCNTs nanopillars with a perfectly defined geometry and big diameter. Once more, for nanocavities of 300 nm diameter and 20 μm length, the determining factor for achieving such free-standing nanostructure is due to the low aspect ratio of nanorod (about 60) and also the rigidity of the polymer. On the contrary and similar to PANI case, for AAO nanocavities of high aspect ratio (45 nm diameter and 100 μm length), Figure 5a shows an agglomeration of non-ordered PVDF-MWCNTs nanofibers. Here again, although the composite polymer is rigid, the high aspect ratio of nanofiber (around 2300) makes the nanofiber cannot stand up and collapse. In this case, is not observed a tendency of nanopillars to agglomerate like in the case of PANI. Moreover, on Figure 5d we can easily observe nanofibers of PVDF with fragmented carbon nanotubes. It is worth mentioning that some of fibers are without MWCNTs due to the small diameter of nanofiber (45 nm) and quite variety in diameter of carbon nanotubes (20–60 nm).

Therefore, PVDF-MWCNTs and PANI nanostructures with modulated morphologies, i.e. long nanofibers, short nanopillars, etc., can be easily achieved from anodized aluminum oxide (AAO) templates assisted methods. Moreover, the fact that PVDF-MWCNTs and PANI can be adjusted to nanoscopic dimensions, allow the study of size-conducting properties dependency in the nanoscale.

3.6. Broadband dielectric spectroscopy

BDS was the tool used to analyze the conductivity of the PANI and PVDF-MWCNTs samples in bulk and confined in AAO templates. The parameter of interest for this study is the DC conductivity $\sigma'(\omega)$ which can be extrapolated from AC conductivity at

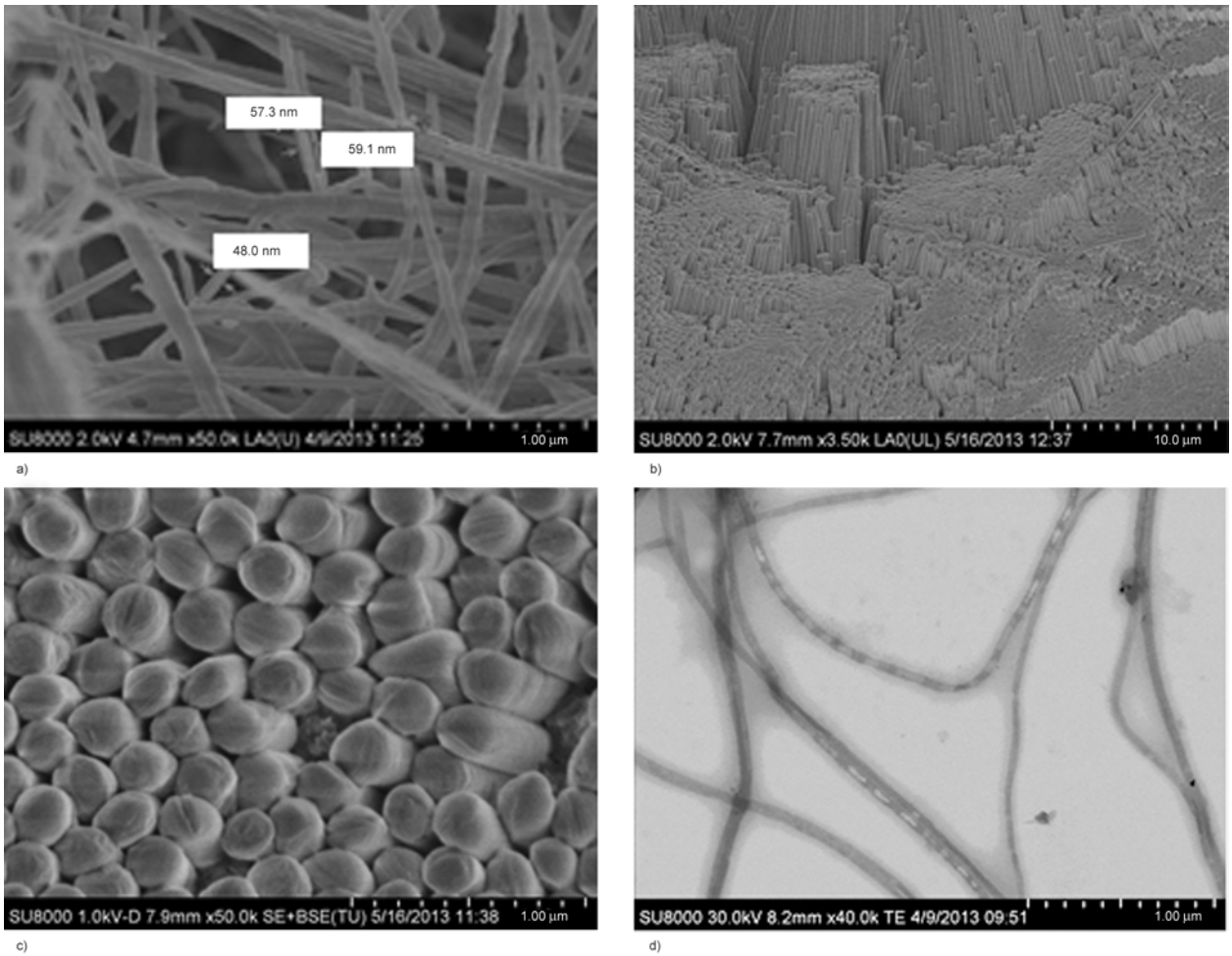

Figure 5. PVDF-MWCNTs 3% inside 45 nm (a) and 300 nm (b and c) AAO pores. TEM micrographs of PVDF-MWCNTs nanofibers with diameter of 45 nm (d).

low frequencies ($\sigma_{DC} \approx \sigma'(\omega \to 0)$). Consequently, only a small part of the dielectric data is of practical use.

3.6.1. PANI system

Figure 6a plots the conductivity of bulk PANI as a function of the frequency at a few key temperatures. The results clearly prove that doping has been effective because, at room temperature, conductivities achieved values of the order of 10^{-2} S·cm^{-1}. It also indicates that strongly doped samples behave like a metal and the real component of conductivity is frequency-independent in the whole range. Moreover, no contributions from interfacial polarization can be seen. The thermal behavior of conductivity is shown on Figure 6b and corresponds to the typical of a semiconductor. As observed in the figure, conductivity increases exponentially with temperature as hopping of carriers and diffusion of ions is favored. The arrows indicate that at first, the temperature was progressively increased during the measurement to a maximum of 120 °C and then decreased. Differences between two equivalent points can be explained by influence of atmosphere. Water is easily absorbed from the atmosphere and always presents in PANI samples so, in consequence, influences on ion transport and enhances conductivity. From this fact, it is reasonable to conclude that the conduction mechanism in doped PANI system is both electronic and ionic in nature. This procedure of temperature increase was applied for all the following measurements, therefore, it can assured that the conduction values are not influenced by the amount of absorbed water. To support this analysis, similar results were found in the literature in the study of the influence of water molecules over EB [37]. In that work, a positive temperature coefficient, $\partial\sigma/\partial T > 0$, also for high doping levels, was evidenced.

The variation of temperature in the PANI electrical transport data, in the range (223–393 K), is analyzed with the Mott VRH equation (Equation (1)) [38]:

$$\sigma(T) = \sigma_0 \exp\left[-\left(\frac{T_0}{T}\right)^{\gamma} \right] \quad (1)$$

where σ_0, a prefactor, T_0, a characteristic temperature including details of the system (density of states at Fermi level, number of nearest neighbor hopping site) and $\gamma = 1/(d+1)$, where d is the effective dimensionality of the system. Hence $d = 3$ for a 3D system, $d = 2$ in 2D and $d = 1$ in 1D. When confronted to a one-dimensional nanostructure, the dimensionality is affected by its diameter. Below a certain diameter, 1D-conduction occurs owing to the large proportion of ordered material. In our case (bulk PANI), the Mott VRH equation (Equation (1)) was best fitted with $\gamma = 0.25$ for a 3D system as can be seen in Figure 6c. This result clearly demonstrates a thermally-activated process. Moreover, Zhang *et al.* [39] reported that for slightly doped

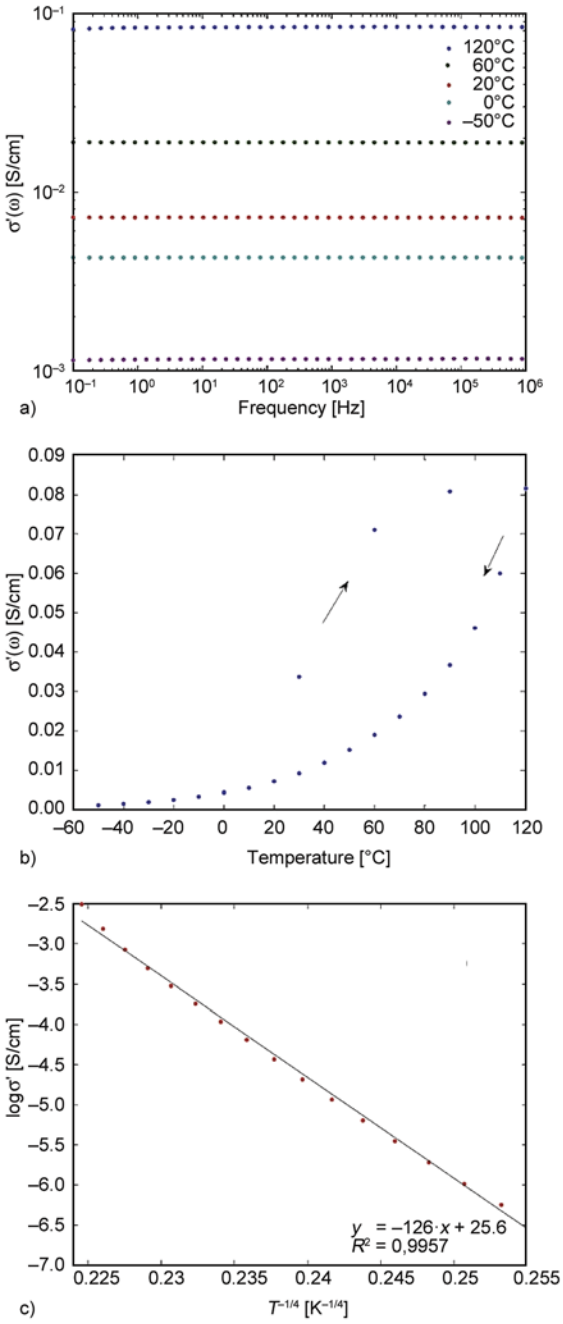

Figure 6. Conductivity of PANI bulk film versus frequency for different temperatures (a) and versus temperature at 0.1 Hertz (b). $\log\sigma$ vs $T^{-0.25}$ with linear fitting for the PANI bulk film at 0.1 Hertz (c).

PANI salt films with different dopants (HCl, CSA and DBSA), the increase of conductivity follows the increase of doping level, reaching a threshold for $\sigma > 10^{-2}$ at 10^{-1} M acid concentration (transition insulator-metal). These results also show conductivity independence of the frequency as in our study. Nevertheless, these authors [39] presented a negative real permittivity ϱ' over the whole range while we only observed it at low frequencies.

PANI nanofibers inside the AAO templates were also studied by BDS. Figures 7a and 7b plot the conductivity of PANI polymerized in AAO nanocavities of 45 nm as a function of frequency and temperature, respectively and (Figures 7c and 7d), the same plots for PANI polymerized in nanocavities of 300 nm. In both Figures, the red continuous line corresponds to an empty AAO template, being a reference line to evaluate the conduction response. This line clearly increases with frequency as can be expected from alumina, an insulator. The blue points are the experimental data and are situated above the reference line. From the comparison of both lines, an increment of conductivity is observed although probably lower to the real one, since the barrier layer present at the bottom of the AAO pores could act as a thin insulating that would impede electrons to fully go through. Both type of PANI filled templates exhibits higher conductivity by 2 orders of magnitude in comparison with empty template. Moreover, there is very little difference between the conductivity value for PANI in AAO pores of 45 and for PANI in 300 nm, being $8{\cdot}10^{-12}$ and $6{\cdot}10^{-12}$ S·cm^{-1}, respectively. In agreement with Martin and coworkers [18, 19], who observed 3 times higher conductivity for nanostructured PANI, one would expect that PANI nanofibers in AAO templates of 45 nm were more conductive than PANI nanofibers in AAO templates of 300 nm. Nevertheless, in agreement to our results, Wu *et al.* [22] found that for PANI nanowires and nanorods the electrical conductivity values were

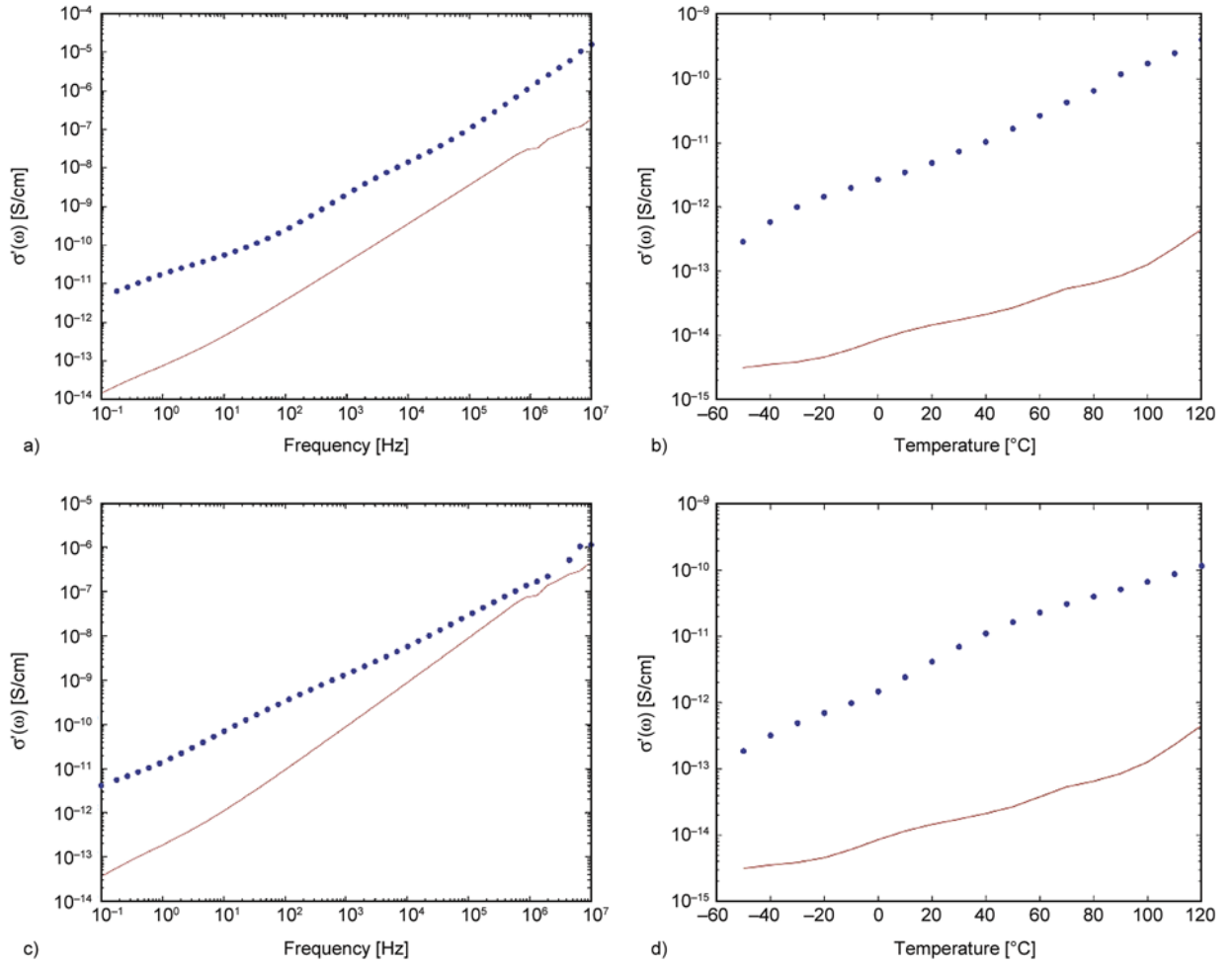

Figure 7. Conductivity of AAO template filled with PANI as a function of frequency, at room temperature for template of 45 nm (a) and for 300 nm (c) and as a function of temperature at 0.1 Hertz for template of 45 nm (b) and 300 nm (d). Empty AAO template is used as a reference (red line).

similar, 1.25 and 2.06 S·cm^{-1}, respectively, so the difference found in both types of structures is similar to that found by us. In our case, the rather higher conductivity value obtained for PANI in nanopores of 45 nm could be due to the thinner barrier layer of AAO template of 45 nm compared to that of 300 nm.

3.6.2. PVDF-MWCNTs system

Figure 8 displays the conductivity variation of bulk PVDF-MWCNT films with different weight percentages of MWCNT, 0; 1; 3 and 5 %. It is obvious that a small addition of CNTs increases the conduction by more than 10 orders of magnitude compared to pure PVDF. At room temperature, bulk PVDF has a conductivity of 10^{-14} S·cm^{-1} while for PVDF-MWCNT (1%) is $3\cdot10^{-3}$ S·cm^{-1}, similar to that obtained for polyaniline. For higher MWCNT content, higher conductivity, but the increase is quite small compared to the change in concentration. Tripling the quantity of MWCNT (from 1 to 3 wt%), the conductivity increases only 2 orders of magnitude, thus indicating that a percolation threshold has already been reached at 1 wt%. Nevertheless, studies do not agree on the percolation threshold [40–44] since there is no unique value, as it depends on the process conditions, the possible preferred orientation of the CNTs in the matrix, the CNTs type and their characteristics (i.e. AR, surface modification [45–48]). In the case of a 5 wt% of MWCNT, the conductivity still increases although flexibility and processability of the polymer is lost as reported by Lonjon *et al*. [49] in the case of P(VDF-TrFE) and nickel nanowires. For these two opposing reasons, only PVDF-MWCNT (3%) in bulk and infiltrated in AAO templates will be deeply studied by BDS.

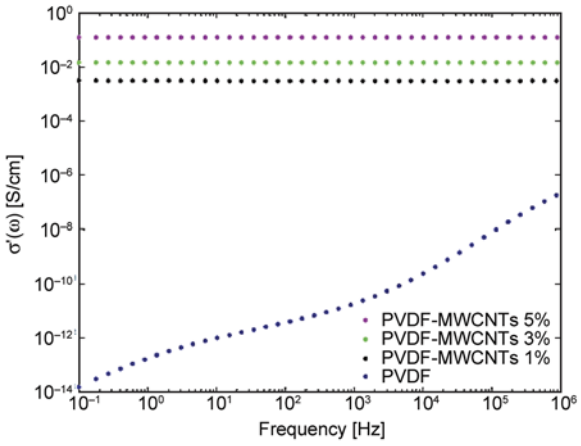

Figure 8. AC conductivity of PVDF-MWCNTs films at different weight percentages of MWCNT at room temperature

Figure 9 presents the isochrones of PVDF-MWCNT (3%) films at the lowest measured frequency (0.1 Hz). The conductivity evolution of the nanocomposite in function of temperature is composed of two different regimes. Below 100 °C the evolution is characteristic of a semiconductor with the conductivity increasing with temperature ($\partial\sigma/\partial T > 0$). Over 100 °C, there is a switch and conductivity behaves like a metal, decreasing with increasing temperature ($\partial\sigma/\partial T < 0$). In our case ($T < T_m$), we are faced with a static and immobilized conductive network of MWCNTs in the polymer matrix since we are in the percolation region and at low temperatures. To explain the results we presume that, at first, the tunneling of the electrons between adjacent carbon nanotubes is favored by the increase of temperature. The electrons gain thermal energy which helps them to overcome the potential barrier more easily, as supported by the FIT model. However, at a temperature limit of 100 °C, for this PVDF-MWCNT (3%) composite the thermal expansion of the polymer matrix compensates the thermally-induced tunneling of MWCNT. This can be explained by the fact that increasing the average distance between nanotubes, the amount of insulating polymer becomes significant and makes a wider barrier that electrons struggle overpass, hence a reduction in the conductivity with further increase of temperature would be observed. Moreover, in semicrystalline polymers, the volume expansion of the polymer matrix which separates the fillers is also attributed to the transformation of the crystalline phase to the amorphous phase. These results agree with others reported in the literature [50]. For instance Tao *et al*. [51] also reported a decrease in conductivity with temperature for a composite of MWCNTs and polyethylene at higher temperatures ($T > T_m$) and was related to the phenomena of crystallization of polyethylene which would disconnect the conductive paths [51]. Other authors [40, 52] also observed a continuous increase of conductivity with temperature below T_m (positive temperature coefficient effect of the resistivity). Moreover, an effect similar was reported by Li *et al*. [50] below a transition temperature of 80 °C. This effect was explained by the fact that at higher temperatures ($T > T_m$), Brownian motion of the carbon nanotubes make them mobile within the melting matrix and they tend to coagulate which results in an decrease of the electrical conductivity of the composite with temperature.

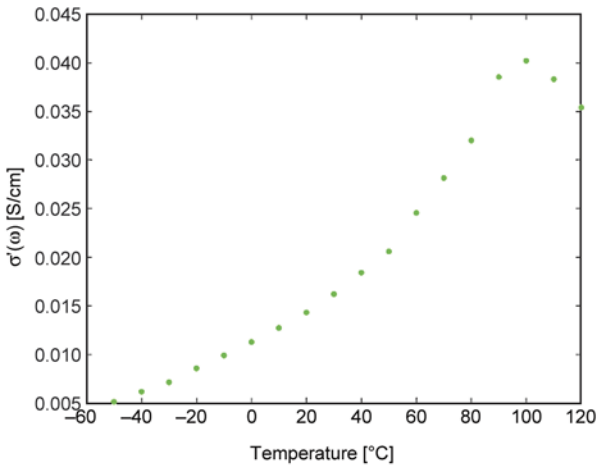

Figure 9. Conductivity versus temperature of PVDF-MWCNTs films at 0.1 Hz for a 3% CNT content

Figure 10 presents the conductivity of two AAO templates filled with the nanocomposite of PVDF-MWCNT 3%, at room temperature. Figure 10a accounts for the template of 45 nm of diameter; the template filled with PVDF and with PVDF-MWCNT 3%. It is observed that infiltrated conducting nanocomposite in AAO exhibits higher conductivity than the PVDF infiltrated alone and evidences the rather surprising fact that carbon nanotubes with an average diameter of 40 nm could penetrate the small pores. Figure 10b accounts for the templates of 300 nm of diameter and as observed do not show a significant improvement of conductivity. The above mentioned effect of the insulating barrier layer could explain the low response.

Comparing the conductivity values of polymer nanostructures of PVDF-MWCNT 3% and of PANI, in AAO templates of 45 and 300 nm diameters, the difference is the same as that found between the two bulk polymers. So, the same conductivity is obtained for a nanostructured ECP (PVDF with a 3% of MWCNT) than for a nanostructured ICP (PANI). Therefore, the above results evidence that BDS is an easy and non-destructive method to determine electrical conductivity of PANI and PVDF-MWCNT polymer nanostructures confined in AAO templates. Moreover, this example could be extended to other nanoscopic conducting polymer systems

4. Conclusions

The core of this work was the synthesis of one-dimensional polymer nanostructures of PANI and PVDF-MWCNT within AAO templates to combine performance and conductivity down to nanoscale and we present an accurate way of increasing and modeling the conductivity of two different kinds' polymeric materials by nanostructuration that opens huge possibilities in the technologies of the future. Conductivity of bulk materials was increased substantially by several orders of magnitude compared to a classic insulating polymer either by doping the intrinsic conducting polymer, polyaniline, or by incorporating conductive nanofillers into poly (vinylidene fluoride). It was demonstrated that by using AAO template it was possible to prepare different kinds of high quality conductive nanomaterials with variable diameters of nanoarray (45–300 nm). The nanostructures were obtained successfully inside the templates either by a simple chemical method of polymerization of aniline or by melt infiltration of the PVDF-MWCNT nanocomposite. Polymerization and infiltration parameters were found to be critical and needed to be well-controlled to achieve the desired morphology. Raman spectroscopy used in

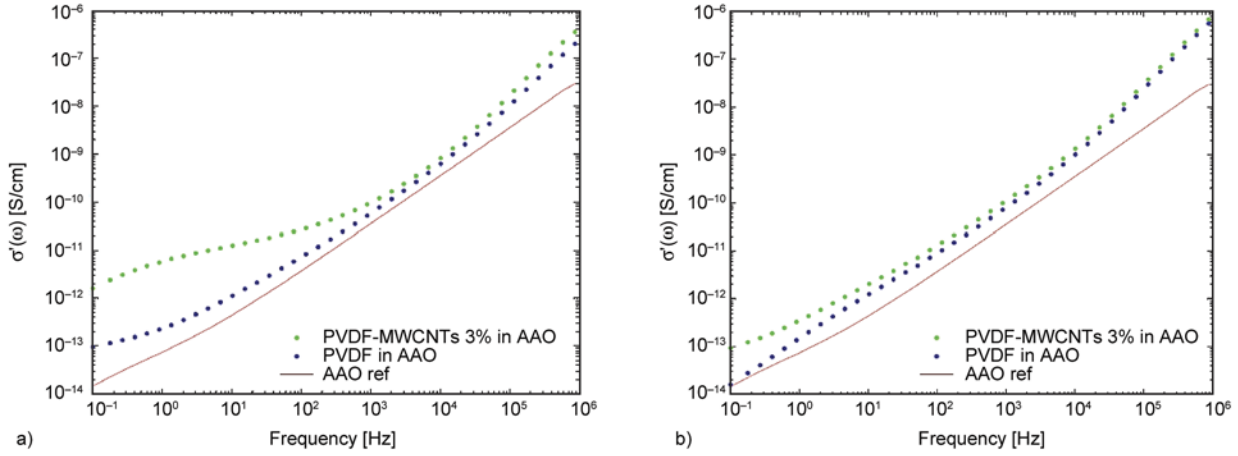

Figure 10. Conductivity of filled AAO template with PVDF-MWCNTs 3% at room temperature for 45 nm pore diameter (a) and for 300 nm (b)

confocal mode detected that the emeraldine salt of PANI was obtained correctly along the length of the nanopores of the AAO template.

For the first time, to our knowledge, dielectric spectroscopy was used to determine in a non-destructive way the conductivity of nanostructures present within the AAO templates. Thus, control over the concentration of dopant for PANI as well as of the filler concentration for PVDF-MWCNT makes possible the tuning of the level of conduction.

In summary, infiltration of a conducting polymer in a lab-made anodized aluminum oxide template is an effective method to produce well-defined one-dimensional nanostructures with regular spatial arrangement and remarkably low polydispersity. Besides, the possibility of precise control of aspect ratio allows adjusting to the application needs. Once free of the template, this kind of compact conducting nanoarray is of great interest for sensing or field emission display as they could be addressed individually. This new approach for rapid evaluation of conductivity of nanomaterials, however, does not give objective value due to the insulating properties of templates.

Acknowledgements

Financial support from the Spanish 'Ministerio de Economia y Competitividad' under projects MAT2011-24797 and MAT2014-53437-C2-1 is acknowledged. The authors thank D. Gómez for SEM experiments and I. Muñoz for Raman spectra. Authors thank Miguel Ángel López Manchado por providing MWCNTs.

References

[1] Long Y-Z., Chen Z., Gu C., Wan M., Duvail J-L., Liu Z., Ringer S. P.: A review on electronic transport properties of individual conducting polymer nanotubes and nanowires. in 'Nanowires science and technology' (ed.: Lupu N.) InTech, Rijeka, 223–242 (2010).
DOI: 10.5772/39488

[2] Wang Y. Y., Jing X. L.: Intrinsically conducting polymers for electromagnetic interference shielding. Polymers for Advanced Technologies, **16**, 344–351 (2005).
DOI: 10.1002/pat.589

[3] Koval'chuk A. A., Shchegolikhin A. N., Shevchenko V. G., Nedorezova P. M., Klyamkina A. N., Aladyshev A. M.: Synthesis and properties of polypropylene/multiwall carbon nanotube composites. Macromolecules, **41**, 3149–3156 (2008).
DOI: 10.1021/ma800297e

[4] Saini P., Choudhary V.: Electrostatic charge dissipation and electromaghetic interference shielding response of polyaniline based conducting fabrics. Indian Journal of Pure and Applied Physics, **51**, 112–117 (2013).

[5] Vecino M., González I., Muñoz M. E., Santamaría A., Ochoteco E., Pomposo J. A.: Synthesis of polyaniline and application in the design of formulations of conductive paints. Polymers for Advanced Technologies, **15**, 560–563 (2004).
DOI: 10.1002/pat.502

[6] Griesser T., Radl S. V., Koepplmayr T., Wolfberger A., Edler M., Pavitschitz A., Kratzer M., Teichert C., Rath T., Trimmel G., Schwabegger G., Simbrunner C., Sitter H., Kern W.: UV-induced modulation of the conductivity of polyaniline: Towards a photo-patternable charge injection layer for structured organic light emitting diodes. Journal of Materials Chemistry, **22**, 2922–2928 (2012).
DOI: 10.1039/c1jm14100g

[7] Peng H., Zhang L., Soeller C., Travas-Sejdic J.: Conducting polymers for electrochemical DNA sensing. Biomaterials, **30**, 2132–2148 (2009).
DOI: 10.1016/j.biomaterials.2008.12.065

[8] Pramanik S., Das G., Karak N.: Facile preparation of polyaniline nanofibers modified bentonite nanohybrid for gas sensor application. RSC Advances, **3**, 4574–4581 (2013).
DOI: 10.1039/c3ra22557g

[9] Li G., Li Y., Li Y., Peng H., Chen K.: Polyaniline nanorings and flat hollow capsules synthesized by *in situ* sacrificial oxidative templates. Macromolecules, **44**, 9319–9323 (2011).
DOI: 10.1021/ma2014854

[10] Wang W., Schiff E. A.: Polyaniline on crystalline silicon heterojunction solar cells. Applied Physics Letters, **91**, 133504/1–133504/3 (2007).
DOI: 10.1063/1.2789785

[11] Zhang J., Hreid T., Li X., Guo W., Wang L., Shi X., Su H., Yuan Z.: Nanostructured polyaniline counter electrode for dye-sensitised solar cells: Fabrication and investigation of its electrochemical formation mechanism. Electrochimica Acta, **55**, 3664–3668 (2010).
DOI: 10.1016/j.electacta.2010.01.115

[12] Duek E. A. R., De Paoli M. A., Mastragostino M.: An electrochromic device based on polyaniline and prussian blue. Advanced Materials, **4**, 287–291 (1992).
DOI: 10.1002/adma.19920040410

[13] Yang Y., Hao Y., Yuan J., Niu L., Xia F.: *In situ* preparation of caterpillar-like polyaniline/carbon nanotube hybrids with core shell structure for high performance supercapacitors. Carbon, **78**, 279–287 (2014).
DOI: 10.1016/j.carbon.2014.07.004

[14] Chen J-T., Hsu C-S.: Conjugated polymer nanostructures for organic solar cell applications. Polymer Chemistry, **2**, 2707–2722 (2011).
DOI: 10.1039/c1py00275a

[15] Sathiyanarayanan S., Muthkrishnan S., Venkatachari G.: Corrosion protection of steel by polyaniline blended coating. Electrochimica Acta, **51**, 6313–6319 (2006).
DOI: 10.1016/j.electacta.2006.04.015

[16] Apodaca D. C., Pernites R. B., Ponnapati R., Del Mundo F. R., Advincula R. C.: Electropolymerized molecularly imprinted polymer film: EIS sensing of bisphenol A. Macromolecules, **44**, 6669–6682 (2011). DOI: 10.1021/ma2010525

[17] Chen M-C., Sun Y-C., Chen Y-H.: Electrically conductive nanofibers with highly oriented structures and their potential application in skeletal muscle tissue engineering. Acta Biomaterialia, **9**, 5562–5572 (2013). DOI: 10.1016/j.actbio.2012.10.024

[18] Martin C. R., Parthasarathy R., Menon V.: Template synthesis of electronically conductive polymers – A new route for achieving higher electronic conductivities. Synthetic Metals, **55**, 1165–1170 (1993). DOI: 10.1016/0379-6779(93)90218-l

[19] Parthasarathy R. V., Martin C. R.: Template-synthesized polyaniline microtubules. Chemistry of Materials, **6**, 1627–1632 (1994). DOI: 10.1021/cm00046a011

[20] Marquez M., Patel K., Carswell A. D. W., Schmidtke D. W., Grady B. P.: Synthesis of nanometer-scale polymeric structures on surfaces from template assisted admicellar polymerization: A comparative study with protein adsorption. Langmuir, **22**, 8010–8016 (2006). DOI: 10.1021/la061108g

[21] Marquez M., Kim S., Jung J., Truong N., Teeters D., Grady B. P.: Factors affecting the synthesis of polymeric nanostructures from template assisted admicellar polymerization. Langmuir, **23**, 10008–10019 (2007). DOI: 10.1021/la7011809

[22] Wu J., Sun Y., Xu W., Zhang Q.: Investigating thermoelectric properties of doped polyaniline nanowires. Synthetic Metals, **189**, 177–182 (2014). DOI: 10.1016/j.synthmet.2014.01.007

[23] Khdary N. H., Abdesalam M. E., El Enany G.: Mesoporous polyaniline films for high performance supercapacitors. Journal of the Electrochemical Society, **161**, G63–G68 (2014). DOI: 10.1149/2.0441409jes

[24] Maiz J., Zhao W., Gu Y., Lawrence J., Arbe A., Alegría A., Emrick T., Colmenero J., Russell T. P., Mijangos C.: Dynamic study of polystyrene-*block*-poly(4-vinylpyridine) copolymer in bulk and confined in cylindrical nanopores. Polymer, **55**, 4057–4066 (2014). DOI: 10.1016/j.polymer.2014.05.042

[25] Serghei A., Chen D., Lee D. H., Russell T. P.: Segmental dynamics of polymers during capillary flow into nanopores. Soft Matter, **6**, 1111–1113 (2010). DOI: 10.1039/b921757f

[26] Blaszczyk-Lezak I., Hernández M., Mijangos C.: One dimensional PMMA nanofibers from AAO templates. Evidence of confinement effects by dielectric and Raman analysis. Macromolecules, **46**, 4995–5002 (2013). DOI: 10.1021/ma400173q

[27] Martin J., Mijangos C., Sanz A., Ezquerra T. A., Nogales A.: Segmental dynamics of semicrystalline poly(vinylidene fluoride) nanorods. Macromolecules, **42**, 5395–5401 (2009). DOI: 10.1021/ma900754v

[28] Suzuki Y., Duran H., Steinhart M., Butt H. J., Floudas G.: Homogeneous crystallization and local dynamics of poly(ethylene oxide) (PEO) confined to nanoporous alumina. Soft Matter, **9**, 2621–2628 (2013). DOI: 10.1039/c2sm27618f

[29] Kremer F., Różański S. A.: The dielectric properties of semiconducting disordered materials. in 'Broadband dielectric spectroscopy' (eds.: Kremer F., Schönhals A.) Springer, Berlin, 475–494 (2003). DOI: 10.1007/978-3-642-56120-7_12

[30] Maiz J., Sacristan J., Mijangos C.: Probing the presence and distribution of single-wall carbon nanotubes in polyvinylidene difluoride 1D nanocomposites by confocal Raman spectroscopy. Chemical Physics Letters, **484**, 290–294 (2010). DOI: 10.1016/j.cplett.2009.11.063

[31] Zhang J., Liu C., Shi G.: Raman spectroscopic study on the structural changes of polyaniline during heating and cooling processes. Journal of Applied Polymer Science, **96**, 732–739 (2005). DOI: 10.1002/app.21520

[32] Salvatierra R. V., Moura L. G., Oliveira M. M., Pimenta M. A., Zarbin A. J. G.: Resonant Raman spectroscopy and spectroelectrochemistry characterization of carbon nanotubes/polyaniline thin film obtained through interfacial polymerization. Journal of Raman Spectroscopy, **43**, 1094–1100 (2012). DOI: 10.1002/jrs.3144

[33] Stejskal J., Exnerová M., Moravková Z., Trchová M., Hromadková J., Prokeš J.: Oxidative stability of polyaniline. Polymer Degradation and Stability, **97**, 1026–1033 (2012). DOI: 10.1016/j.polymdegradstab.2012.03.006

[34] Islam R., Chan-Yu-King R., Brun J-F., Gors C., Addad A., Depriester M., Hadj-Sahraoui A., Roussel F.: Transport and thermoelectric properties of polyaniline/reduced graphene oxide nanocomposites. Nanotechnology, **25**, 475705/1–475705/9 (2014). DOI: 10.1088/0957-4484/25/47/475705

[35] Bower D. I.: Infrared dichroism, polarized fluorescence and Raman spectroscopy. in 'Structure and properties of oriented polymers' (ed.: Ward I. M.) Springer, Dordrecht, 181–233 (1997). DOI: 10.1007/978-94-011-5844-2_4

[36] Liem H-M., Etchegoin P., Whitehead K-S., Bradley D. D. C.: Raman anisotropy measurements: An effective probe of molecular orientation in conjugated polymer thin films. Advanced Functional Materials, **13**, 66–72 (2003). DOI: 10.1002/adfm.200390008

[37] Calleja R. D., Matveeva E. S., Parkhutik V. P.: Electric relaxation in chemically synthesized polyaniline: Study using electric modulus formalism. Journal of Non-Crystalline Solids, **180**, 260–265 (1995). DOI: 10.1016/0022-3093(94)00470-6

[38] Moliton A., Hiorns R. C.: Review of electronic and optical properties of semiconducting π-conjugated polymers: Applications in optoelectronics. Polymer International, **53**, 1397–1412 (2004). DOI: 10.1002/pi.1587

[39] Zhang X., Zhu J., Haldolaarachchige N., Ryu J., Young D. P., Wei S. Y., Guo Z.: Synthetic process engineered polyaniline nanostructures with tunable morphology and physical properties. Polymer, **53**, 2109–2120 (2012). DOI: 10.1016/j.polymer.2012.02.042

[40] Prashantha K., Lee J. H.: Positive temperature coefficient characteristics of multi-walled carbon nanotube filled polyvinylidene fluoride nanocomposites. Journal of Macromolecular Science Part A: Pure and Applied Chemistry, **48**, 737–741 (2011). DOI: 10.1080/10601325.2011.596056

[41] Zhang C., Zhu J., Ouyang M., Ma C., Sumita M.: Conductive network formation and electrical properties of poly(vinylidene fluoride)/multiwalled carbon nanotube composites: Percolation and dynamic percolation. Journal of Applied Polymer Science, **114**, 1405–1411 (2009). DOI: 10.1002/app.30729

[42] Almasri A., Ounaies Z., Kim Y. S., Grunlan J.: Characterization of solution-processed double-walled carbon nanotube/poly(vinylidene fluoride) nanocomposites. Macromolecular Materials and Engineering, **293**, 123–131 (2008). DOI: 10.1002/mame.200700229

[43] Li Q., Xue Q., Zheng Q., Hao L., Gao X.: Large dielectric constant of the chemically purified carbon nanotube/polymer composites. Materials Letters, **62**, 4229–4231 (2008). DOI: 10.1016/j.matlet.2008.06.047

[44] Zhao Z., Zheng W., Yu W., Long B.: Electrical conductivity of poly(vinylidene fluoride)/carbon nanotube composites with a spherical substructure. Carbon, **47**, 2118–2120 (2009). DOI: 10.1016/j.carbon.2009.03.043

[45] Vukićević R., Vukovic I., Stoyanov H., Korwitz A., Pospiech D., Kofod G., Loos K., ten Brinke G., Beuermann S.: Poly(vinylidene fluoride)-functionalized single-walled carbon nanotubes for the preparation of composites with improved conductivity. Polymer Chemistry, **3**, 2261–2265 (2012). DOI: 10.1039/c2py20166f

[46] Ansón-Casaos A., González-Domínguez J. M., Diez-Pascual A. M., Gómez-Fatou M. A., Martínez M. T.: Choosing the chemical route for carbon nanotube integration in poly(vinylidene fluoride). Journal of Physical Chemistry C, **116**, 16217–16225 (2012). DOI: 10.1021/jp302212m

[47] Yu S., Zheng W., Yu W., Zhang Y., Jiang Q., Zhao Z.: Formation mechanism of β-phase in PVDF/CNT composite prepared by the sonication method. Macromolecules, **42**, 8870–8874 (2009). DOI: 10.1021/ma901765j

[48] Sharma M., Madras G., Bose S.: Cooperativity and structural relaxations in PVDF/PMMA blends in the presence of MWNTs: An assessment through SAXS and dielectric spectroscopy. Macromolecules, **47**, 1392–1402 (2014). DOI: 10.1021/ma4023718

[49] Lonjon A., Demont P., Dantras E., Lacabanne C.: Mechanical improvement of P(VDF-TrFE)/nickel nanowires conductive nanocomposites: Influence of particles aspect ratio. Journal of Non-Crystalline Solids, **358**, 236–240 (2012). DOI: 10.1016/j.jnoncrysol.2011.09.019

[50] Li Q., Xue Q. Z., Gao X. L., Zheng Q. B.: Temperature dependence of the electrical properties of the carbon nanotube/polymer composites. Express Polymer Letters, **3**, 769–777 (2009). DOI: 10.3144/expresspolymlett.2009.95

[51] Tao F., Bonnaud L., Auhl D., Struth B., Dubois P., Bailly C.: Influence of shear-induced crystallization on the electrical conductivity of high density polyethylene carbon nanotube nanocomposites. Polymer, **53**, 5909–5916 (2012). DOI: 10.1016/j.polymer.2012.10.026

[52] Jiang S. L., Yu Y., Xie J. J., Wang L. P., Zeng Y. K., Fu M., Li T.: Positive temperature coefficient properties of multiwall carbon nanotubes/poly(vinylidene fluoride) nanocomposites. Journal of Applied Polymer Science, **116**, 838–842 (2010). DOI: 10.1002/app.31569